# Chemical-Scale Studies of the Nicotinic and Muscarinic Acetylcholine Receptors

Thesis by

**Michael McCann Torrice**

In Partial Fulfillment of the

Requirements for the Degree of

Doctor of Philosophy


**California Institute of Technology**
**Pasadena, CA**
**2009**
**(Defended July 25, 2008)**

*In memory of my grandparents:*

*Margaret and Ronald McCann*

*Virginia and Carl Torrice*

# Acknowledgments

*The struggle itself towards the heights is enough to fill a man's heart. One must imagine Sisyphus happy.*

- Albert Camus

My six years of pushing the stubborn rock of graduate school uphill have come to an end. Thankfully, I've had many sets of hands helping me shove.

The first set belongs to my advisor, Dennis Dougherty. In my senior year of college, while I was pondering graduate school, Dennis gave two lectures at M.I.T. I attended both and was hooked by his discussions of unnatural amino acids, cation-π interactions, and the brain. His ability to tell engaging scientific stories and to explain his reasoning in a transparent manner continues to inspire me. As an advisor, Dennis has allowed me a great deal of freedom, while also injecting timely doses of guidance. He has stood by me when projects appeared mired in confusion. And he has provided me the space to explore a non-traditional career path. For his support, academic and otherwise, I thank him.

All of the research contained in the following pages would have been difficult to perform without the expertise of Henry Lester and his lab. Henry has served as a fresh set of eyes for perplexing data and a source of new experiment ideas during countless "Unnaturals Club" meetings. I also greatly appreciate his support of my ventures into science writing. Bruce Cohen, a member of the Lester Group, has also been an excellent electrophysiology tutor.

I also thank the other members of my committee, Peter Dervan, Bill Goddard, and Dave Tirrell, for their words of encouragement and advice throughout my graduate career.

When I arrived at CalTech I met an amazing collection of scientists in the Dougherty Group who made me feel truly welcome. The Lake Avenue lunch squad of Josh Maurer, Gabriel Brandt, Don Elmore, Darren Beene, and James Petersson were a constant source of engaging discussions about topics serious and silly that often involved list-making. Niki Zacharias, Sarah May, David Dahan, Tingwei Mu, and Steve Spronk were also integral in helping me grasp the basics of graduate school and the ways of the Dougherty Group. Amanda Cashin was my collaborator for the D89 project (Chapter 2) and the project's initiator. Lori Lee has been an indispensable source of scientific and career advice during the past six years; she has also been a great friend.

The current cast of Doughertyites has continued the group's scientific tradition of going where no organic chemist has gone before. I have enjoyed working alongside my fellow classmates, Joanne (Xinan) Xiu, Erik Rodriguez, and Amy Eastwood. Joanne is a dedicated scientist who never seemed to be flustered by the grind of graduate school. Erik's experimental advice has been crucial throughout the years; in particular, I thank him for his assistance with the frameshift suppression work in the D89 project. I thank Amy for commiserating with me over research, graduate school, and whatnot, especially as this document was being prepared. As my Opus co-captain, Ariele Hanek made dealing with an unruly machine a much more manageable job. I appreciate my discussions about the GPCR project, and science in general, with Kiowa Bower; I hope he doesn't regret switching receptors. Jai Shanata, Katie McMenimen, and Kristin

Gleitsman have listened to my ideas, read my writing, and provided me with valuable feedback over the years. I thank all the newer group members—Angela Blum, Noah Duffy, Shawna Frazier, Sean Kedrowski, Kay (Walrati) Limapichat, Darren Nakamura, and Nyssa Puskar—for humoring the grumblings of an older graduate student.

Of course, my past six years haven't solely been spent inside the lab. I've been fortunate to meet many people "on the outside" who have enriched my time at CalTech. I wish to thank a specific few here. My move from research to science writing would not be possible without Doug Smith at *Engineering & Science*. I would like to thank him for the opportunity to write while at CalTech and also for the encouragement to take the plunge into a new career. Roger Donaldson and Ben Collins were two of my several roommates. I simply thank them for all the laughs that carried me through the ebbs and flows of graduate school. Besides proofreading this, at times dry, document, Graef Allen has also been a movie-going, cat-watching, and Thai-food-eating companion. I thank her for her constant support, patience, and understanding during the home stretch of this long marathon.

Finally, I thank my family for their limitless cross-country encouragement. My aunts have been cheering me on at school since kindergarten. My parents' support for my varied pursuits has been unending. Together they have all fostered my curiosity in science that has led me here.

# Abstract

This dissertation describes three chemical-scale studies of neuroreceptor structure and function. Incorporation of unnatural amino acids into two acetylcholine receptors—the nicotinic acetylcholine receptor (nAChR) and the $M_2$ muscarinic acetylcholine receptor ($M_2$AChR)—and an electrophysiology assay of receptor function were performed in each of the studies. The nAChR is a ligand-gated ion channel (LGIC) and the $M_2$AChR is a G-protein-coupled receptor (GPCR).

In Chapter 2, a highly conserved aspartate residue (D89) that is near the agonist binding site of the nAChR was probed for its role in agonist binding. We found that the side chain of D89 establishes a redundant network of hydrogen bonds and preorganizes the agonist binding site by positioning a critical agonist-binding residue, tryptophan 149 (W149). Previous studies of a D89N mutant led to the proposal that a negative charge at D89 was essential for receptor function. However, our studies show that neutral side chains at position 89 function well, only if an unfavorable electrostatic clash is avoided.

Chapter 3 describes our attempts to incorporate unnatural amino acids into the $M_2$AChR, a GPCR. GPCR activity is assayed through second messenger signaling pathways, unlike the direct readout assays of LGICs. These second messenger pathways require significant amounts of optimization to create assays that produce reliable and robust data. In our experiments, variability of dose-response relationship data between batches of cells was the most significant concern. Several factors were investigated to reduce this batch-to-batch variability. After a reliable means to assay $M_2$AChR function

was found, we performed a preliminary search for tryptophan residues in the agonist binding site that form a cation-π interaction with acetylcholine.

Finally, in Chapter 4, we discuss the use of hydroxy acids to scan the αM1 transmembrane helix of the nAChR for residues that undergo structural rearrangements during gating. Hydroxy acids disrupt hydrogen bonding in protein backbones and thus provide a means to detect backbone interactions that form or break during gating. The hydroxy acid analog of valine, valic acid (Vah), was incorporated at ten positions along the αM1 helix. Backbone mutations at five residues on the intracellular side of a conserved proline (P221) produced shifts in dose-response relationships.

# Table of Contents

# List of Figures

# List of Tables

# **Chapter 1:** An Introduction to Chemical-Scale Neuroscience

## 1.1 Chemistry and the Brain

No object in nature is more complex than the human brain. The average adult brain contains more than one-hundred billion (> $10^{11}$) neurons. Each neuron connects with one- to ten-thousand ($10^3$–$10^4$) other neurons through specialized junctions, called synapses. There are, therefore, an unfathomable quadrillion ($10^{15}$) synapses in the human brain—a quantity that eclipses the number of stars in our galaxy (~ 400 billion). This intricate web of cells draws massive amounts of energy: the brain uses 25% of the body's glucose and 20% of its oxygen[1]. This energy consumption fuels the processing of information that regulates mental and physical actions, such as locomotion, social behavior, learning, and memory. How can an organ as complex as the human brain be understood, in part, through the properties and interactions of its chemical components?

A chemical-scale understanding is possible because, at a basic level, the brain processes information through chemical signals transmitted between neurons. This exchange is called synaptic transmission (Figure 1.1). Synaptic transmission begins with an electrical signal, called an action potential, traveling down a neuron's axon. To communicate with another neuron, this signal must move towards an axon terminal that has formed a synapse with the dendrite of the other neuron (***i*** in Figure 1.1b) This first cell is referred to as the presynaptic cell and the second cell as the postsynaptic cell. At

the axon terminal, the electrical signal stimulates the mobilization of vesicles containing neurotransmitters. These vesicles fuse with the cell membrane and release their contents into the space between the two cells, the synaptic cleft (***ii*** in Figure 1.1b). These chemicals diffuse across the synaptic cleft and bind to neuroreceptors on the postsynaptic cell. Activated neuroreceptors either directly or indirectly produce electrical signals in the postsynaptic cell, which can then promote or inhibit the generation of an action potential in this cell (***iii*** in Figure 1.1b). Thus an electrical signal in the presynaptic cell is translated into a chemical signal that the postsynaptic cell decodes back into an electrical signal.

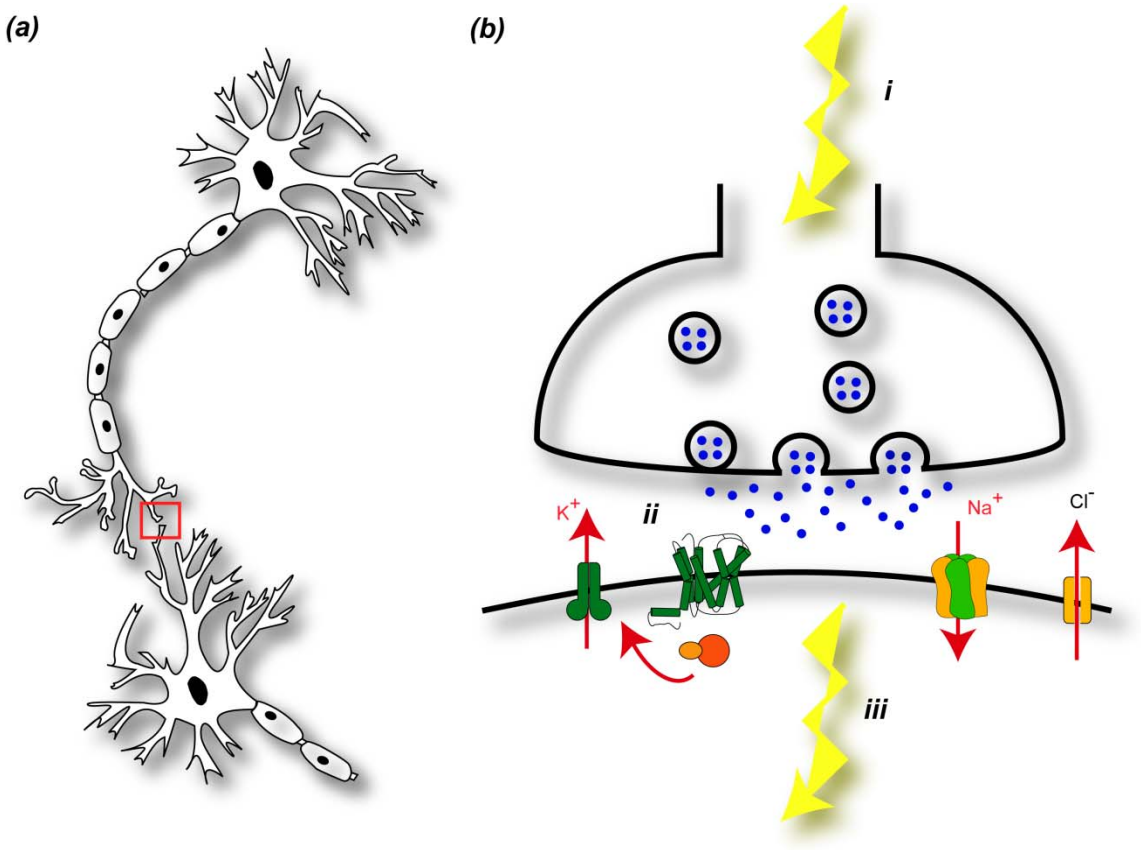


**Figure 1.1.** Synaptic transmission. ***(a)*** Two neurons making a connection: an axon terminal of the presynaptic cell (*top*) forms a synapse (red box) with a dendrite from the postsynaptic cell (*bottom*). ***(b)*** Scheme of synaptic transmission

Through the various neurotransmitters and neuroreceptors at synapses, neurons can send myriad chemical signals. Neurotransmitters can be small organic molecules, peptides, or even fatty acids. Two main types of neuroreceptor proteins exist. Ligand-gated ion channels (LGICs) bind neurotransmitters and directly produce electrical signals. These proteins undergo conformational changes upon ligand binding that produce open protein pores for ions to pass across the cell membrane. G-protein-coupled receptors (GPCRs), the second type of neuroreceptor, activate second messenger systems within the neuron upon neurotransmitter binding. These second messengers can gate ion channels on the neuron surface, but can also intiate other cellular pathways, such as gene transcription.

Chemical-scale studies of the brain analyze the actions of these neurotransmitter and neuroreceptor systems. The goal of chemical-scale neuroscience is to understand the chemistry of the brain through studies of the gating / activation mechanisms of neuroreceptors and the molecular recognition of neurotransmitters by neuroreceptors.

## 1.2 The Unnatural Amino Acid Methodology

### *1.2.1 The Power of Unnatural Amino Acids*

To probe neurotransmitters and neuroreceptors at the chemical scale, researchers need precise techniques that allow them to investigate these molecules in the brain as chemists would study molecules in a flask. What techniques would allow researchers to perform structure-function studies on these molecules? Neurotransmitter structure and function can easily be probed through chemical synthesis. Medicinal chemists and

pharmacologists have been derivatizing and synthesizing analogs of neurotransmitters for decades to understand how their actions on neurons can be altered through changes to their chemical structures.

Studying neuroreceptors is substantially more difficult. Neuroreceptors are large membrane-bound proteins that often form multi-subunit signaling complexes. These features make them synthetically inaccessible. Even if these proteins could be synthesized chemically, they would need to be investigated in the proper context of the cell to fully assess their structure and function. Conventional mutagenesis combined with heterologous expression provides the proper *in vivo* context and has been used to determine important features of receptor structure. Unfortunately, the changes to protein structure available through conventional mutagenesis are severely limited. The twenty natural amino acids have limited chemical functionalities; there are no ketone, nitro, or ester moieties, to just name a few.

To illustrate this limitation of conventional mutagenesis, consider the cation-π interaction. Inorganic and organic cations have been shown to be stabilized through interactions with the π faces of aromatic rings[2–5]. These interactions are mainly electrostatic in nature. Cations are attracted to the negative charge density of the aromatic π face created by the quadropole moment of the ring. In biological structures, there is one cation-π interaction for every 77 amino acids in the protein data bank and 26% of all Trp residues are involved in cation-π interactions[4].

Despite its significance to protein structure, there is no means to study this interaction through conventional mutagenesis. Although there are differences in cation-π

binding energies between the three aromatic amino acids (Trp, Phe, Tyr), their structual differences are substantial enough that any effect in protein function could not solely be attributed to changes in a cation-π interaction. Ablating aromaticity at the site through Ala mutation would, of course, be even more destructive. An ideal experiment to study a Trp cation-π interaction would involve the progressive replacement of ring hydrogens with fluorines (Figure 1.2). Fluorination would decrease electron density on the π face of the ring through the atom's strong electronegativity. A change from hydrogen to fluorine would also be structurally subtle. Unfortunately, nature has not provided a codon that codes for fluorinated Trp.

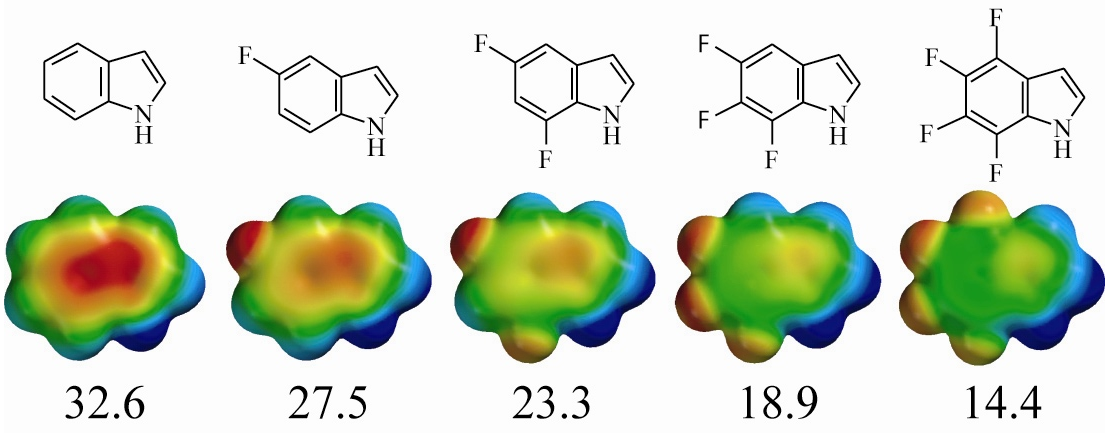


**Figure 1.2.** Fluorinated Trp analogs and cation-π binding energies. Electrostatic potential images show more negative charge density as red and more positive charge density as blue. Binding energies (kcal/mol) are from gas-phase calculations between fluorinated indole ring and sodium cation[2]

### *1.2.2 Incorporation of Unnatural Amino Acids into Neuroreceptors*

To provide researchers with the ability to specifically incorporate unnatural amino acids, such as a fluorinated Trp, into proteins for structure-function studies, the nonsense suppression methodology was developed by Schultz and co-workers in 1989[6–15]. In this

method, one of the cell's stop codons (UAG, the amber codon) serves as the *de facto* codon for the unnatural amino acid (Figure 1.3). A suppressor tRNA with an anticodon (CUA) that can recognize the stop codon is chemically appended with the unnatural amino acid of choice. Instead of terminating protein translation when the UAG codon is encountered, the ribosome incorporates the unnatural amino acid at the site of the stop codon as it would incorporate any standard amino acid. The protein is thus synthesized normally, with the unnatural amino acid incorporated at the site of interest.

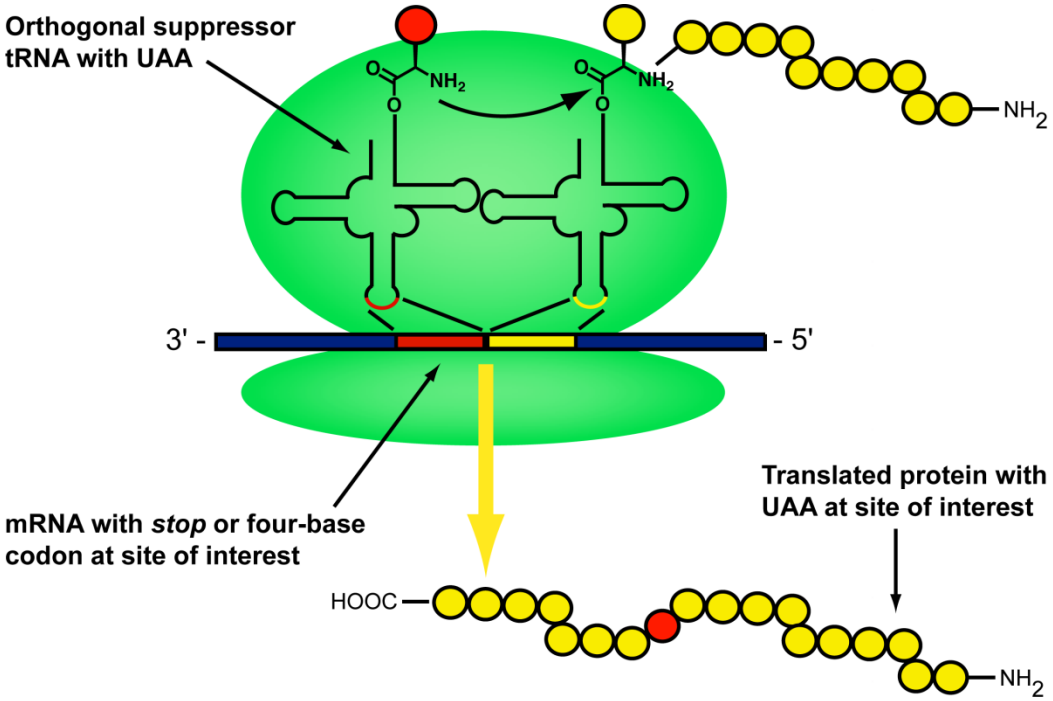


**Figure 1.3.** Overview of unnatural amino acid (UAA) incorporation using nonsense or frameshift suppression methodologies

Recently, an alternative method for incorporating unnatural amino acids has been developed, called frameshift suppression [16–18]. This methodology is similar to the nonsense suppression methodology, but codes for the unnatural amino acid through a four-base codon (GGGU) instead of a stop codon. A four-base codon normally shifts the ribosome out of the proper reading frame and produces mistranslated proteins. A

suppressor tRNA with the appropriate four-base anticodon (ACCC) that recognizes the four-base codon is used to suppress this shift in reading frame. By chemically appending an unnatural amino acid to this tRNA molecule, the ribosome incorporates the amino acid at the site of interest.

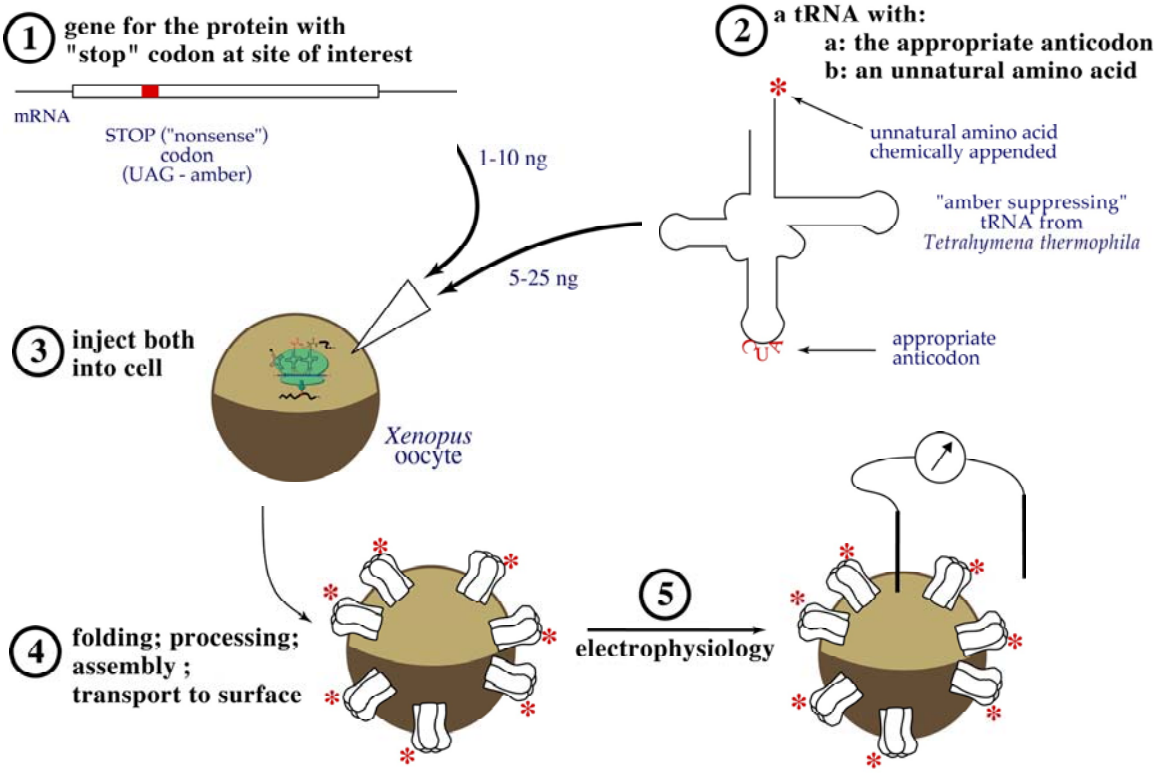


**Figure 1.4.** Implementation of nonsense suppression methodology for incorporating unnatural amino acids into membrane proteins in *Xenopus laevis* oocytes

In practice, both of these methodologies require a combination of chemical synthesis and simple molecular biology (Figure 1.4)[14,19–22]. The gene for the protein to be studied is mutated at the site of interest to either a stop or a four-base codon through standard mutagenesis protocols. Suppressor tRNA is transcribed without the last two nucleotides of the acceptor stem (C and A). A dinucleotide consisting of deoxy-C and A (dCA) is synthesized chemically and used as a chemical handle for the unnatural amino acid. Unnatural amino acids are prepared for use in these methodologies through the

addition of a photo- or $I_2$-labile amino protecting group (NVOC or 4-PO, respectively). Formation of a cyanomethyl ester from the free carboxylate activates the unnatural amino acid for acylation of the dCA molecule (Figure 1.5). Once acylated, the dCA molecule is ligated onto the truncated suppressor tRNA body with T4 RNA ligase to yield amino-acylated tRNA. Protection of the amino group of the unnatural amino acid provides stability to the amino-acylated tRNA.

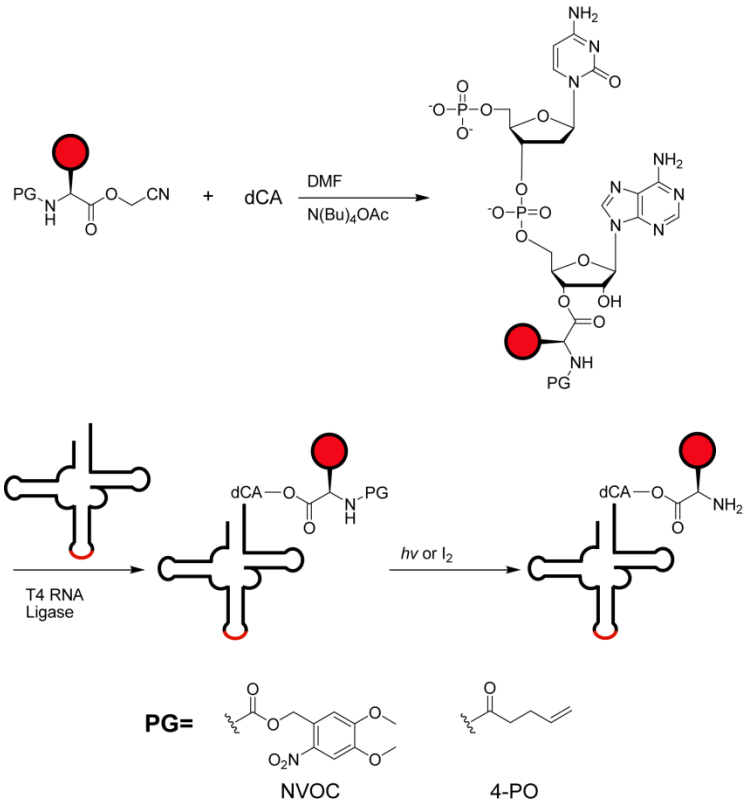


**Figure 1.5.** Method for chemically acylating unnatural amino acids (red circle) to the acceptor stem of suppressor tRNA

The mutated mRNA and amino-acylated tRNA are then injected into the cell type of choice, which in previous studies of neuroreceptors has been the *Xenopus laevis* oocyte[14,20,23–40]. An incubation period allows the proteins to be translated with the unnatural amino acid, processed, and transported to the surface of the cell. Several control experiments are performed along with the mutation experiment to ensure that the

unnatural amino acid has been properly incorporated into the protein. Injection of the mutant mRNA alone tests for readthrough of the stop or four-base codon by the ribosome. Injection of suppressor tRNA without an amino acid appended to the acceptor stem controls for misacylation—the phenomenon in which the cell's synthetases append a natural amino acid onto the tRNA body. Misacylation produces proteins that do not homogeneously contain the unnatural amino acid at the site of interest. Finally, wild-type recovery experiments, in which the suppressor tRNA is amino-acylated with the wild-type amino acid, ensure that proper protein function can be recovered through the nonsense or frameshift suppression methodology.

Because the suppressor tRNA cannot be amino-acylated within the cell with more unnatural amino acid, the suppressor tRNA is a stoichiometric reagent; protein yields cannot exceed the amount of tRNA injected into the cell. Fortunately, studies of neuroreceptors can be assayed through methods that do not require large amounts of protein. Electrophysiology is an extremely sensitive assay for ion channel function that detects currents through whole cells or patches of cell membranes. In fact, single ion channels can be monitored through these assays. When a drug is applied to the cell, ion channels on the cell's surface gate and pass ions into or out of the cell (Figure 1.6a). The aggregate passage of ions by these ion channels produces a cell current that can be measured using the two-electrode voltage clamp method[41,42]. When the concentration of drug increases, these currents also increase as more receptors become active (Figure 1.6bc).

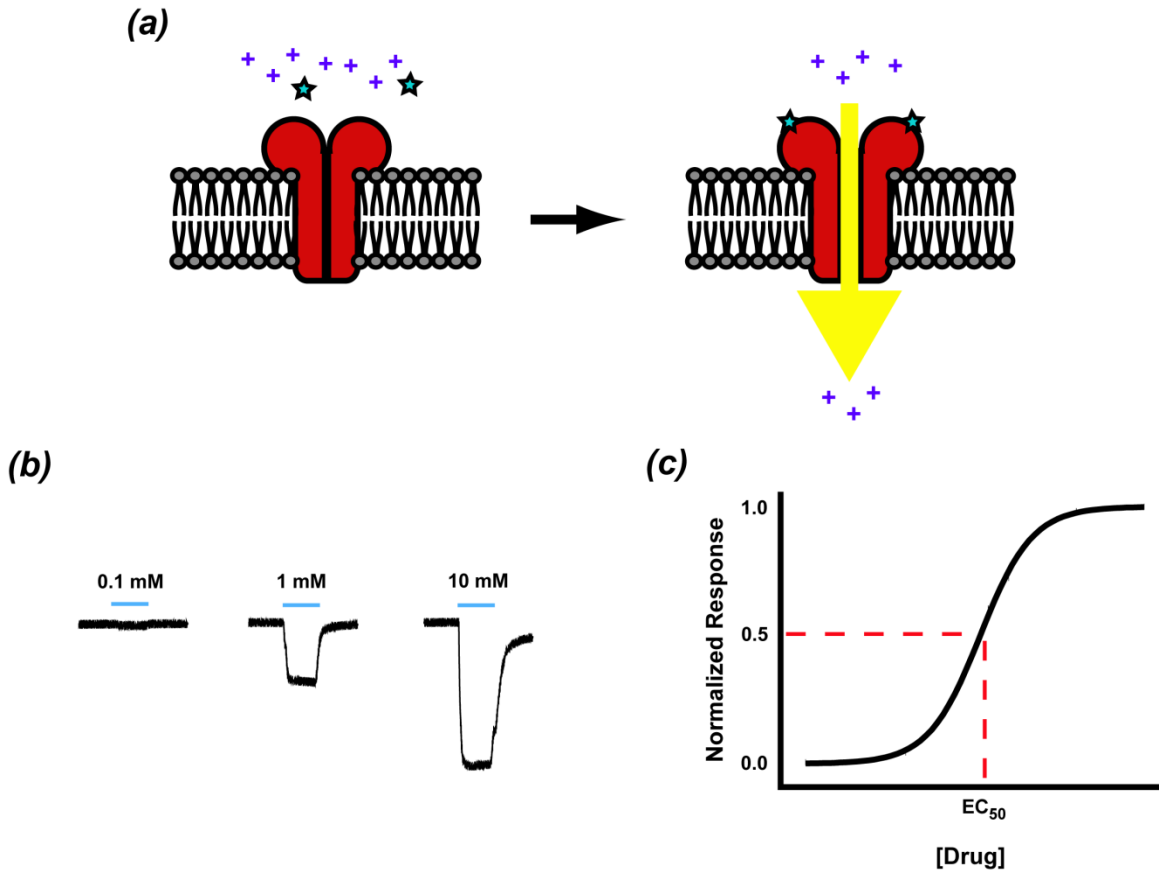


**Figure 1.6.** Basics of electrophysiology assay. ***(a)*** Drug (stars) binding to LGIC promotes receptor gating. Once open, the channel allows current to pass in or out of the cell producing current signals. ***(b)*** Examples of current response to varying concentrations of drug. From *left* to *right*, low, $EC_{50}$, and saturating drug concentrations. ***(c)*** Example of dose-response relationship. $EC_{50}$ definition shown in relation to the rest of the curve

A drug's potency at a receptor can be established through such a dose-response relationship (Figure 1.6c). Potency of a drug for a given neuroreceptor is a combination of the drug's binding affinity and its ability to promote receptor activation (efficacy). Mutations to residues in the binding site of the receptor are assumed mainly to affect affinity, although there are notable exceptions. Typically, those mutations along the gating/activation pathway of the receptor are thought to mainly affect efficacy.

$EC_{50}$, the dose of drug that elicits a half-maximal response in the receptor (Figure 1.6c), is a means to quantitate drug potency, and thus contains information about both

drug affinity and efficacy. Changes in receptor function are reported through shifts in $EC_{50}$ values: a shift to higher $EC_{50}$ values implies a loss-of-function mutation and, accordingly, shifts to lower $EC_{50}$ values suggest gain-of-function. By combining unnatural amino acid mutagenesis with these electrophysiology experiments, the role of specific chemical interactions in the function of large neuroreceptors can be assayed.

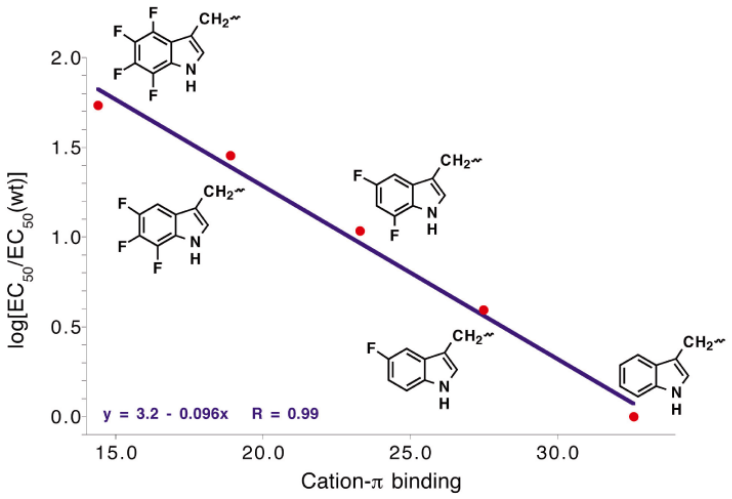


**Figure 1.7.** Classic Zhong plot for αW149 residue of nAChR. Calculated cation-π binding energy (gas phase) is plotted against the log of the ratio of the $EC_{50}$ of the $F_n$Trp mutant receptor to the wild-type receptor $EC_{50}$[40]

A classic early example of this coupling of unnatural amino acid mutagenesis and electrophysiology is the discovery of a cation-π interaction between acetylcholine (ACh) and a binding site residue in the nicotinic ACh receptor (nAChR)[40]. This early study probed a Trp in the α subunit of the nAChR (αW149) for an interaction with the positively charged quaternary amine of ACh. A series of fluorinated Trp amino acids (Figure 1.2) were incorporated at αW149 and the effect on $EC_{50}$ was measured. $EC_{50}$ values progressively shifted upwards with each fluorination (Figure 1.7), and thus suggested that a cation-π interaction existed between the indole ring of αW149 and the quaternary amine of ACh.

## 1.3 Dissertation Work

This dissertation describes three studies that utilized this combination of unnatural amino acid mutagenesis and electrophysiology. The three studies probed the structure and function of two different ACh receptors, the nAChR and the $M_2$ muscarinic ACh receptor ($M_2$AChR). Chapters 2 and 3 outline binding site studies, while Chapter 4 studies gating. In Chapter 2, we descibe an investigation into the role of a highly conserved Asp in the nAChR binding site. Using subtle mutations only available through unnatural amino acids, we determine that this residue is responsible for preorganizing a key region of the nAChR binding site for ligand binding. Chapter 3 discusses our attempts to incorporate unnatural amino acids into a GPCR ($M_2$AChR), a type of neuroreceptor we had not previously studied through this methodology. We determined optimal conditions that allowed us to obtain robust and reliable data from GPCRs. Initial data on the search for a cation-$\pi$ interaction between ACh and aromatic residues in the $M_2$AChR binding site are also discussed. Finally, in Chapter 4, we describe a study of the $\alpha$M1 transmembrane helix of the nAChR using hydroxy acids. This study sought to determine the nature of structural rearrangements in the helix during channel gating.

## 1.4 References

(1) Kandel, E. R.; Schwartz, J. H.; Jessel, T. M. *Principles of Neural Science, 4th ed.* McGraw-Hill: New York, NY, 2000.
(2) Ma, J. C.; Dougherty, D. A. *Chem. Rev.* **1997**, *97*, 1303–1324.

(3) Dougherty, D. A. *Science* **1996**, *271*, 163–168.
(4) Gallivan, J. P.; Dougherty, D. A. *Proceedings of the National Academy of Sciences of the United States of America* **1999**, *96*, 9459–9464.
(5) Zacharias, N.; Dougherty, D. A. *Trends in Pharmacological Sciences* **2002**, *23*, 281–287.
(6) Chapman, E.; Thorson, J. S.; Schultz, P. G. *J. Am. Chem. Soc.* **1997**, *119*, 7151–7152.
(7) Chung, H. H.; Benson, D. R.; Schultz, P. G. *Science* **1993**, *259*, 806–809.
(8) Cornish, V. W.; Benson, D. R.; Altenbach, C. A.; Hideg, K.; Hubbell, W. L.; Schultz, P. G. *Proceedings of the National Academy of Sciences of the United States of America* **1994**, *91*, 2910–2914.
(9) Cornish, V. W.; Mendel, D.; Schultz, P. G. *Angewandte Chemie—International Edition in English* **1995**, *34*, 621–633.
(10) Ellman, J. A.; Mendel, D.; Schultz, P. G. *Science* **1992**, *255*, 197–200.
(11) Judice, J. K.; Gamble, T. R.; Murphy, E. C.; de Vos, A. M.; Schultz, P. G. *Science* **1993**, *261*, 1578–1581.
(12) Koh, J. T.; Cornish, V. W.; Schultz, P. G. *Biochemistry* **1997**, *36*, 11314–11322.
(13) Noren, C. J.; Anthonycahill, S. J.; Griffith, M. C.; Schultz, P. G. *Science* **1989**, *244*, 182–188.
(14) Nowak, M. W.; Kearney, P. C.; Sampson, J. R.; Saks, M. E.; Labarca, C. G.; Silverman, S. K.; Zhong, W.; Thorson, J.; Abelson, J. N.; Davidson, N.; Schultz, P. G.; Dougherty, D. A.; Lester, H. A. *Science* **1995**, *268*, 439–442.
(15) Thorson, J. S., Chapman, E., Schultz, P.G. *Journal of the American Chemical Society* **1995**, *117*, 9361–9362.
(16) Hohsaka, T.; Ashizuka, Y.; Murakami, H.; Sisido, M. *Journal of the American Chemical Society* **1996**, *118*, 9778–9779.
(17) Hohsaka, T.; Ashizuka, Y.; Taira, H.; Murakami, H.; Sisido, M. *Biochemistry* **2001**, *40*, 11060–11064.
(18) Rodriguez, E. A.; Lester, H. A.; Dougherty, D. A. *Proc Natl Acad Sci U S A* **2006**, *103*, 8650–5.
(19) Beene, D. L.; Dougherty, D. A.; Lester, H. A. *Current Opinion in Neurobiology* **2003**, *13*, 264–270.
(20) Dougherty, D. A. *Current Opinion in Chemical Biology* **2000**, *4*, 645–652.
(21) Kearney, P. C.; Nowak, M. W.; Zhong, W.; Silverman, S. K.; Lester, H. A.; Dougherty, D. A. *Mol Pharmacol* **1996**, *50*, 1401–1412.
(22) Nowak, M. W.; Gallivan, J. P.; Silverman, S. K.; Labarca, C. G.; Dougherty, D. A.; Lester, H. A.; Conn, P. M. *Methods in Enzymology* **1998**, *293*, 504–529.
(23) Beene, D. L.; Brandt, G. S.; Zhong, W.; Zacharias, N. M.; Lester, H. A.; Dougherty, D. A. *Biochemistry* **2002**, *41*, 10262–10269.
(24) Beene, D. L.; Price, K. L.; Lester, H. A.; Dougherty, D. A.; Lummis, S. C. R. *J. Neurosci.* **2004**, *24*, 9097–9104.
(25) Cashin, A. L.; Petersson, E. J.; Lester, H. A.; Dougherty, D. A. *J. Am. Chem. Soc.* **2005**, *127*, 350–356.
(26) Cashin, A. L.; Torrice, M. M.; McMenimen, K. A.; Lester, H. A.; Dougherty, D. A. *Biochemistry* **2007**, *46*, 630–639.

(27) Dang, H.; England, P. M.; Farivar, S. S.; Dougherty, D. A.; Lester, H. A. *Mol Pharmacol* **2000**, *57*, 1114–1122.
(28) Dougherty, D. A. *J. Org. Chem.* **2008**, *73*, 3667–3673.
(29) Dougherty, D. A. *Chem. Rev.* **2008**, *108*, 1642–1653.
(30) England, P. M.; Lester, H. A.; Dougherty, D. A. *Tetrahedron Letters* **1999**, *40*, 6189–6192.
(31) England, P. M.; Zhang, Y.; Dougherty, D. A.; Lester, H. A. *Cell* **1999**, *96M1 nAChR*, 89–98.
(32) Li, L. T.; Zhong, W. G.; Zacharias, N.; Gibbs, C.; Lester, H. A.; Dougherty, D. A. *Chemistry & Biology* **2001**, *8*, 47–58.
(33) Lummis, S. C. R.; Beene, D. L.; Lee, L. W.; Lester, H. A.; Broadhurst, R. W.; Dougherty, D. A. *Nature* **2005**, *438*, 248–252.
(34) Lummis, S. C. R.; L. Beene, D.; Harrison, N. J.; Lester, H. A.; Dougherty, D. A. *Chemistry & Biology* **2005**, *12*, 993–997.
(35) McMenimen, K. A.; Petersson, E. J.; Lester, H. A.; Dougherty, D. A. *ACS Chem. Biol.* **2006**, *1*, 227–234.
(36) Mu, T. W.; Lester, H. A.; Dougherty, D. A. *J. Am. Chem. Soc.* **2003**, *125*, 6850–6851.
(37) Padgett, C. L.; Hanek, A. P.; Lester, H. A.; Dougherty, D. A.; Lummis, S. C. R. *J. Neurosci.* **2007**, *27*, 886–892.
(38) Petersson, E. J.; Choi, A.; Dahan, D. S.; Lester, H. A.; Dougherty, D. A. *J. Am. Chem. Soc.* **2002**, *124*, 12662–12663.
(39) Xiu, X.; Hanek, A. P.; Wang, J.; Lester, H. A.; Dougherty, D. A. *J. Biol. Chem.* **2005**, *280*, 41655–41666.
(40) Zhong, W.; Gallivan, J. P.; Zhang, Y.; Li, L.; Lester, H. A.; Dougherty, D. A. *PNAS* **1998**, *95*, 12088–12093.
(41) Hodgkin, A. L.; Huxley, A. F. *Cold Spring Harbor symposia on quantitative biology* **1952**, *17*, 43–52.
(42) Hodgkin, A. L.; Huxley, A. F. *J. Physiol.* **1952**, *117*, 500–544.

# **Chapter 2:** Chemical-Scale Studies on the Role of a Conserved Aspartate in Preorganizing the Agonist Binding Site of the Nicotinic Acetylcholine Receptor*

## 2.1 Introduction

### *2.1.1 The Nicotinic Acetylcholine Receptor*

Neuroreceptors are central players in synaptic transmission, receiving and interpreting chemical signals between neurons in the nervous system. Neuroreceptors of the ligand-gated ion channel (LGIC) family directly convert incoming chemical signals into electrical output. In the LGIC gating process, neurotransmitters are recognized by ligand-binding domains, and binding triggers conformational changes within the structure to form an ion-conducting pore.

The nicotinic acetylcholine receptor (nAChR) has served as a prototype for understanding the structure and function of the Cys-loop family of LGICs (also known as pentameric LGICs). In this superfamily of receptors, which also includes γ-aminobutyric acid, glycine, and serotonin receptors, the five subunits are symmetrically or pseudosymmetrically arranged around a central ion-conducting pore. Each subunit contains a four-helix transmembrane domain that contains the ion channel gate and an extracellular ligand-binding domain. Members of the nAChR family are expressed at the neuromuscular junction and in the electric organ of eels and rays (muscle-type receptors), as well as in the central nervous system (neuronal receptors). The muscle-type receptor

is the best characterized, and the form studied here is the embryonic muscle nAChR, with a subunit stoichiometry of two α1 subunits and one each of the β1, γ, and δ subunits[1]. The nAChR has two agonist binding sites located at the α/γ and α/δ subunit interfaces[2–4]. The α subunits contribute the primary binding site components, termed loops A, B, and C, while the γ and δ subunits contribute the complementary components, primarily loop D (with possible contributions from loops E and F). The focus of this chapter is on loops A and B of the α subunit.

Work over the past several years on acetylcholine binding protein (AChBP) orthologs from mollusks has led to important new insights into the structures of Cys-loop receptor ligand-binding domains[5–8]. AChBP is a soluble, homopentameric protein produced in glial cells that is homologous to the nAChR ligand-binding domain. Crystal structures of AChBP with various agonists bound have established that the nAChR binding site is comprised of a box of conserved aromatic residues. One of these conserved aromatic residues is a tryptophan on loop B, W149 (Figures 2.1 and 2.2). Previous studies by this lab established that this tryptophan makes a strong cation-π interaction with ACh in the muscle-type receptor [9], and its role as a component of the AChBP "aromatic box" confirmed those findings. Subsequent work showed that the potent nicotinic agonist epibatidine also makes a cation-π interaction with W149 [9,10]. Nicotine is a quite weak agonist at the muscle-type receptor and does not form a cation-π interaction; its actions at the neuronal receptors are more substantial.

### *2.1.2 Previous Studies of D89/Loop B Interactions*

The AChBP crystal structures suggest other important ligand-binding domain interactions that require verification through experiment. One structurally interesting interaction involves a conserved aspartate on loop A, D89[6]. This residue is part of a highly conserved WxPD motif exhibited across the entire Cys-loop superfamily (Figure 2.1). In the crystal structures of AChBP, D89 is positioned to interact with loop B through any of a number of hydrogen bonds between the aspartate carboxylate side chain and loop B residues T148, W149, and T150 (Figure 2.2). For the purposes of discussion, a schematic of the putative hydrogen bonding network, with potential hydrogen bonds labeled, is shown in Figure 2.3a. The high degree of conservation of the WxPD motif and the clear interaction of D89 with a known component of the agonist binding site (loop B/W149) have generated considerable interest in D89. Note that loop A also contains a canonical contributor to the aromatic box, Y93.

| | loop A | loop B |
|---|---|---|
| AChBP | SL**W**V**PD**LAAYN | IG**SWT**H |
| mmα1 | KI**W**R**PD**VVLYN | LG**TWT**Y |
| hα7 | QI**W**K**PD**ILLYN | FG**SWS**Y |
| hGly- α1 | SI**W**K**PD**MFFVH | IE**SY**AY |
| h5-$HT_3$A | SI**W**V**PD**ILINE | FE**SYS**H |

**Figure 2.1.** Alignment of loops A and B for several Cys-loop receptors. The WxPD motif of loop A and the region around W149 of loop B are highlighted in red and blue, respectively. AChBP: ACh binding protein from *Limnaea stagnalis*; mmα1: nAChR α 1 subunit of mouse muscle (studied here); hα7: human nAChR α7 subunit; hGly- α1: human glycine receptor α1 subunit; h5-$HT_3$A: human 5-$HT_3$ A subunit. Y93 shown in green in the mmα1 sequence.

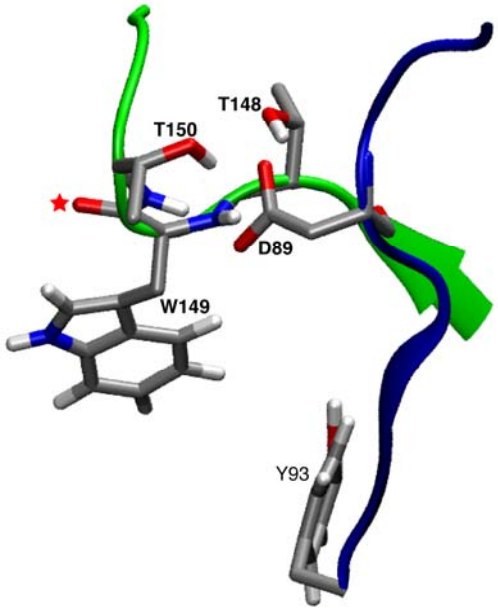


**Figure 2.2.** Region investigated in the Chapter 2 study. Loop A is shown in blue; loop B in green. Highlighted are the side chains of D89, T148, and T150, which together can form a network of hydrogen bonds. Also shown are contributors to the agonist binding site: Y93 from loop A; W149 side chain and W149 backbone carbonyl (red star) from loop B. This carbonyl and the side chain of Trp 149 point directly at the agonist, which in this view lies "behind" loop B. This image results from MD simulations, as discussed in text.

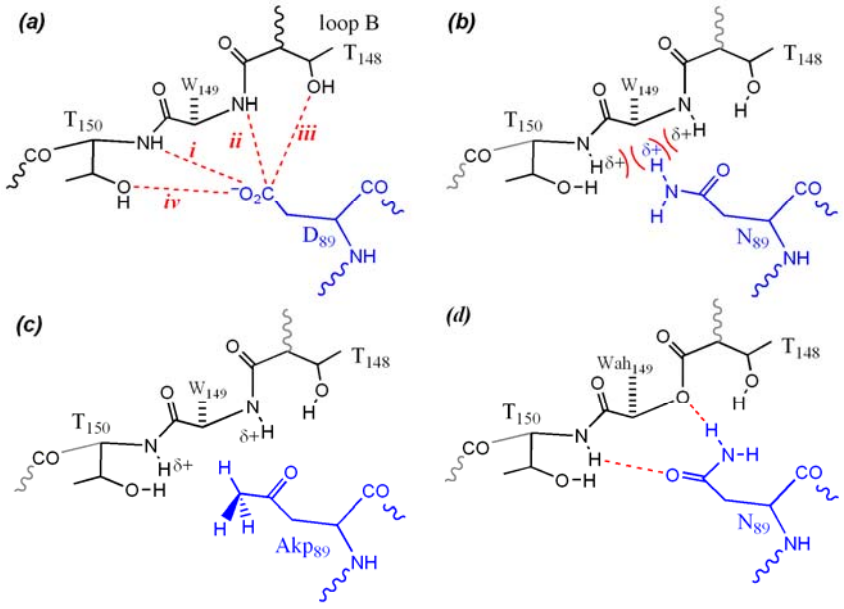


**Figure 2.3.** Schematics of potential hydrogen bonding interactions between loops A (blue) and B (black). ***(a)*** The wild type receptor. ***(b)*** D89N, highlighting the potential electrostatic clash. ***(c)*** D89Akp; note the lack of an electrostatic clash. ***(d)*** The double mutant D89N/W149Wah; note how hydrogen bond *ii* could, in principle, be restored.

Recently, Lee and Sine[11] have investigated D89 and its role in agonist binding by combining site-directed mutagenesis with single-channel kinetic analyses. Neutralization of the negative charge at position 89 through a mutation to asparagine or threonine, (D89N and D89T, respectively) substantially compromised receptor function, producing significant decreases in the bimolecular forward rate constant for agonist-receptor binding. In contrast, mutating residues T148 and T150, singly and in combination, did not seriously impact function. From these results, Lee and Sine concluded that D89 plays a structural role in stabilizing loop B, in particular W149, for agonist association. They concluded that essential structural features of the D89/loop B network were the negative charge of D89 and hydrogen bonds between the aspartate carboxylate and the amide backbones of T150 and T149 (hydrogen bonds *i* and *ii* in Figure 2.3a). They also proposed that a possible polarization of the backbone carbonyl of W149 contributes to ACh binding[6].

### *2.1.3 Project Goals*

In the present study, we sought to further probe the role of the conserved D89 in the nAChR ligand-binding domain. Through the incorporation of unnatural amino acids using two different suppression methodologies[12–15], we introduced more subtle modifications to the side chain of D89, allowing what we have termed "chemical-scale" studies of such complex receptors. By chemical scale we mean, in effect, the distance scale to which chemists are accustomed: the functional group, the specific bond rotation or local conformational change, or the precise noncovalent interaction. We have also

incorporated amide-to-ester backbone mutations into loop B to probe proposed hydrogen bonds to this region. We conclude that the significantly disruptive D89N mutation affects receptor function in several ways: a distortion of the hydrogen bonding network, the introduction of an electrostatic clash between the asparagine amide side chain and the backbone amides of loop B, and, to a lesser extent, a neutralization of charge. We also find that, of the network of hydrogen bonds implied by the AChBP structure (Figure 2.3a), no one hydrogen bond is singularly important. Rather, maintaining the overall network of hydrogen bonds and avoiding electrostatic and/or steric clashes are essential for proper function. To support our unnatural amino acid mutagenesis studies, we conducted molecular dynamics simulations of the wild-type and D89N mutant ligand-binding domains in an effort to evaluate the hydrogen bonding network.

## 2.2 Results

### *2.2.1 Conventional Mutants, D89N and D89E*

In this project, we evaluated receptors using the macroscopic parameter $EC_{50}$, the effective concentration of agonist necessary to achieve half-maximal response, rather than the more information rich, but more time consuming, single-channel analyses of Lee and Sine[11]. We made this choice both to examine a large number of mutants and to avoid the additional challenges of performing single-channel studies at the low expression levels often associated with unnatural amino acid mutagenesis. Of course, $EC_{50}$ is a composite value that could be influenced by changes in agonist affinity or in gating. Since the mutations we are evaluating are proximal to the agonist binding site and are

quite remote from the gate of the channel, we interpret changes in $EC_{50}$ as affecting binding more than gating. Consistent with this view, single-channel analyses of several D89 mutants reveal much more substantial changes in binding parameters than in gating parameters[11].

For comparison, we first studied two conventional mutants, D89N and D89E, that were also studied by Lee and Sine. The D89E mutant produced a modest 4-fold increase in $EC_{50}$ for both ACh and epibatidine. However, the D89N mutant produced substantial 23- and 28-fold increases in $EC_{50}$ for ACh and epibatidine, respectively (Table 2.1). Our results parallel the single-channel work, in which D89N produced a significant decrease in rate constants for ACh association while D89E resulted in a modest decrease in association rates and barely any change in the overall agonist binding equilibria.

### *2.2.2 Unnatural Mutants, D89Nha and D89Akp*

Unnatural amino acids were incorporated at D89 through frame-shift suppression, instead of nonsense suppression. We used the frame-shift methodology because of the high level of misacylated THG73 incorporation at this position. Currents with an average magnitude of 0.29 ± 0.03 μA (Figure 2.4a) were observed when we performed the misacylation control experiment (injection of 74 nt THG73 tRNA). The dose-response relationship for this misacylation current ($EC_{50}$ = 1.2 ± 0.1 μM; Figure 2.4b) suggested that Asp or Glu may have been the amino acid on the misacylated tRNA. When we performed a similar control experiment with the frame-shift suppressor tRNA, YFaFS, we observed negligible misacylation currents (0.05 ± 0.01 μA; Figure 2.4a).

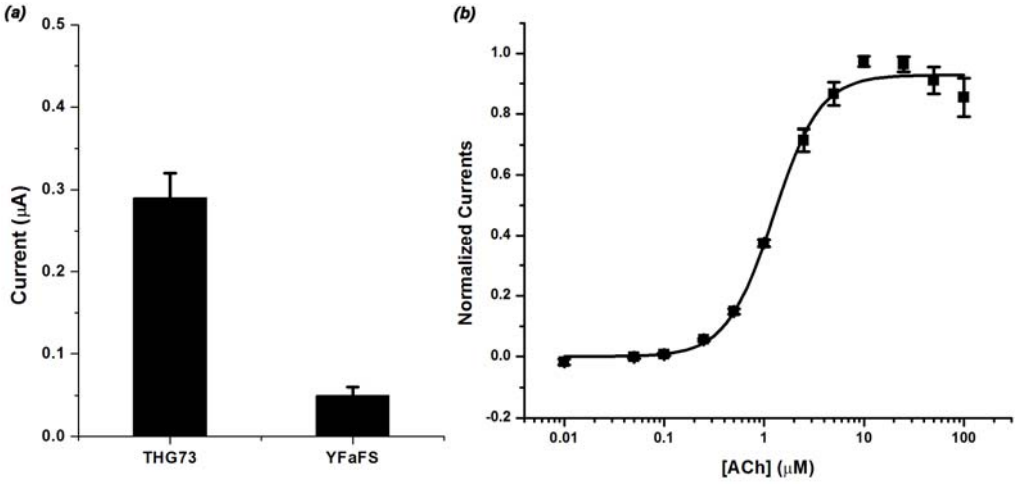


**Figure 2.4.** D89 misacylation data. ***(a)*** Comparison of currents from the misacylation control experiment for nonsense suppression (injection of 74 nt THG73 tRNA) and frame-shift suppression (injection of 74 nt YFaFS tRNA). Currents were 0.29 ± 0.03 μA for THG73 (N = 13) and 0.05 ± 0.01 μA for YFaFS (N = 5). ***(b)*** Dose-response relationship for misacylated THG73 currents. Hill equation parameters: $EC_{50}$ = 1.2 ± 0.1 μM, $n_H$ = 1.9 ± 0.2, N = 6 cells

The essential role of D89 is confirmed by the large perturbation of the D89N mutant. While generally considered a subtle change, an Asp-to-Asn mutation does more than simply neutralize charge. It also replaces a hydrogen-bond-accepting O atom with a hydrogen-bond-donating $NH_2$ group, and in the context of this system, this change introduces a possible electrostatic clash between position 89 and loop B (Figure 2.3b). The amide side chain of asparagine places an $N^{\delta-}$–$H^{\delta+}$ bond dipole proximal to the $N^{\delta-}$–$H^{\delta+}$ bond dipoles of the loop B amide backbone at T150 and W149. This possible repulsive interaction between the $N^{\delta-}$–$H^{\delta+}$ dipoles could contribute to the deleterious effects of the D89N mutant.

In an attempt to dissect these two features of the D89N mutant, we incorporated two unnatural amino acids that neutralize the negative charge of Asp without introducing an electrostatic clash. A nitro group ($NO_2$) is isoelectronic and isosteric to a carboxylate, but it has no negative charge (Figure 2.5). Also, a nitro group is a substantially weaker

hydrogen bond acceptor than carboxylate[16]; the measured difference in energetics of carboxylate and nitro hydrogen bonding is 1.5–2.0 kcal/mol[17], corresponding to a factor of 10–20 in an equilibrium constant. The ideal residue would be nitroalanine (Noa), the nitro analog of Asp, but it is not chemically compatible with the nonsense suppression methodology (see Appendix A for details). Therefore, we studied nitrohomoalanine (Nha), the nitro analog of Glu (Figure 2.6). Since the D89E mutant produces only a modest change in receptor function, comparing the Nha mutant to the Glu mutant was deemed meaningful.

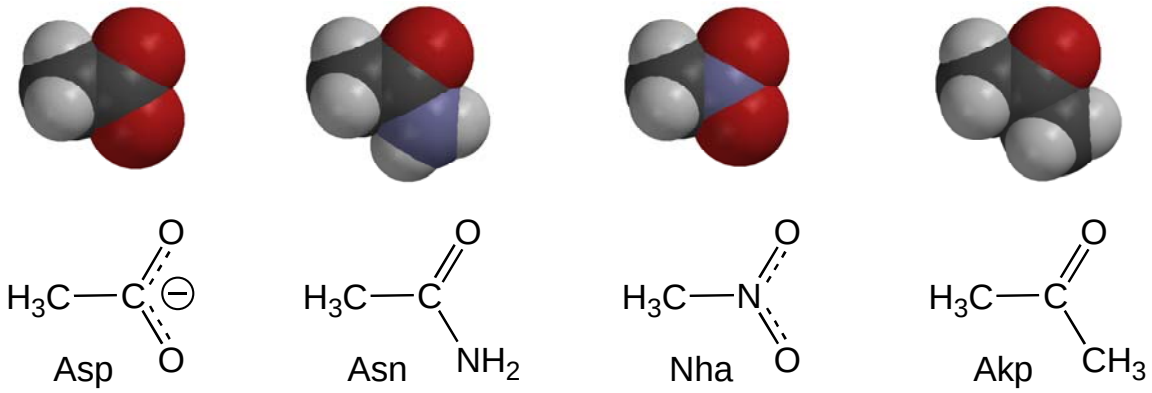


**Figure 2.5.** Functionalities of side chains used in Chapter 2. Space-filling models shown. Note the greater steric similarity between Asp and Nha and between Asn and Akp.

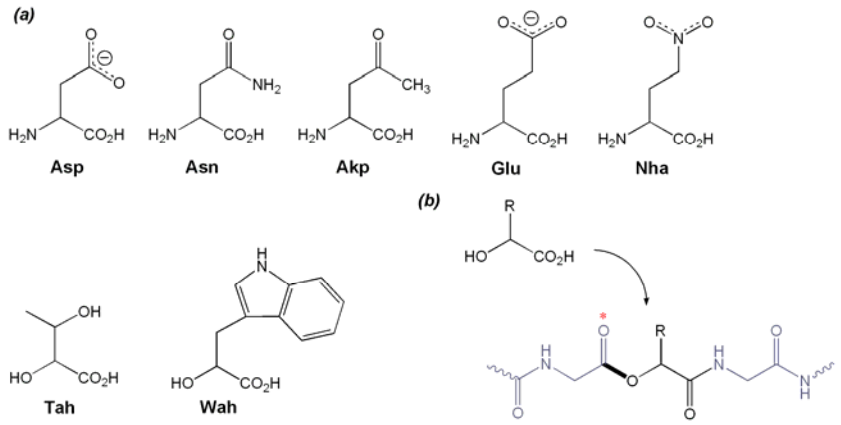


**Figure 2.6.** Structures of hydroxyl acids, natural, and unnatural amino acids used in Chapter 2. ***(a)*** Natural and unnatural amino (and hydroxy) acids structures. ***(b)*** Consequences of incorporating an α-hydoxy acid into a protein. The critical ester linkage is highlighted in bold; the carbonyl that is modulated is noted with a star.

**Table 2.1.** D89 Mutants[a]

| | | Wild Type[b] | D89N[b] | D89E[b] | D89Nha | D89Akp |
|---|---|---|---|---|---|---|
| **ACh** | $EC_{50}$ | 0.83 ± 0.04 | 19 ± 1 | 3.4 ± 0.3 | 14 ± 1 | 8.0 ± 0.7 |
| | $n_H$ | 1.8 ± 0.1 | 1.6 ± 0.1 | 1.6 ± 0.1 | 1.3 ± 0.1 | 1.7 ± 0.2 |
| | N | 22 | 8 | 9 | 8 | 5 |
| **Epi** | $EC_{50}$ | 0.60 ± 0.04 | 13 ± 1 | 2.4 ± 0.1 | 11 ± 1 | 5.0 ± 0.5 |
| | $n_H$ | 1.6 ± 0.1 | 2.0 ± 0.2 | 1.7 ± 0.2 | 1.7 ± 0.3 | 1.5 ± 0.2 |
| | N | 22 | 5 | 3 | 8 | 5 |

[a]$EC_{50}$ (μM) and Hill coefficient ± standard error of the mean. The receptor has a Leu9'Ser mutation in M2 of the β subunit. [b]Data reported previously[10,18]

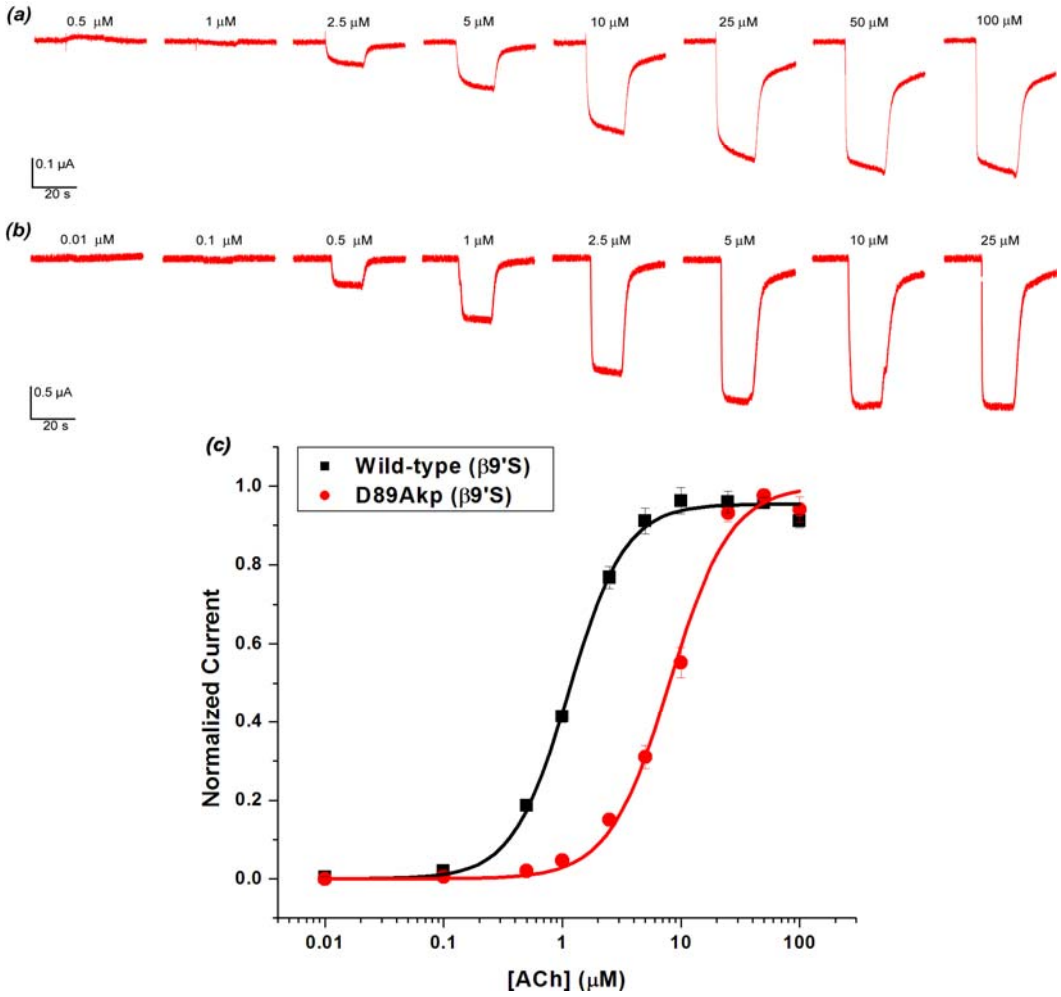


**Figure 2.7.** Representative dose-response relationships for D89Akp ***(a)*** and D89 wild-type recovery ***(b)***. ***(c)*** Data from same conditions as ***(a)*** and ***(b)*** fit to the Hill equation

Incorporation of Nha at position 89, D89Nha, resulted in a modest 4-fold increase in $EC_{50}$ when compared to that of the isosteric D89E receptor for both ACh and

epibatidine (Table 2.1). This change is comparable to that of the original D89E mutation. The D89Nha mutant behavior suggests that charge neutralization is no more deleterious than an increase in side chain length at position 89.

The second neutral unnatural amino acid we incorporated was 2-amino-4-ketopentanoic acid (Akp; Figure 2.6), producing D89Akp. Akp is a direct analog of Asp, and the ketone side chain of Akp is sterically similar to the Asp and especially the Asn side chains (Figure 2.5 and 2.6). However, Akp lacks the $N^{\delta-}$–$H^{\delta+}$ bond dipole (Figure 2.3c), and so does not contribute an electrostatic clash. When Akp was incorporated at position 89, 8- and 10-fold increases in $EC_{50}$ were observed for ACh and epibatidine, respectively, relative to that of wild type (Table 2.1 and Figure 2.7). The ~ 2.5-fold difference in $EC_{50}$ between the D89Akp and D89N receptors can be attributed to the electrostatic clash produced by the Asn $N^{\delta-}$–$H^{\delta+}$ dipole.

**Table 2.2.** Nicotine Data[a]

| | **Wild Type**[b] | **D89E**[b] | **D89N**[b] | **D89Nha** | **D89Akp** |
|---|---|---|---|---|---|
| **$EC_{50}$** | 57 ± 2 | 59 ± 6 | 1600 | 270 ± 60 | 110 ± 10 |
| **$n_H$** | | | | 1.9 ± 0.5 | 2.7 ± 0.6 |
| **N** | | | | 9 | 5 |

[a]$EC_{50}$ (μM) and Hill coefficient ± standard error of the mean. The receptor has a Leu9'Ser mutation in M2 of the β subunit. [b]Data reported previously[18]

These two unnatural amino acid mutations were also studied with nicotine as the agonist. While nicotine is a full agonist at neuronal receptors, it is a weak partial agonist at the muscle type of nAChR. Incorporation of Nha produced a 4.5-fold shift in nicotine $EC_{50}$ relative to that of the D89E mutant, and the incorporation of Akp produced an almost 2-fold shift relative to that of wild-type (Table 2.2). (Unlike ACh and epibatidine, the D89E mutation did not shift the nicotine $EC_{50}$; the wild-type nicotine $EC_{50}$ was 57 ± 2

μM and the the D89E mutant $EC_{50}$ was 59 ± 6 μM[18].) The negative charge of Asp appears to be of equal importance to nicotine as it is with ACh and epibatidine. But, when compared to the D89N mutation ($EC_{50}$ = ~ 1600 μM[18]), the slight shift in $EC_{50}$ caused by the D89Akp mutation suggests that the electrostatic clash of Asn affects nicotine binding more than ACh and epibatidine.

### *2.2.3 Loop B Backbone Mutations*

Of the four possible hydrogen bonds in the D89/loop B network, two involve side-chain–to–side-chain interactions, and two involve hydrogen bonds with the loop B amide backbone (Figure 2.3a). The side chain interactions (*iii* and *iv*) have been probed by conventional mutagenesis[11]. T148L, T150A, and T148L/T150A mutants were not substantially disruptive, suggesting hydrogen bonds *iii* and *iv* are not crucial. By inference, backbone hydrogen bonds *i* and *ii* have been proposed to be especially critical to receptor function[11].

**Table 2.3.** Loop B and Double Mutants[a]

| | | **Wild Type** | **T150Tah** | **W149Wah** | **D89N** | **D89N / T150Tah** | **D89N / W149Wah** |
|---|---|---|---|---|---|---|---|
| **ACh** | $EC_{50}$ | 0.83 ± 0.04 | 0.25 ± 0.01 | 0.81 ± 0.03 | 19 ± 1 | 15 ± 1 | 2.2 ± 0.1 |
| | $n_H$ | 1.8 ± 0.1 | 1.4 ± 0.04 | 1.6 ± 0.1 | 1.6 ± 0.1 | 1.4 ± 0.2 | 1.8 ± 0.1 |
| | N | 22 | 17 | 7 | 8 | 7 | 6 |
| **Epi** | $EC_{50}$ | 0.60 ± 0.04 | 2.2 ± 0.2 | 1.6 ± 0.1 | 13 ± 1 | 2.9 ± 0.3 | 0.76 ± 0.05 |
| | $n_H$ | 1.6 ± 0.1 | 1.3 ± 0.1 | 1.6 ± 0.1 | 2.0 ± 0.2 | 1.2 ± 0.1 | 1.7 ± 0.1 |
| | N | 22 | 16 | 5 | 5 | 6 | 6 |

[a] $EC_{50}$ (μM) and Hill coefficient ± standard error of the mean. The receptor has a Leu9'Ser mutation in M2 of the β subunit. Data reported previously[10,18]

Probing backbone hydrogen bonds requires the power of unnatural amino acid mutagenesis. Appropriate amide-to-ester mutations remove the backbone NH group that

can contribute to the hydrogen bond (Figure 2.6b). In this system, the T150Tah mutation disrupts hydrogen bond *i*, and the W149Wah mutation disrupts hydrogen bond *ii*. The W149Wah mutation produced very modest effects (Table 2.3), suggesting that hydrogen bond *ii* is nonessential.

The T150Tah mutation has been studied previously[10]. It is unique among the mutations considered here in that the results for ACh and epibatidine are qualitatively different; the $EC_{50}$ for ACh decreased ~ 3-fold, while that for epibatidine increased ~ 4-fold. Ester backbones not only eliminate a hydrogen bond donor in the backbone, but also weaken the corresponding (adjacent) carbonyl as a hydrogen bond acceptor. The carbonyl perturbed by the T150Tah mutation, the W149 backbone carbonyl (*star* in Figures 2.2 and 2.6b), points away from the region being probed here and directly into the agonist binding site. Epibatidine can make a hydrogen bond to this carbonyl, and the ester mutation weakens the hydrogen-bond-accepting ability of the carbonyl, accounting for the increase in $EC_{50}$. No such hydrogen bond is possible for ACh. As such, we consider ACh the better gauge of the importance of hydrogen bond *i*, and we ascribe a nonessential role for it.

### *2.2.4 D89N and Ester Double Mutants*

Backbone ester mutations in loop B were also produced in an attempt to recover wild-type receptor function from the D89N mutant. If indeed a $N^{\delta-}$–$H^{\delta+}$•••$H^{\delta+}$–$N^{\delta-}$ dipole-dipole clash is introduced by the D89N mutation, an appropriate backbone ester would not only alleviate the clash, but would replace it with a potentially favorable

hydrogen bond (Figure 2.3d). Two double mutants were evaluated, D89N/T150Tah and D89N/W149Wah (Table 2.3). The D89N/T150Tah double mutant (attempting to rescue hydrogen bond *i*) did not fully recover wild-type receptor function: 18- and 5-fold increases in $EC_{50}$ were observed for ACh and epibatidine, respectively. In contrast, the D89N/W149Wah double mutant (attempting to rescue hydrogen bond *ii*; Figure 2.3d) produced near wild-type activity, with $EC_{50}$ increases of only 2.7- and 1.3-fold for ACh and epibatidine, respectively. These results suggest that there is an asymmetry in the D89/loop B network that allows the electrostatic clash of the Asn side chain to be relieved through an ester at position 149 but not at position 150. Note that the D89N/W149Wah mutant receptor is an example of a receptor that contains no negative charge in the vicinity of position 89, but retains nearly wild-type activity.

### *2.2.5 Molecular Dynamics Simulation of nAChR Ligand-binding Domain*

We performed two simulations of the mouse muscle nAChR ligand-binding domain, one without and one with the agonist carbamylcholine (CCh) bound. Other simulations of AChBP and variants of the nAChR have appeared[19–24]. The agonist-free structure is based on Unwin's model of the receptor from *T. marmorata*, which is nearly identical in sequence to the mouse muscle receptor. CCh was then docked into this structure in a manner compatible with the crystal structure of AChBP that contains CCh in the agonist binding site[6]. We monitored hydrogen bonds *i* through *iv*, considering both oxygens of the D89 carboxylate (called OD1 and OD2; Figure 2.9), for a total of eight possible interactions. Along with the D89/loop B hydrogen bonds, we monitored two

"control" hydrogen bonds that are part of a well-defined α-helix in the ligand binding domain. The results summarized in Figure 2.8 and Table 2.4 are calculated from the final 500 ps of the 5 ns simulations.

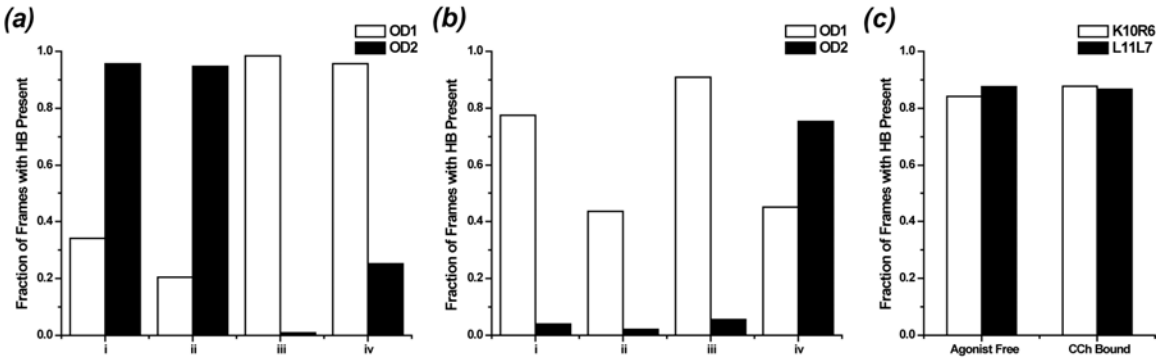


**Figure 2.8.** Analysis of hydrogen bonding in the molecular dynamics simulations of the nAChR ligand-binding domain without ***(a)*** and with ***(b)*** CCh bound. Hydrogen bonds were monitored between both D89 carboxylate oxygens (OD1, white bars, and OD2, black bars) and the four loop B hydrogen bond donors. ***(c)*** Control hydrogen bonds between the backbone amide of K10 and the backbone carbonyl of R6 (K10R6, white bar) and the backbone amide of L11 and the backbone carbonyl of L7 (L11L7, black bar) were also monitored in both structures. All observations were made during the last 500 ps of the 5 ns simulations. Data expressed as the fraction of the 1000 observed frames where a given hydrogen bond was present

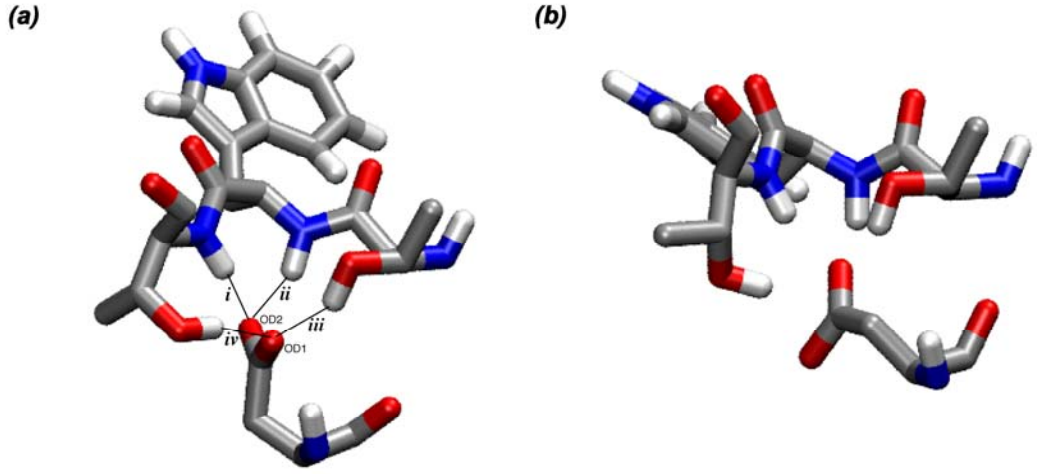


**Figure 2.9.** Two views of hydrogen bonding interactions for the receptor. Structure without ***(a)*** and with ***(b)*** CCh bound shown. Generated with the g_cluster program of the GROMACS suite from the final 500 ps of the 5 ns nAChR ligand-binding domain simulations

**Table 2.4.** Molecular Dynamics Simulations[a]

| | D89-Loop B Distance (Å)[b] | Number of D89-LoopB Hydrogen Bonds[c] | rmsd[d] |
|---|---|---|---|
| **WT Agonist Free** | 4.3 ± 0.2 | 4.7 ± 0.8 | -- |
| **WT CCh Bound** | 5.2 ± 0.3 | 3.4 ± 0.8 | 1.5 ± 0.2 |
| **D89N1** | 5.3 ± 0.3 | 1.6 ± 0.6 | 2.5 ± 0.1 |
| **D89N2** | 8.1 ± 0.5 | 1.5 ± 0.9 | 3.8 ± 0.3 |

[a]All statistics averaged over the last 500 ps of the given simulation (1000 frames) and presented as mean ± standard deviation of the mean. [b]Distance measured from D89 or N89 γ carbon to the W149 α carbon. [c]All hydrogen bonds between position 89 and loop B residues, T148, W149, and T150. Includes both oxygens of D89 in wild-type simulations. [d]rmsd calculated in reference to the average structure from the last 500 ps of the agonist free wild-type simulation. Average structure from g_cluster program of GROMACS suite

The agonist-free structure shows a very well-defined hydrogen bonding network. In a representative structure (Figure 2.9a), one carboxylate oxygen (OD2) makes hydrogen bonds to the two backbone NH groups (*i* and *ii*), while the other carboxylate oxygen makes hydrogen bonds to the two side chain OH groups (*iii* and *iv*). These are strong hydrogen bonds, being present more frequently than the reference hydrogen bonds of the α helix. Occasionally, one carboxylate oxygen simultaneously makes three hydrogen bonds; on average, there are 4.7 hydrogen bonds between D89 and loop B. Note that the orientation of the carboxylate in this simulation (Figure 2.2 and 2.9a) differs from previous models, the side chain having rotated to enable formation of four hydrogen bonds.

Addition of the agonist CCh leads to a weakened interaction between D89 and loop B. In the agonist-free simulation, D89 interacts with all four loop B hydrogen bond donors in 94% of the frames, but that number drops to 34% of the frames in the CCh-bound simulation. Hydrogen bonds to the loop B backbone, interactions *i* and *ii*, are

present less frequently in the CCh-bound structure (decreases of 17% and 50%, respectively, in the number of frames with a hydrogen bond present), while the side chain interactions, hydrogen bonds *iii* and *iv*, remain. The average number of hydrogen bonds drops from 4.7 to 3.4 when agonist binds, and the distance between D89 and W149 increases from 4.3 Å to 5.1 Å (measured from the D89 γ carbon to the W149 α carbon; Table 2.4). We also observed a similar decrease in hydrogen bonding between D89 and loop B when analyzing the last 500 ps of an α7 simulation[25] (3.97 ± 0.05 compared to 3.73 ± 0.05 hydrogen bonds for the agonist-free and CCh-bound structures, respectively). In the CCh-bound structure, OD1 makes the majority of the interactions with loop B, while OD2 only interacts with the T150 hydroxyl side chain (Figure 2.9b). Structurally, the changes between empty and occupied agonist binding sites arise because the D89 side chain rotates to a less symmetrical arrangement that favors one carboxylate oxygen over the other in hydrogen bonding (Figure 2.9). Also, the T150 side chain reorients, but the OH group ends up in a similar location. In addition, as others have noted, the side chain of W149 reorients to make a cation-π interaction with the agonist.

Simulations of the D89N mutant were performed on the agonist-free structure only, because the Asn mutant mainly affected the kinetics of association of the agonist with the unbound nAChR[11]. Two simulations that differ in the initial orientation of the Asn side chain were considered. In the D89N1 simulation, the N89 amide nitrogen was placed in a position comparable to that of OD1 of the agonist-free wild type structure, while in D89N2, the nitrogen was placed in the OD2 position.

As summarized in Table 2.4, both simulations show that the D89N mutant substantially disrupts the interaction between position 89 and loop B. The average

distance between N89 and loop B (measured from the N89 γ carbon to the W149 α carbon) over the final 500 ps was larger for both D89N1 and D89N2 simulations (5.3 Å and 8.1 Å, respectively) than either wild-type simulation. Also, in the D89N mutant simulations the 4.7 hydrogen bonds seen in the agonist free wild-type simulation are reduced to ~ 1.5, and many of these hydrogen bonds do not correspond to hydrogen bonds *i*–*iv*, but are new hydrogen bonds involving the backbone of N89. The substantial disruption of the D89N mutant structures was also observed in the loop B region. A comparison between the final loop B structure of the agonist-free wild-type simulation and comparable structures from the D89N1 and D89N2 simulations yielded rmsds of 2.5 Å and 3.8 Å, respectively (Table 2.4).

## 2.3 Discussion

### *2.3.1 AChBP and the D89/Loop B Network*

The study of the nAChR ligand-binding domain has been transformed by information gained from the AChBP crystal structures. Structural interactions found in the AChBP crystal structures have served as a starting point for new mutation studies in the nAChR and other Cys-loop family receptors[26,27]. However, since the AChBP is not an actual LGIC and is < 25% homologous to the closest nAChR relative, α7, experiments are necessary to test the relevance of interactions found in the crystal structures. The use of unnatural amino acids has allowed us to probe the relevance of these AChBP interactions at a chemical scale unavailable with conventional mutagenesis[10,12,13,28].

In this study, we have evaluated the structural role of the highly conserved residue, D89. According to the AChBP crystal structures, D89 provides the contact point between loop A, which contains D89 and agonist binding site residue Y93, and loop B, which contains the critical agonist binding site residue W149 (Figure 2.2). In the AChBP structures the D89 carboxylate forms hydrogen bonds with the backbone amides of loop B residues T150 and W149, while also interacting with the hydroxyl side chains of T148 and T150. This network is conserved among the primary ligand-binding subunits of the Cys-loop family of receptors (Figure 2.1). As noted before, D89 is part of a highly conserved WxPD motif found in essentially all known Cys-loop receptors. The residues aligning with T148 are conserved as hydroxyl side chains, serine, or threonine. W149 is part of the conserved aromatic box that comprises the agonist-binding site. In three different Cys-loop receptors—the nAChR considered here, the 5-$HT_3$ (serotonin) receptor, and the $GABA_C$ receptor—the aromatic residue that aligns with W149 makes direct contact with a bound agonist through a cation-π interaction [9,10–28,29].

### *2.3.2 D89/Loop B Unnatural Amino Acid Mutations*

The essential role of D89 was established by the severe consequences of the relatively modest mutation D89N, an effect reported previously[11]. Such a mutation could disrupt any or all of the four potential hydrogen bonds suggested by the AChBP structures (Figure 2.3). Conventional mutagenesis previously showed that hydrogen bonds *iii* and *iv* could be removed without significant disruption of receptor function. Using unnatural amino acid mutagenesis, we have now ablated hydrogen bonds *i*

(T150Tah) and *ii* (W149Wah), and neither change is seriously disruptive. Clearly, no single hydrogen bond between loop B and loop A is critical to receptor function.

Beyond disruption of the D89 / loop B hydrogen bond network, the D89N mutation neutralizes the negative charge of the wild-type Asp. Others have concluded that binding of cationic agonists such as ACh requires a negative charge in the loop A/loop B interface region. However, more subtle charge-neutralization strategies, such as incorporation of Nha or Akp, do not reproduce the full D89N effect. This suggests that another factor is operative.

We propose that the D89N mutation also introduces a destabilizing $N^{\delta-}$–$H^{\delta+}$•••$H^{\delta+}$–$N^{\delta-}$ dipole-dipole clash between position 89 and loop B. The other charge-neutralizing mutations, D89Nha and D89Akp, do not experience such a clash and so are less disruptive. Also, the introduction into the D89N mutant receptor of a second, backbone mutation that removes one of the offending $N^{\delta-}$–$H^{\delta+}$ dipoles (D89N/W149Wah) restores near wild-type behavior. This double mutant has no negative charge at the loop A / loop B interface yet is near wild type in behavior.

Nicotine data for the D89 mutations diverges from that of ACh and epibatidine, which are quite similar to each other. While the D89E and D89Akp mutants produce modest shifts in the ACh and epibatidine $EC_{50}$s, nicotine potency is barely affected. In contrast, the wild type to D89N and D89E to D89Nha nicotine $EC_{50}$ shifts are similar to those for ACh and epibatidine (Figure 2.10).

The most glaring difference in the nicotine data is found when comparing the D89N and D89Akp $EC_{50}$ shifts for each agonist (Electrostatic Clash in Figure 2.10).

There is a 14.5-fold improvement in nicotine potency when the Asn amide $NH_2$ group is substituted with the $CH_3$ group of Akp; ACh and epibatidine only experience a ~ 2.5-fold improvement. Relieving the electrostatic clash between Asn and loop B returns nicotine potency almost to that of wild type. Because ACh and epibatidine $EC_{50}$ values are still quite shifted, we concluded that the Akp mutation still disrupts the loop B structure possibly through general steric perturbations or destruction of the symmetry of the D89 / loop B interactions. Because nicotine only makes one contact with loop B, a hydrogen bond to the W149 carbonyl[10], the loop B binding requirements for nicotine are fewer than for the stronger agonists, ACh and epibatidine. These observations suggest that ACh and epibatidine are more sensitive to perturbations in loop B structure than nicotine.

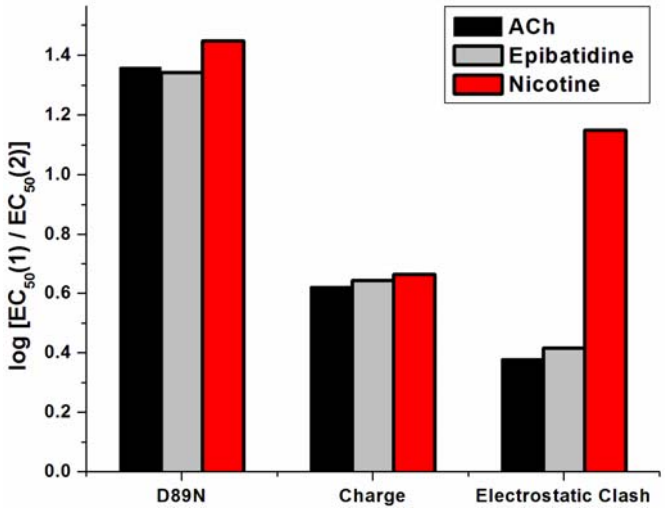


**Figure 2.10.** D89 unnatural mutation data compared between ACh, epibatidine, and nicotine. Three different $EC_{50}$ comparisons are made for each agonist and plotted as the log of the ratio of the two $EC_{50}$s (log [$EC_{50}$(1) / $EC_{50}$(2)]). D89N: $EC_{50}$(1) is D89N and $EC_{50}$(2) is wild type; Charge: $EC_{50}$(1) is D89Nha and $EC_{50}$(2) is D89E; Electrostatic Clash: $EC_{50}$(1) is D89N and $EC_{50}$(2) is D89Akp.

### *2.3.3 D89N Mutation and Implications for the Role of D89 in Ligand Binding*

Another proposed role for D89 is a polarization of the W149 carbonyl (*star* in Figure 2.2), which points into the agonist binding site and can directly contact agonists[6]. An amide carbonyl is highly polarized $C^{\delta+}=O^{\delta-}$, and the partial negative charge on oxygen could contribute to binding of cationic agonists. It has been proposed that the negative charge of D89 could enhance this polarization[6], although we are unaware of any precedent for this type of effect. Our results do not appear to support this suggestion. For the mutant T150Tah, the key carbonyl is much less polarized, as it is now an ester carbonyl rather than an amide carbonyl. However, this mutation decreases ACh $EC_{50}$, the opposite of expectations from the polarization suggestion.

The picture that emerges for the role of D89 is not simple. It seems certain that hydrogen bonding between the side chain of D89 and loop A is involved. However, no one interaction is singularly important. A subset of the full complement of interactions between D89 and loop B is required to stabilize the nAChR ligand-binding site.

Another possible indication of the disruptive nature of the D89N mutation can be found from a pair of Cys-loop receptors that are gated by serotonin. The 5-$HT_3$ receptor has a Trp that aligns with the nAChR Trp $\alpha$149, and it makes a cation-$\pi$ interaction with the agonist serotonin.[28] Interestingly, the MOD-1 receptor from *C. elegans* naturally contains the D89N modification, a rare exception to the highly conserved WxPD motif. Also, even though MOD-1 is highly homologous to the 5-$HT_3$ receptor, and binds the same neurotransmitter, the cation-$\pi$ interaction in MOD-1 has moved away from the loop

B aromatic residue to a different residue in the aromatic box on loop C. [30] This could reflect the disruption of loop B caused by the D89N substitution in MOD-1.

Molecular dynamics simulations generally support the experimental data of others and ourselves. In our simulations, a sharp reduction in the level of hydrogen bonding in the position 89/loop B network suggests that the D89N mutation severely disrupts interactions between position 89 and loop B. In fact, in one of the D89N simulations, the Asn side chain ceases to interact at all with loop B. Both D89N mutant simulations produced loop B structures that differed from their wild type counterparts. From these observations we conclude that loop B adjusts in structure to accommodate the Asn.

From our molecular dynamics simulations of the mouse muscle nAChR ligand-binding domain, it appears that D89 interacts with loop B more in the agonist-free state than in the agonist-bound state. Relative to the agonist-free structure we find an average of approximately one fewer hydrogen bond between D89 and loop B; and D89 is almost 1 Å further from loop B in the CCh-bound structure. Because loop B itself does not relocate substantially on agonist binding (as revealed in the comparison of our agonist-free and CCh bound wild-type simulations), the role of D89 is to preorganize the empty agonist binding site into a conformation that favors binding, an effect that would enhance binding affinity[31]. Apparently, once the agonist is bound, the stabilization of loop B provided by D89 is no longer necessary, and the interaction between the two is weakened. This is consistent with an earlier conclusion that the D89N mutation affects agonist association but not subsequent steps in the channel activation mechanism[11].

In conclusion, chemical-scale studies of the D89/loop B network have further refined our understanding of this interesting and highly conserved structural feature. D89 and loop B form a redundant network of hydrogen bonding interactions, no one of which is essential. In addition, the charge on D89 is not essential for receptor function. The D89N mutation both disrupts the hydrogen bonding network and introduces a repulsive electrostatic interaction, significantly destabilizing the D89/loop B network. These results, along with molecular dynamics simulations and earlier single-channel studies[11], indicate that the role of the D89/loop B network is to preorganize the agonist binding site for ligand binding, with no significant contribution to the gating mechanism.

## 2.4 Materials and Methods

### *Unnatural Amino Acid Suppression*

Synthetic amino acids and α-hydroxy acids were conjugated to the dinucleotide dCA and ligated to truncated 74 nt tRNA as previously described[32,33]. Aminoacyl tRNA was deprotected by photolysis immediately prior to co-injection with mRNA, as described previously[32,34]. Typically, 25 ng of tRNA was injected per oocyte along with mRNA in a total volume of 50 nL/cell. mRNA was prepared by *in vitro* runoff transcription using the Ambion (Austin, TX) T7 mMessage mMachine kit. The site of interest was mutated to the amber stop codon by standard means, verified by sequencing through both strands. Mouse muscle embryonic nAChR in the pAMV vector was used. A total of 4.0 ng of mRNA was injected in an α:β:γ:δ subunit ratio of 10:1:1:1. In all cases, a Leu-to-Ser mutation at a site 50 Å from the nAChR ligand-binding domain in the

M2 helix, known as 9', was used to lower $EC_{50}$ values to a measurable range[10,28]. Previous work on this mutation has shown that a Leu9'Ser mutation in the β subunit lowers $EC_{50}$ values 40-fold without changing trends in $EC_{50}$ values[13,28]. In addition, the α subunits contain an HA epitope in the M3-M4 cytoplasmic loop for Western blot studies. Control experiments show that this epitope does not detectably alter $EC_{50}$. As a negative control for suppression, truncated 74 nt tRNA or truncated tRNA ligated to dCA was co-injected with mRNA in the same manner as fully charged tRNA. At the positions studied here, no current was ever observed from these negative controls. The positive control for suppression involved wild-type recovery by co-injection with 74 nt tRNA ligated to dCA-Thr or dCA-Trp. Frameshift suppression at αD89 was utilized as described by Rodriguez *et al*[35].

### *Electrophysiology*

Stage V-VI oocytes of *Xenopus laevis* were employed. Oocyte recordings were made 24 to 48 h postinjection in two-electrode voltage clamp mode using the OpusXpress™ 6000A (Axon Instruments, Union City, CA). Oocytes were superfused with $Ca^{2+}$-free ND96 solution at flow rates of 1 mL/min before application, 4 mL/min during drug application, and 3 mL/min during wash. Holding potentials were -60 mV. Data were sampled at 125 Hz and filtered at 50 Hz. Drug applications were 15 s in duration. Acetylcholine chloride was purchased from Sigma/Aldrich/RBI. Epibatidine was purchased from Tocris as (±) epibatidine dihydrochloride. All drugs were prepared in sterile ddi water for dilution into calcium-free ND96. Dose-response data were

obtained for a minimum of 10 concentrations of agonists and for a minimum of three cells. Dose-response relations were fitted to the Hill equation to determine $EC_{50}$ and Hill coefficient values.

### *Generation of Mouse Muscle nAChR Heteropentamer Computational Model*

A model of the mouse muscle ligand-binding domain was created by first aligning the mouse muscle nAChR sequence with the sequence of the *Torpedo marmorata* acetylcholine receptor, the structure of which had been determined using electron microscopy by Unwin[36] and resolved to 4 Å resolution[37]. An alignment was generated using the T-Coffee website. A homology model was then built with this alignment using Prime[38], within the Schrödinger suite of programs. The individual chains of *Torpedo* structure 2BG9 were used as templates for each subunit type. Chain A of the Torpedo structure was used as a template for both α subunits of the mouse muscle nAChR. Each subunit was exported as a PDB file and aligned in Swiss PDB Viewer[39]. This structure was imported back to Prime where a side-chain prediction algorithm was used.

This heteropentamer was converted to GROMACS[40] format and inserted into a periodic box with 7 Å gaps between the protein and the box edge for molecular mechanics minimizations and simulations. SPC water molecules[40] were used to add explicit solvation to the model followed by the insertion of sodium and chloride ions to bring the molarity of the box to 150 mM. An excess of sodium ions was added to neutralize the charge of the protein.

*Ligand Incorporation into Mouse Muscle nAChR Model*

Using this heteropentamer, another structure was generated containing carbamoylcholine (CCh) in the ligand-binding pocket. CCh was inserted into the two binding pockets of the mouse muscle nAChR. This was performed by aligning the box residues of the mouse muscle model with the D binding site of the AChBP structure containing CCh (1UV6). Gromacs parameters for the ligand (CCh) were initially generated using ProDRG (http://davapc1.bioch.dundee.ac.uk/programs/prodrg/)[41]. The charges generated by ProDRG for CCh were modified due to a large positive charge that was inaccurately placed on the nitrogen atom of the ammonium. Instead, ChelpG charges from HF/6-31G** calculations were used with some attenuation of the partial charges between carbamoyl protons and oxygens to fit within GROMACS MD parameters.

*Generation of the D89N Mutant Structures*

D89N mutant structures were made from the homology model PDB file by mutating D89 of both α subunits to Asn using Swiss PDB. The two structures differed in their orientations of the $NH_2$ group of the side chain: D89N1 placed the $NH_2$ group in a position analogous to that of OD1 of D89 in the wild-type model, while D89N2 placed the NH2 group in a position analogous to that of OD2. The mutant models were then placed in a hexagonal periodic box and treated like the wild-type model.

### *Molecular Dynamics Simulations*

All four nAChR structures (agonist free wild type, CCh bound wild type, D89N1, and D89N2) underwent one minimization step. Then, under the GROMACS force field, MD simulations were begun. The MD simulations started at 0 K and warmed to 310 K over the first 25 ps. The protein and drug (CCh bound structure) were highly restrained during this warmup, followed by 100 ps of slowly releasing the restraints. All simulations after this point continued unrestrained for 5000 ps (wild type-structures) or 7500 ps (D89N mutant structures). α7 model and molecular dynamics simulations were performed by E. James Petersson[25].

### *Analysis of Molecular Dynamics Simulations*

All molecular dynamics trajectories were analyzed using the tools included in the GROMACS suite(*26*). All characterizations were performed on the last 500 ps of the simulations. Each trajectory file contained data for every 0.5 ps, yielding 1000 frames of analysis per simulation.

Distances and hydrogen bonds were analyzed using the g_dist and g_hbond programs, respectively. The default g_hond hydrogen bond structural cut-offs (a donor/acceptor distance of 3.5 Å and an acceptor-hydrogen-donor angle of 30°) were used when monitoring hydrogen bonds.

rmsd values for the CCh bound wild type, D89N1, and D89N2 simulations were calculated using the g_rms program. All comparisons were made with respect to the

average loop B structure of the last 500 ps of the agonist-free wild-type simulation obtained from g_cluster, using the gromos method and an rmsd cutoff of 0.14 Å. The α carbons of the two structures to be compared were aligned prior to the rmsd calculation. Figure 2.9 was produced from PDB files generated by g_cluster, using the conditions described above on the agonist free and CCh bound wild-type simulation trajectories.

### *Synthesis of Wah cyanomethyl ester and* dCA-Wah

Syntheses for both molecules performed by Amanda L. Cashin[18].

### *Synthesis of t-Butyl 2-Diphenylmethyleneimino-4-nitro-butanoate, nitrohomoalanine, NVOC-nitrohomoalanine, NVOC-nitrohomoalanine cyanomethyl ester, and Nha-dCA*

Described in Appendix A.

### *Synthesis of Akp-dCA*

The synthesis of 2-amino-4-ketopentanoic acid and preparation of Akp-dCA were described previously[42].

## 2.5 References


(1) Miyazawa, A.; Fujiyoshi, Y.; Stowell, M.; Unwin, N. *Journal of Molecular Biology* **1999**, *288*, 765–786.

(2) Corringer, P.J.; Novere, N. L.; Changeux, J.-P. *Annual Review of Pharmacology and Toxicology* **2000**, *40*, 431–458.

(3) Grutter, T.; Changeux, J.P. *Trends in Biochemical Sciences* **2001**, *26*, 459–463.

(4) Karlin, A. *Nature Reviews Neuroscience* **2002**, *3*, 102–114.

(5) Brejc, K.; van Dijk, W. J.; Klaassen, R. V.; Schuurmans, M.; van der Oost, J.; Smit, A. B.; Sixma, T. K. *Nature* **2001**, *411*, 269–276.

(6) Celie, P. H. N.; van Rossum-Fikkert, S. E.; van Dijk, W. J.; Brejc, K.; Smit, A. B.; Sixma, T. K. *Neuron* **2004**, *41*, 907–914.

(7) Hansen, S. B., Sulzenbacher, G., Huxford, T., Marchot, P., Taylor, P., Bourne, Y. *EMBO Journal* **2005**, *24*, 3625–3646.

(8) Smit, A. B.; Syed, N. I.; Schaap, D.; van Minnen, J.; Klumperman, J.; Kits, K. S.; Lodder, H.; van der Schors, R. C.; van Elk, R.; Sorgedrager, B.; Brejc, K.; Sixma, T. K.; Geraerts, W. P. M. *Nature* **2001**, *411*, 261–268.

(9) Zhong, W.; Gallivan, J. P.; Zhang, Y.; Li, L.; Lester, H. A.; Dougherty, D. A. *PNAS* **1998**, *95*, 12088–12093.

(10) Cashin, A. L.; Petersson, E. J.; Lester, H. A.; Dougherty, D. A. *J. Am. Chem. Soc.* **2005**, *127*, 350–356.

(11) Lee, W. Y.; Sine, S. M. *J. Gen. Physiol.* **2004**, *124*, 555–567.

(12) Dougherty, D. A. *Current Opinion in Chemical Biology* **2000**, *4*, 645–652.

(13) Kearney, P. C.; Nowak, M. W.; Zhong, W.; Silverman, S. K.; Lester, H. A.; Dougherty, D. A. *Mol Pharmacol* **1996**, *50*, 1401–1412.

(14) Nowak, M. W.; Gallivan, J. P.; Silverman, S. K.; Labarca, C. G.; Dougherty, D. A.; Lester, H. A.; Conn, P. M. *Methods in Enzymology* **1998**, *293*, 504–529.

(15) Rodriguez, E. A.; Lester, H. A.; Dougherty, D. A. *Proc. Natl. Acad. Sci.* **2006**, *103*, 8650–8655.

(16) Kelly, T. R.; Kim, M.H. *Journal of the American Chemical Society* **1994**, *116*, 7072–7080.

(17) Thorson, J. S.; Chapman, E.; Schultz, P.G. *Journal of the American Chemical Society* **1995**, *117*, 9361–9362.

(18) Cashin, A. L. California Institute of Technology, 2006.

(19) Gao, F.; Bern, N.; Little, A.; Wang, H.L.; Hansen, S. B.; Talley, T. T.; Taylor, P.; Sine, S. M. *J. Biol. Chem.* **2003**, *278*, 23020–23026.

(20) Gao, F.; Bren, N.; Burghardt, T. P.; Hansen, S.; Henchman, R. H.; Taylor, P.; McCammon, J. A.; Sine, S. M. *J. Biol. Chem.* **2005**, *280*, 8443–8451.

(21) Henchman, R. H.; Wang, H.L.; Sine, S. M.; Taylor, P.; McCammon, J. A. *Biophys. J.* **2003**, *85*, 3007–3018.

(22) Henchman, R. H.; Wang, H.L.; Sine, S. M.; Taylor, P.; McCammon, J. A. *Biophys. J.* **2005**, *88*, 2564–2576.

(23) Le Novere, N.; Grutter, T.; Changeux, J.P. *PNAS* **2002**, *99*, 3210–3215.

(24) Schapira, M.; Abagyan, R.; Totrov, M. *BMC Structural Biology* **2002**, *2*, 1.

(25) Petersson, E. J. California Institute of Technology, 2005.

(26) Criado, M.; Mulet, J.; Bernal, J. A.; Gerber, S.; Sala, S.; Sala, F. *Mol Pharmacol* **2005**, *68*, 1669–1677.
(27) Mukhtasimova, N.; Free, C.; Sine, S. M. *J. Gen. Physiol.* **2005**, *126*, 23–39.
(28) Beene, D. L.; Brandt, G. S.; Zhong, W.; Zacharias, N. M.; Lester, H. A.; Dougherty, D. A. *Biochemistry* **2002**, *41*, 10262–10269.
(29) Lummis, S. C. R.; L. Beene, D.; Harrison, N. J.; Lester, H. A.; Dougherty, D. A. *Chemistry & Biology* **2005**, *12*, 993–997.
(30) Mu, T. W.; Lester, H. A.; Dougherty, D. A. *J. Am. Chem. Soc.* **2003**, *125*, 6850–6851.
(31) Cram, D. J. *Angewandte Chemie—International Edition in English* **1986**, *25*, 1039–1057.
(32) Nowak, M. W.; Gallivan, J. P.; Silverman, S. K.; Labarca, C. G.; Dougherty, D. A.; Lester, H. A. *Ion Channels, Pt B* **1998**, *293*, 504–529.
(33) England, P. M.; Lester, H. A.; Dougherty, D. A. *Tetrahedron Letters* **1999**, *40*, 6189–6192.
(34) Li, L. T.; Zhong, W. G.; Zacharias, N.; Gibbs, C.; Lester, H. A.; Dougherty, D. A. *Chemistry & Biology* **2001**, *8*, 47–58.
(35) Rodriguez, E. A.; Lester, H. A.; Dougherty, D. A. *PNAS* **2006**, *103*, 8650–8655.
(36) Miyazawa, A.; Fujiyoshi, Y.; Unwin, N. *Nature* **2003**, *423*, 949–55.
(37) Unwin, N. *J Mol Biol* **2005**, *346*, 967–89.
(38) Schrodinger, I. Portland, OR.
(39) Guex, N.; Peitsch, M. C. *Electrophoresis* **1997**, *18*, 2714–2723.
(40) van der Spoel, D., Lindahl, E., Hess, B., van Buuren, A.R., Apol, E., Meulenhoff, P. J., Tieleman, D.P., Sijbers, A.L.T.M., Feenstra, K.A., R., v.D., Berendsen, H.J.C. 2004.
(41) Schuettelkopf, A. W.; van Aalten, D.M.F. *Acta Crystal* **2004**, *D60*, 1355–1363.
(42) Mu, T. California Institute of Technology, 2006.

# **Chapter 3:** Incorporation of Unnatural Amino Acids into the Binding Site of the $M_2$ Muscarinic Acetylcholine Receptor

## 3.1 Introduction

### *3.1.1 The G-Protein Coupled Receptor Superfamily*

More drugs target the G-protein coupled receptor (GPCR) superfamily of proteins than any other protein family[1]. In 2001, 30% of all drugs on the market—and 25% of the top 100 selling drugs—hit GPCRs. Annually, sales for drugs that modulate GPCRs exceed $30 billion[2]. These statistics reflect the diversity of GPCR biology in the cell and the myriad natural ligands that affect GPCRs. Extracellular stimuli as diverse as photons, neurotransmitters, peptides, lipids, and proteases activate GPCR signaling networks involved in processes such as memory, drug addiction, social behavior, three of the five senses (vision, olfaction, and taste), and the regulation of cardiac and pulmonary function[2–4].

As a superfamily, all GPCRs share a topology consisting of seven transmembrane helices (Figure 3.1). The classical model of a GPCR signaling network begins with an extracellular stimulus, such as ligand binding, acting on the resting receptor (Figure 3.1a). A conformational change in the transmembrane helices produces an active conformation, which reorganizes the intracellular face of the GPCR[5]. Heterotrimeric G-proteins—consisting of $\alpha$, $\beta, \gamma$ subunits—bind to the intracellular face of the receptor, which facilitates the exchange of GDP for GTP in the G$\alpha$ subunit (Figure 3.1b). Upon GTP

binding, the Gα and Gβγ subunits dissociate and affect various downstream cellular targets (Figure 3.1c). Depending on the Gα subfamily, the G-proteins act on different effectors: $G_i$ activates adenyl cyclase (AC), $G_q$ affects phospholipase C (PLCβ), $G_{12/13}$ mediates Rho GTPase activity, and $G_{i/o}$ gates G-protein activated inward rectifying potassium channels (GIRKs) and inhibits AC[6]. G-protein signaling is terminated through the hydrolysis of GTP by the Gα GTPase domain and reassociation of the Gα and Gβγ subunits (Figure 3.1d).

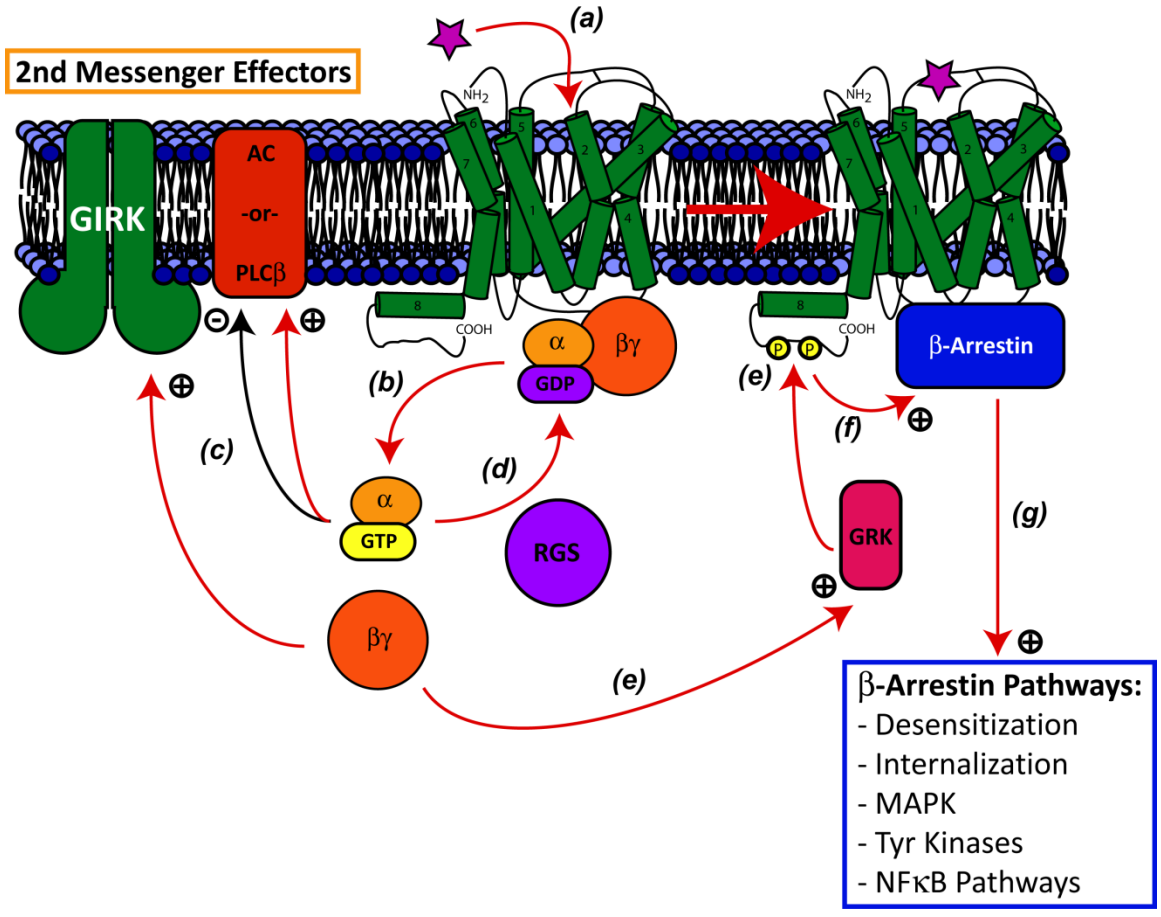


**Figure 3.1.** GPCR signaling and desensitization pathways

Desensitization of a GPCR signal is a multi-step process that terminates G-protein binding to the receptor[4,7]. In the first step of desensitization, Ser and Thr residues within

the C-terminus of active GPCRs are phosphorylated by GPCR receptor kinases (GRKs). GRKs are activated through interactions with Gβγ (Figure 3.1e). β-arrestin binds to phosphorylated receptor conformations and blocks further G-protein binding (Figure 3.1f). After β-arrestin mediated desensitization, β-arrestin can also interact with other cellular proteins to promote receptor internalization, degradation, and recycling (Figure 3.1g).

GPCR studies in the last decade have revealed a more complex signaling system. The classical image of a GPCR signaling to a specific downstream effector has been modified to allow for GPCRs that can couple to multiple second-messenger pathways [8]. These GPCRs have receptor conformations that can bind multiple subtypes of Gα. Other downstream effectors, not associated with G-protein signaling, can also be modulated through interactions with β-arrestin (Figure 3.1g). Some heterotrimeric G-proteins do not dissociate upon GTP exchange and instead appear to undergo a structural rearrangement between the Gα and Gβγ subunits[9,10]. Receptors and G-proteins also have been found to pre-couple in a signaling complex prior to receptor activation[11–14].

The most significant amendment to the classical GPCR signaling model is the concept of GPCR dimerization[4,15,16]. Researchers who obtained AFM images of rhodopsin dimers have suggested that GPCR dimers are the functional unit of GPCR signaling. According to this model, the G-protein heterotrimer makes contact with both of the monomers, but is only activated by one of the receptors in the dimer[17,18]. While the prevalence of non-rhodopsin GPCR dimers is debated[15], dimer formation has been shown to affect receptor signaling in several different systems. $GABA_B$ receptors must

heterodimerize to produce a competent signaling complex; expression of $GABA_{B1}$ or $GABA_{B2}$ alone does not yield a functional receptor. Heterodimers of opioid receptors are also proposed and believed to affect agonist affinity, pathway signaling, and receptor internalization[19].

GPCRs exhibit other complex pharmacology apart from the effects of dimerization. Different ligands at the same receptor can promote different GPCR-signaling profiles. This phenomenon is called ligand bias[20]. In the parathyroid hormone (PTH) receptor, some peptide agonists trigger $G_s$-coupled signaling, while other peptides activate both $G_q$ and $G_s$ pathways[20]. Some angiotensin II type 1 ($AT_1$) and PTH receptor agonists can induce conformations that recruit β-arrestin binding without G-protein activation[20,21]. Finally, there are GPCRs, like the μ-opioid receptor (MOR), that do not desensitize when activated by specific agonists. MOR bound with the natural agonist, enkephalin, desensitizes through the normal β-arrestin mechanism, while morphine bound to MOR does not trigger GRK phosphorylation or β-arrestin binding[22,23].

Inverse agonism is another pharmacological concept associated with GPCRs. An inverse agonist inhibits constitutive activity, which is described as the ability of a receptor to spontaneously adopt an active conformation and couple with G-proteins in the absence of ligand binding. Inverse agonists work by binding to the receptor and stabilizing the resting state of the receptor over the activated state. Because constitutively active mutants (CAMs) in GPCRs are implicated in diseases ranging from cancer to endocrine diseases, like male precocious puberty[24], inverse agonists are an important pharmaceutical target.

### *3.1.2 The Aminergic Class of GPCRs and Muscarinic Acetylcholine Receptors*

Monoamine neurotransmitters, such as dopamine, serotonin, epinephrine, and acetylcholine, can signal through the aminergic class of GPCRs. These receptors belong to the rhodopsin-like family of GPCRs (family A or I) and share many of the structural features found in the rhodopsin crystal structure[25–28]. The receptors have short N-terminal sequences and an eighth amphiphilic helix at the C-terminus that runs parallel to the intracellular side of the membrane bilayer. A conserved disulfide bond connects the first extracellular loop (EL-1), which bridges transmembrane helix 2 (TM2) and TM3, with the second extracellular loop (EL-2), which bridges TM4 and TM5. A recent crystal structure of the $\beta_2$ adrenergic receptor ($\beta_2$AR) confirms these conserved features[29–31].

Aminergic GPCRs lack large extracellular ligand binding domains, such as those found in metabotropic glutamate receptors (mGluRs). The monoamine ligands instead bind within a shallow crevice created between the seven transmembrane helices (Figure 3.2)[27,32]. There have been many attempts to model the binding sites of aminergic GPCRs[25,33–39], but the low sequence homology between receptors (rhodopsin and the muscarinc receptors only share 16% overall sequence identity and 21% identity within transmembrane regions[36]) has prevented the creation of successful models.

The centerpiece of the aminergic binding site is a highly conserved Asp on TM3, D3.32. (The X.50 numbering convention of Ballesteros[28] will be used throughout this chapter. This convention uses the one-letter amino acid code, the helix number, and a residue index number. To index each residue of a helix, the most conserved residue in

the helix is denoted as 50 and all other residues are numbered N-terminal to C-terminal accordingly. For example, D3.32 refers to an Asp residue on TM3, 18 residues in the N-terminal direction from the highly conserved Arg residue.) Surrounding the conserved D3.32, there is a cluster of aromatic residues reminiscent of the aromatic box found in the binding site of the Cys-loop family of LGICs. The recent $\beta_2$AR crystal structure shows the secondary amine of carazolol, an inverse agonist, in close proximity to D3.32 and several aromatic residues[31].

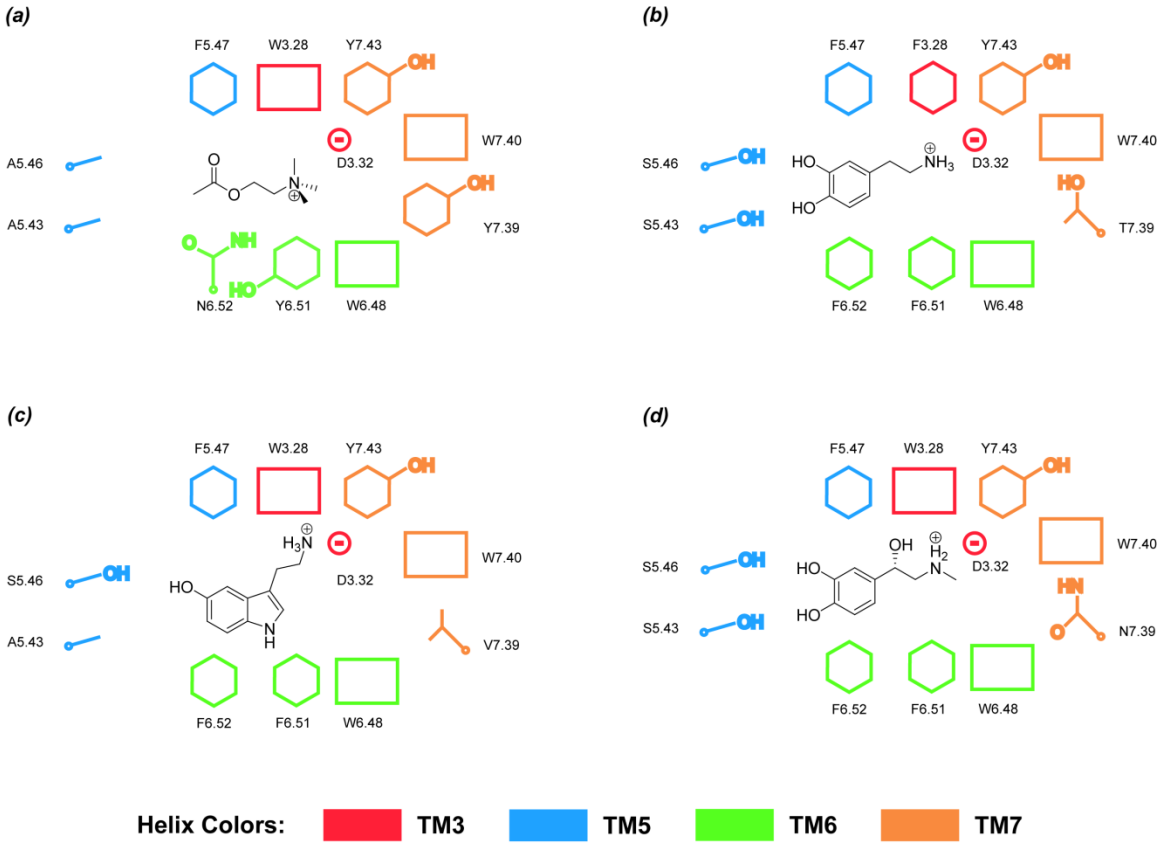


**Figure 3.2.** Schematic of aminergic GPCR binding sites. ***(a)*** $M_2$AChR binding site with ACh. ***(b)*** D2R binding site with dopamine. ***(c)*** 5-$HT_{2A}$ binding site with serotonin. ***(d)*** β2AR binding site with epinephrine

Residues that are believed to bind the non-amine end of ligands are also quite conserved. Ser residues on TM5 (S5.46 and S5.43) have been proposed to bind the hydroxyl groups of the catechol containing agonists (dopamine and epinephrine) in the

$D_2$ dopamine receptor ($D_2R$) and $\beta_2AR$, respectively. In the serotonin 2A receptor (5-$HT_{2A}R$), one of these Ser is an Ala and in the $M_2$ muscarinic acetylcholine receptor ($M_2AChR$) both are Ala, which reflects the fact that serotonin only has one hydroxyl group and ACh has none. Position 6.52 also seems to bind non-amine moieties of aminergic agonists. In receptors that have aromatic-based agonists, position 6.52 is conserved as a Phe. This position is an Asn in $M_2AChR$ and is proposed to make a hydrogen bond to the ester moiety of ACh.

There are five sub-types of muscarinic acetylcholine receptor, $M_1$ through $M_5$. As a group of GPCRs, the five sub-types of receptors are highly homologous; the group has a 63% sequence identity within the transmembrane region[36]. This high degree of similarity has made the discovery of subtype-specific ligands extremely difficult. As drug targets, the muscarinic receptors are investigated in connection with Alzheimer's disease[40], schizophrenia[41], and smooth muscle disorders, such as overactive bladder, irritable bowel syndrome, and chronic obstructive pulmonary disorder[42].

### *3.1.3 GIRK 1/4 Readout of $M_2AChR$*

As GPCRs do not produce an easily detectable signal on their own, researchers often use downstream effectors as a readout of GPCR function. In our GPCR experiments described below, we chose to measure $M_2AChR$ activity through GIRK signals. GIRK channels allowed us to utilize electrophysiology as an assay—a technique we have used with the unnatural amino acid methodology for the past decade in our studies of LGICs[23,43–60].

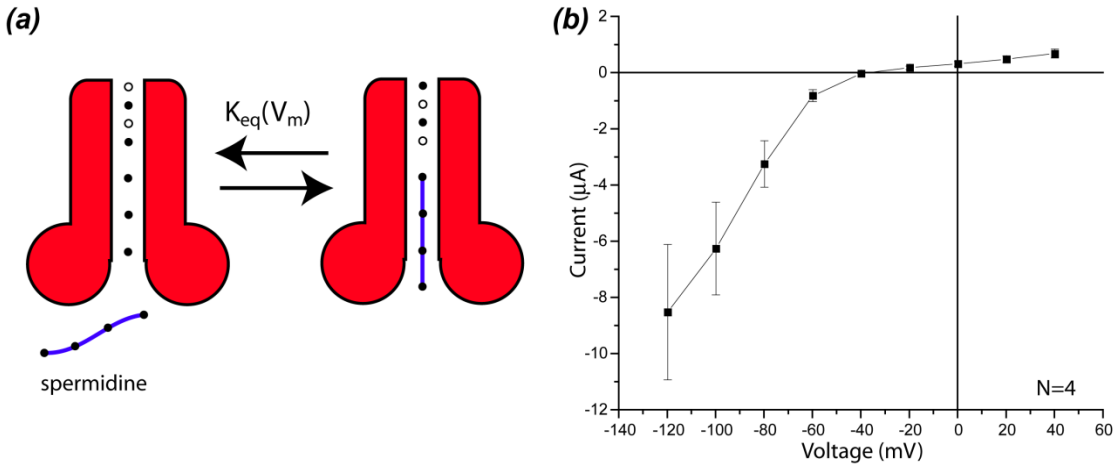


**Figure 3.3.** Inward rectification. ***(a)*** Schematic for inward rectification mechanism. ***(b)*** Sample IV curve data from GIRK 1/4 channels exhibiting inward rectification

Only $M_2$AChR and $M_4$AChR couple to GIRK channels through members of the $G_{i/o}$ family of G-proteins. The other three muscarinic receptors signal through the $G_q$ family and activate PLCβ. Unlike most other downstream effectors of GPCR signaling, GIRK channels are gated through the binding of free Gβγ subunits, not the GTP-bound Gα subunit[61–64]. Four Gβγ subunits are required to gate the channel, one per subunit of the tetrameric ion channel[65,66]. G-protein binding sites have been found on both the N- and C-terminal regions of the GIRK subunits[61,63].

GIRK channels exist as heterotetramers with a $X_2Y_2$ stoichiometry, where X and Y are two different GIRK subtypes. The two predominant heterotetramers are GIRK1/GIRK2 (GIRK 1/2) and GIRK1/GIRK4 (GIRK 1/4), which are found mainly in the brain and smooth muscle tissue, respectively. Otto Loewi's initial experiments on synaptic transmission showed that a substance released by the vagus nerve slowed the rate of cardiac action potentials. It was later found that this substance was ACh and its target of action was the $M_2$AChR-GIRK 1/4 signaling system[63,67,68].

As inward rectifying channels, GIRKs do not conduct currents in and out of the cell equally. At depolarized membrane potentials, the channels pass currents inwardly. But, when the cell is hyperpolarized, GIRKs conduct negligible outward currents. At these hyperpolarized membrane potentials, positively charged polyamines inside the cell, like spermidine, bind to the negatively charged intracellular domain of the GIRK and block the channel pore (Figure 3.3a). This intracellular blockage produces an IV relationship that turns over at membrane potentials close to 0 mV (Figure 3.3b)[63].

### *3.1.4 Goals of Project*

As illustrated in the above summary, GPCRs provide many opportunities to explore chemical-level phenomena. Our studies on LGICs have already proven the utility of unnatural amino acid incorporation in analyzing large, complex signaling proteins. We believe that from ligand binding and receptor activation to ligand bias and inverse agonism, the subtlety of unnatural amino acid mutagenesis could provide a new tool in elucidating the structure and function of this significant protein family.

To begin these studies and adapt the unnatural amino acid methodology to the GPCR system, we chose the $M_2$AChR—a receptor that binds the familiar agonist, ACh—as our initial target. Our first goal was to successfully incorporate unnatural amino acids into the $M_2$AChR and, using electrophysiological readout from GIRK 1/4 channels, to develop a procedure for assaying receptor function that is robust and reliable. Our second goal was to begin to probe important binding site residues and determine their role in ACh binding. In particular, we wanted to determine whether the quaternary amine

of ACh was bound through a cation-π interaction, as it is in the nicotinic acetylcholine receptor (nAChR)[69].

## 3.2 Results

### *3.2.1 Electrophysiology of the $M_2$AChR-GIRK 1/4 System*

Figure 3.4 illustrates the basic procedure we used in our $M_2$AChR-GIRK 1/4 assays. Because GIRKs only conduct inward currents, against the potassium concentration gradient, a ringer solution with a high potassium concentration must be used to produce significant current magnitudes. We chose to use a ringer solution that is the same as ND96, but has a potassium concentration of 24 mM (ND96 potassium concentration of 2 mM). This concentration of potassium generated currents of sufficient magnitude and was tolerated well by the cells.

To assay the response of the $M_2$AChR to a given dose of ACh, our experiments began by voltage clamping the cell at -60 mV. Higher currents can be produced if more negative holding potentials are used[70], but we found that these higher holding potentials lead to more extensive cell death through the course of an experiment. After an initial pre-wash of ND96 to determine a baseline current level (Figure 3.4a), we switched to the high-potassium ringer. Upon switching to the high-potassium ringer, a basal potassium current was generated due to the presence of free Gβγ inside the cell[66,71]. After 50 s, this standing current began to level off. A dose of ACh in the high-potassium ringer was then applied to the cell for 15 s. Drug was washed out of the chamber through a two-phase

wash protocol; the initial phase involved washing with the high-potassium ringer and the final phase consisted of a longer wash with ND96.

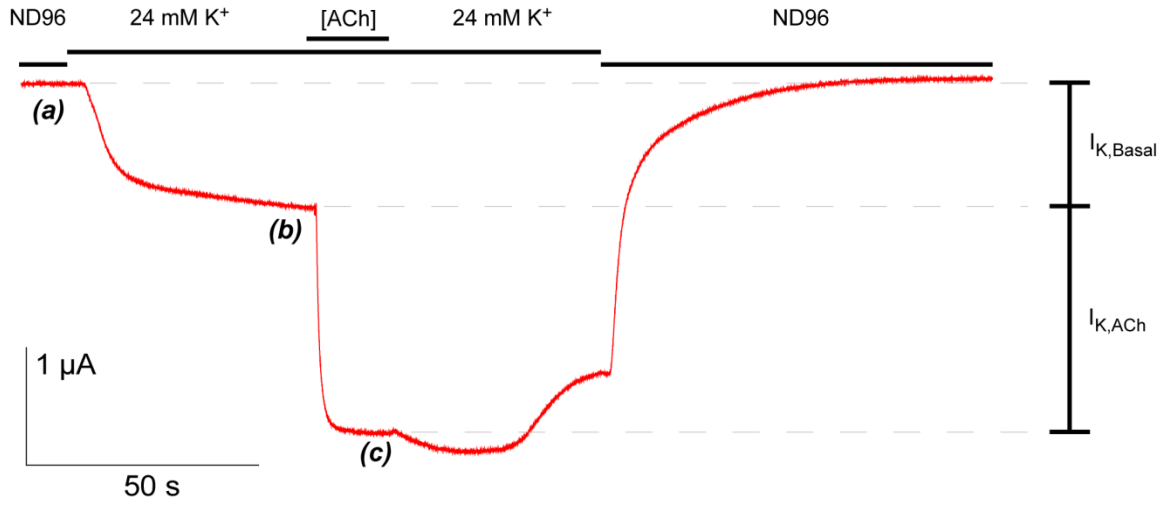


**Figure 3.4.** Example of a GPCR electrophysiology experiment. ND96 ringer solution has a potassium concentration of 2 mM. ACh is applied in the presence of the high-potassium ringer. $I_{K,\ Basal}$ is defined as the current difference between ***(b)*** and ***(a)***; subtraction of ***(b)*** from ***(c)*** yields $I_{K,\ ACh}$

For the rest of this chapter, we will refer to two current measurements frequently. $I_{K,Basal}$ refers to the basal potassium current produced by free Gβγ and is measured as the difference between the current level at the end of the high-potassium pre-wash (Figure 3.4b) and the initial baseline current in ND96 (Figure 3.4a). $I_{K,ACh}$ is defined as the ACh-induced current and is measured as the difference between the current at the end of the 15 s drug application (Figure 3.4c) and at the end of the high-potassium ringer pre-wash (Figure 3.4b).

The above experimental procedure was successful in producing robust $M_2$AChR-GIRK 1/4 signals, but the resulting data was highly variable. In the following sections, we will discuss the current and, especially, $EC_{50}$ data variability that we observed. We will also describe how this system was optimized to yield reproducible data.

### 3.2.2 Co-Injection of Gα mRNA Blocks $I_{K,Basal}$

Our first attempt to eliminate a possible source of variability in the GPCR assay was to control $I_{K,Basal}$. We believed that because we could not control the level of free Gβγ in the cell, basal current levels might fluctuate greatly and affect the reliability of our data. To control free Gβγ levels in the cell, we injected Gα mRNA with the mRNA for $M_2$AChR and GIRK 1/4. The extra Gα proteins in the cell would bind to any free Gβγ subunits. Previous experiments had shown that co-injecting Gα mRNA produced lower or negligible basal current levels[66,71].

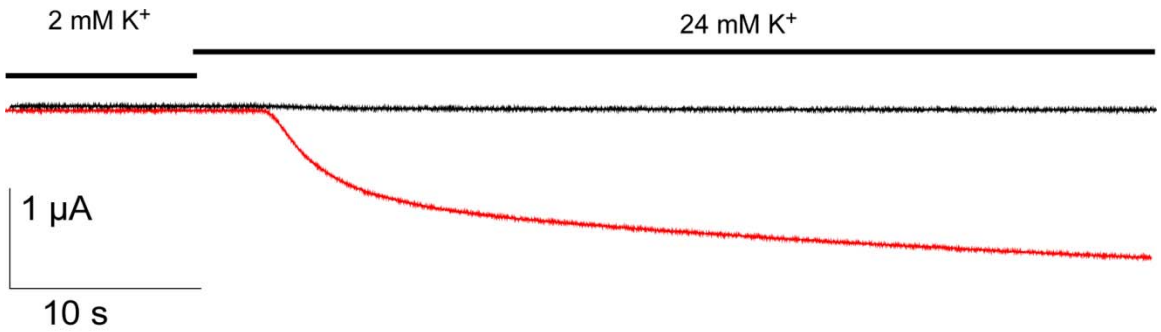


**Figure 3.5.** Example of $I_{K,\ Basal}$ suppression through injection of Gα mRNA. Black trace is $M_2$AChR / GIRK 1/4 system with 10 ng $G\alpha_{oA}$ mRNA, while red trace is the system without additional Gα mRNA.

We decided to use $G\alpha_{oA}$ mRNA because a previous study showed that co-injections with it not only produced the lowest $I_{K,Basal}$, but also exhibited higher $I_{K,ACh}$ when compared to injections of other $G_{i/o}$ mRNAs[66]. In our experiments, co-injection of 10 ng of $G\alpha_{oA}$ mRNA significantly decreased $I_{K,Basal}$ by 86% from 0.7 μA to 0.1 μA (Figures 3.5 and 3.6a). $I_{K,ACh}$ also increased by 65% from 2.0 μA to 3.3 μA (Figure 3.6a). Reducing the amount of $G\alpha_{oA}$ mRNA injected from 10 ng to 2 ng also produced a significant increase in $I_{K,ACh}$ (Figure 3.6b). We therefore decided to proceed by co-injecting 2 ng of $G\alpha_{oA}$ mRNA in subsequent experiments.

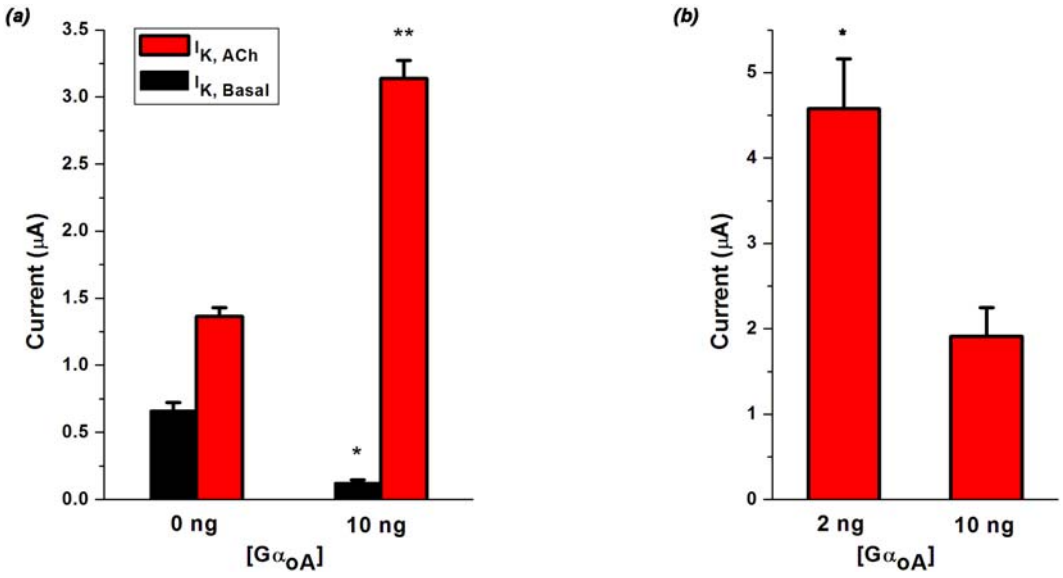


**Figure 3.6.** Experiments with $G\alpha_{oA}$ mRNA injections. ***(a)*** Co-injection of 10 ng of $G\alpha_{oA}$ mRNA decreases $I_{K, Basal}$ from 0.7 μA to 0.1 μA, while increasing $I_{K,ACh}$ from 2.0 μA to 3.3 μA. N = 6 and N = 7 for the 0 ng and 10 ng conditions, respectively. ***(b)*** Decreasing $G\alpha_{oA}$ mRNA from 10 ng to 2 ng, enhanced $I_{K, ACh}$ by 142% (1.9 μA to 4.6 μA). N = 20 and N= 9 for the 2 ng and 10 ng conditions, respectively. Error bars are SEM. * *t*-test $p = 0.01$; ** *t*-test $p = 0.001$

### *3.2.3 RGS4 and Current Trace Kinetics*

It has been known in the $M_2$AChR-GIRK 1/4 literature that $I_{K,ACh}$ trace kinetics do not resemble native kinetics in cardiac cells without the injection of an additional component[72]. This additional component is the regulator of G-protein signaling 4 (RGS4). Proteins belonging to the RGS family all act as G-protein-activating proteins (GAPs) by accelerating the kinetics of GTP hydrolysis in the Gα GTPase domain. RGS4 proteins bind Gα and stabilize the switch I and II regions of the GTPase domain, which contain the domain's catalytic residues.

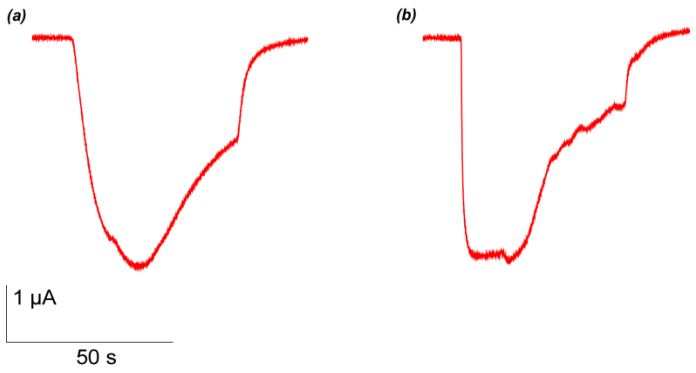


**Figure 3.7.** RGS kinetic effect. 0.5 ng $M_2$AChR / 10 ng GIRK 1/4 co-injected with 0 ng ***(a)*** and 10 ng RGS4 ***(b)***. RGS4 mRNA co-injection increases both activation and deactivation kinetics.

The electrophysiological consequence of adding RGS4 to the cell is faster deactivation kinetics in $I_{K,ACh}$ traces (Figure 3.7). Also, it has been observed that RGS4 co-injection increases activation kinetics (Figure 3.7). Researchers have proposed that RGS4 not only acts as a GAP, but also serves as scaffolding for a signaling complex between the GPCR, G-protein, and GIRK channel[65,66]. In this model, activation kinetics are thought to be increased through maintaining the signaling partners in close proximity.

For our experiments, we sought uniform traces that reached a maximum $I_{K,ACh}$ level quickly and, therefore, we experimented with RGS4 mRNA injections. We compared the effects of injecting 10 ng of RGS4 mRNA at two different times, 48 hrs and 24 hrs, prior to recording. Injection 24 hrs before recording yielded more uniform accelerated kinetics than 48 hr injection. Throughout the rest of this chapter, all experiments described will involve a 10 ng injection of RGS4 mRNA 24 hours prior to recording.

### *3.2.4 Dose-Response Relationships for Conventionally Expressed $M_2$AChRs*

After diminishing $I_{K,Basal}$ and establishing proper accelerated RGS kinetics, we sought to determine an ACh dose-response relationship for $M_2$AChR using conventional expression of the receptor. One issue we were particularly concerned with when performing these experiments was avoiding spare receptor conditions. When GPCRs significantly outnumber their downstream effectors, the signaling system is described as having spare receptors (Figure 3.8a). This disparity between GPCR and downstream effector numbers creates a situation where the downstream signal is saturated before the receptor binding site becomes saturated. Essentially, the signal saturates prematurely. As a consequence the dose-response relationship shifts and produces a lower $EC_{50}$ value (Figure 3.8b). To avoid spare receptors when we performed our experiments, we injected a series of different GIRK : $M_2$AChR mRNA ratios and monitored for shifts in $EC_{50}$.

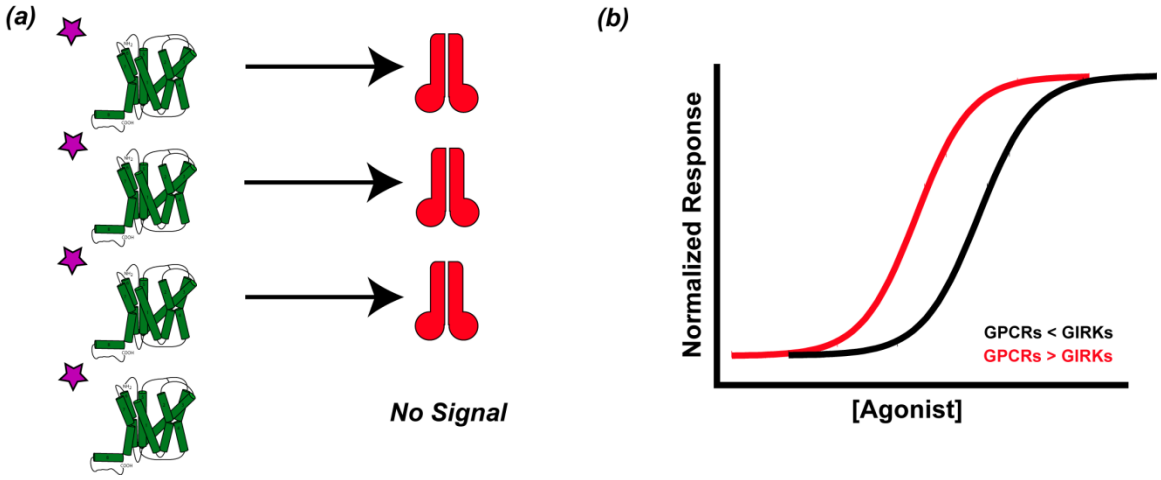


**Figure 3.8.** Scheme for spare receptors. ***(a)*** When GPCRs outnumber Girk channels, the downstream signal is saturated before the receptor binding site is saturated by drug. ***(b)*** Spare receptors (red) produce a shift in the dose-response relationship from the actual curve (black) towards lower $EC_{50}$ values.

(Throughout the rest of this chapter, we will be discussing two different types of $EC_{50}$ values. The first value is the $EC_{50}$ obtained when each cell's dose-response

relationship data is fit to the Hill equation. This value will be referred to as the cell $EC_{50}$, or $cEC_{50}$. The second value is our standard definition, where the responses to each drug dose are averaged across all cells and these averaged responses are fit to the Hill equation. This value will be referred to simply as $EC_{50}$. The two values, although similar, are not identical.)

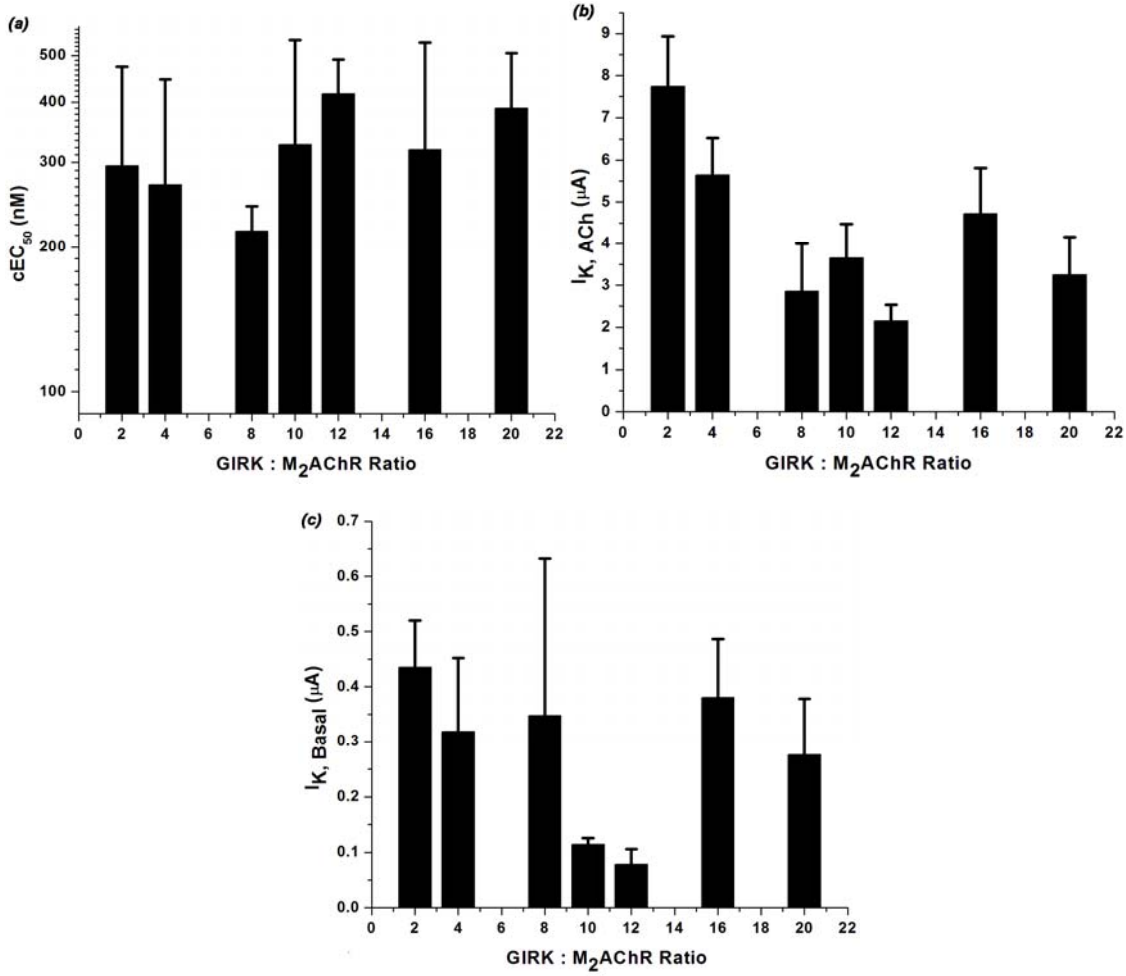


**Figure 3.9.** GIRK:$M_2$AChR mRNA injection ratio comparisons of $cEC_{50}$ ***(a)***, $I_{K,ACh}$ ***(b)***, and $I_{K,Basal}$ ***(c)***. One-way ANOVA test for differences between mRNA ratio groups show no significant difference for any of the three measurements. ($cEC_{50}$ F-value = 0.77; df = 6, 50; *p*-value = 0.6. $I_{K,ACh}$ F-value = 2.04; df = 6, 50; *p*-value = 0.8. $I_{K,Basal}$ F-value = 0.71; df = 6, 50; *p*-value = 0.6.) Cell counts for the conditions are N = 22, 16, 3, 4, 4, 3, and 5 for the 2, 4, 8, 10, 12, 16, and 20 Girk:$M_2$AChR mRNA ratio conditions, respectively. Error bars are standard deviation ***(a)*** and SEM ***(b)*** and ***(c)***.

The different injection ratios had no significant effect on current levels or $cEC_{50}$ values (Figure 3.9). The dose-response relationship remained the same from GIRK : $M_2$AChR mRNA ratios of 2:1 up through 20:1. We therefore concluded that we were not experiencing spare receptors in these experiments. When data from all 57 cells were combined, the $EC_{50}$ for conventionally expressed $M_2$AChR was 250 ± 10 nM ACh (Figure 3.10).

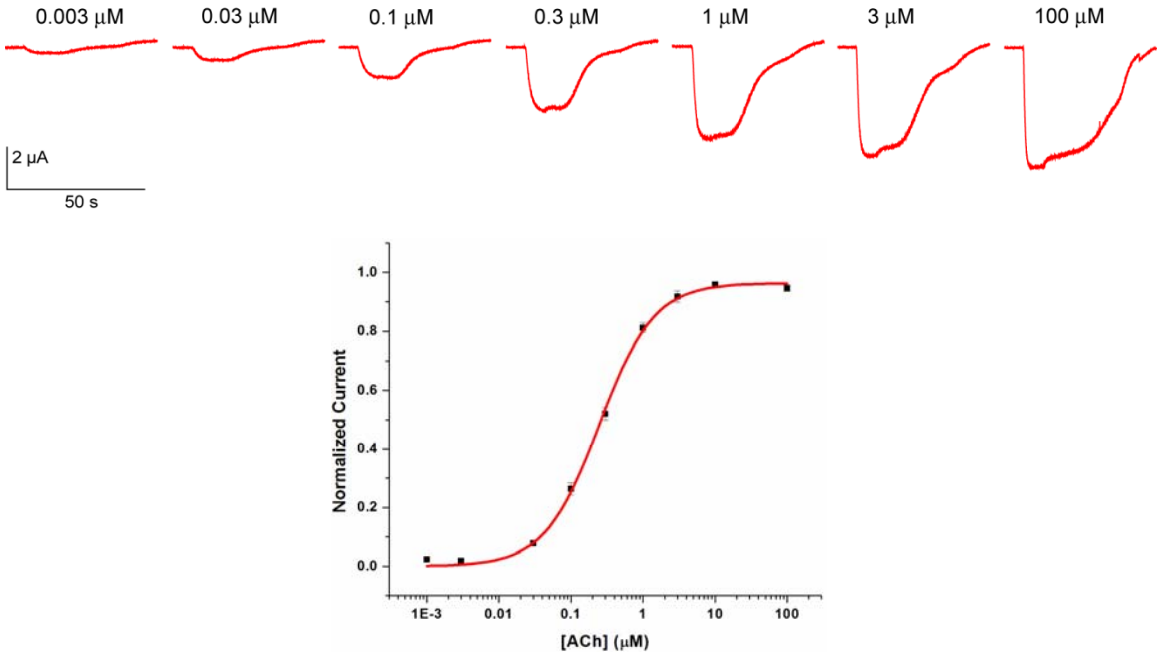


**Figure 3.10.** Conventional $M_2$AChR / GIRK 1/4 ACh dose-response experiment. *Top*: Sample $I_{K,ACh}$ traces with ACh dose concentrations. *Bottom*: Dose-response curve for N = 57 cells that were injected with varying GIRK 1/4: $M_2$AChR mRNA ratios and 2 ng $G\alpha_{oA}$ mRNA. Curve fit parameters: $EC_{50}$ = 250 ± 10 nM; $n_H$ = 1.2 ± 0.1

### *3.2.5 Wild-Type Recovery of $M_2$AChR*

Once we had assured ourselves that we had established an accurate dose-response relationship for wild-type $M_2$AChR through conventional expression, we next attempted to assay a wild-type receptor through nonsense suppression. In this wild-type recovery

experiment, a stop codon was placed at a specific site within the $M_2$AChR gene and THG73 tRNA ligated with the wild-type amino acid was injected into the cell to re-establish the wild-type protein. Following what we had learned in our conventional experiments, these nonsense suppression experiments included co-injection of $G\alpha_{oA}$ mRNA at the same time as the mutant $M_2$AChR and GIRK 1/4 mRNA and a subsequent injection of RGS4 mRNA 24 hours before recording.

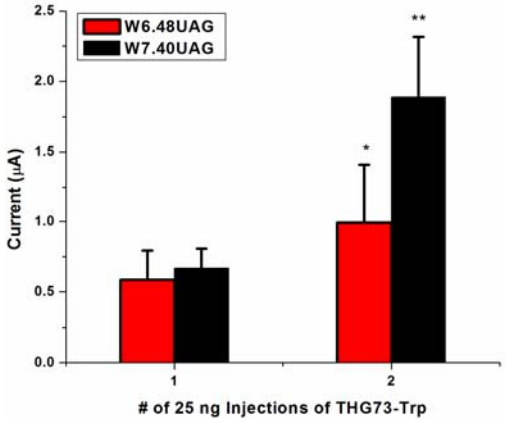


**Figure 3.11.** $I_{K,ACh}$ and number of suppressor tRNA injections. 20.5.2 W7.40UAG (black) and 20.5.0 W6.48UAG (red) conditions were used with 1 or 2 injections of 25 ng THG73-Trp. $I_{K,ACh}$ for the 1 injection conditions were 0.7 μA and 0.6 μA for the W7.40 and W6.48 conditions, respectively. A second injection of tRNA increased currents to 1.9 μA and 1.0 μA in the W7.40 and W6.48 experiments, respectively. (* *t*-test *p*-value = 0.02, with N = 9 for both injection conditions; ** *t*-test *p*-value = 0.03, with N = 9 for the 1 injection and N = 6 for the 2 injection conditions.) Error bars are SEM

(For the rest of this chapter, we will refer to suppression experiment conditions through a X.Y.Z triplet, where X is the amount of mutant $M_2$AChR mRNA, Y is the amount of mRNA for each GIRK subunit, and Z is the amount of $G\alpha_{oA}$ mRNA injected. In every case, 10 ng of RGS4 mRNA was injected 24 hrs before recording. As an example, 20.5.2 refers to the experiment where 20 ng of the $M_2$AChR mRNA, 5 ng each of GIRK1 and GIRK4 mRNA, and 2 ng of $G\alpha_{oA}$ mRNA were injected. A given nonsense suppression mutation will be described in the following manner: the site of stop codon mutation will be written with the X.50 numbering convention and the amino acid

incorporated at that position will be written with the three-letter amino acid code. W7.40Trp refers to an experiment at position W7.40, where Trp was incorporated at the position through nonsense suppression.)

In an attempt to produce optimal expression levels, we tried one and two injections of suppressor tRNA. The first injection always occurred along with the $M_2$AChR, GIRK, and Gα mRNAs 48 hrs prior to recording. A second injection was performed in some cells along with the RGS4 mRNA injection 24 hrs before assaying. We performed this injection study on two different mutants, W6.48Trp with injection conditions 20.5.0 (20.5.0 W6.48Trp) and W7.40Trp with injection conditions 20.5.2 (20.5.0 W7.40Trp). In both cases, a second injection of tRNA led to larger $I_{K,ACh}$ (Figure 3.11). These larger currents were interpreted as greater expression efficiency of the $M_2$AChR protein. We therefore adopted double tRNA injections as part of our GPCR nonsense suppression methodology.

Our initial nonsense suppression experiments also involved varying the amounts of mutant $M_2$AChR mRNA. We found that 20 ng of UAG mutant mRNA produced the most reliable expression of receptors and adequate $I_{K,ACh}$ levels. Because expression of proteins with incorporated unnatural amino acids is limited by the amount of tRNA we inject into the cell, we were not concerned about spare receptors. The low expression efficiency of nonsense suppression would ensure that $M_2$AChR expression levels never outpaced GIRK expression levels. GIRK mRNA injection amounts were also kept at 5 ng to further avoid spare receptors. At the end of these initial experiments, we arrived at the 20.5.2 suppression conditions with double tRNA injections. We then began to collect

ACh dose-response relationship data for wild-type recovery and unnatural amino mutant receptors.

### *3.2.6 $cEC_{50}$ Variability in Nonsense Suppression $M_2$AChR Experiments*

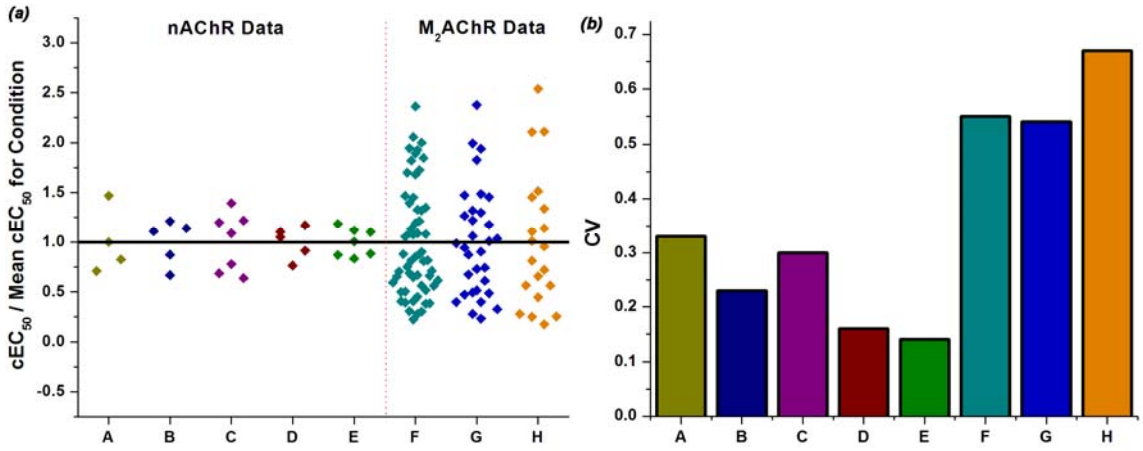


**Figure 3.12.** Cell-to-cell variability of nAChR and $M_2$AChR suppression data. ***(a)*** $cEC_{50}$ values normalized to the mean $EC_{50}$ for the condition. ***(b)*** Bar chart showing the CV values for the conditions in ***(a)***. $M_2$AChR suppression data has greater than twice the CV value of nAChR data (left side of ***(a)***). A: nAChR, D89Asp ACh data (CV = 0.33); B: nAChR, D89Akp ACh data (CV = 0.23); C: nAChR, D89Nha ACh data (CV = 0.30); D: nAChR, D89Akp Epi data (CV = 0.16); E: nAChR D89Nha Epi Data (CV = 0.14); F: $M_2$AChR conventional WT (CV = 0.55); G: $M_2$AChR 20.5.2 W7.40Trp (CV = 0.54); H: $M_2$AChR 20.5.2 W7.40$F_1$Trp (CV = 0.68)

Analysis of our dose-response relationship data for the first series of experiments with the 20.5.2 suppression conditions revealed two different types of variability in $cEC_{50}$ values. These first experiments involved the wild-type recovery mutant, W7.40Trp, and the incorporation of 5-F-Trp ($F_1$Trp) at W7.40, W7.40$F_1$Trp. The conventional $M_2$AChR data set and the two mutant data sets all exhibited twice the cell-to-cell $cEC_{50}$ variability as nAChR data when measured by the coefficient of variation (CV; Figure 3.12). The coefficient of variation is defined as the ratio of the standard deviation to the mean of a population. This variation can also be visualized by normalizing the $cEC_{50}$ values to the mean $cEC_{50}$ for a specific condition and observing the spread of data from 1 (Figure

3.12a); the standard deviation of the transformed data is equal to the CV of the non-transformed data.

With higher levels of cell-to-cell variability, we wondered what kind of shifts in $cEC_{50}$ or $EC_{50}$ we could interpret statistically. To address this concern, we derived a formula for the student's *t*-test in terms of CV and a z-fold shift in $cEC_{50}$ (details in Appendix B). This formula allowed us to determine what z-fold shifts in $EC_{50}$ could be significantly differentiated when the data had high CVs. When studying other receptors, we have not attempted to physically interpret 3-fold shifts and below. For data with a CV of 0.25 (nAChR data variability) or a CV of 0.5 ($M_2$AChR data variability), 3-fold shifts are significantly different at a > 99% confidence level. 3.5-fold shifts in $EC_{50}$ values can be significantly differentiated in populations with a CV of 1.0. Also, increasing the number of cells collected for each condition increases the statistical significance of small $cEC_{50}$ shifts. Because $cEC_{50}$ values are similar to $EC_{50}$ values, we assumed that significant shifts in $cEC_{50}$ data would produce significant shifts in $EC_{50}$ values. Therefore, the level of cell-to-cell variability of data observed in our $M_2$AChR conventional and suppression experiments were not so high as to prevent us from interpreting $EC_{50}$ shifts that we have considered to be significant in previous LGIC experiments.

But another type of data variability we observed in our nonsense expression experiments was not manageable. Compared to our conventional expression experiments, the batch-to-batch variability of $cEC_{50}$s was high (Figure 3.13); we define batch-to-batch variability as the variation in the mean $cEC_{50}$ for a batch of cells injected under the same conditions. The batch-to-batch CV of the 20.5.2 W7.40$F_1$Trp nonsense

suppression experiment conditions was twice that of the conventional expression experiment (Figure 3.13b).

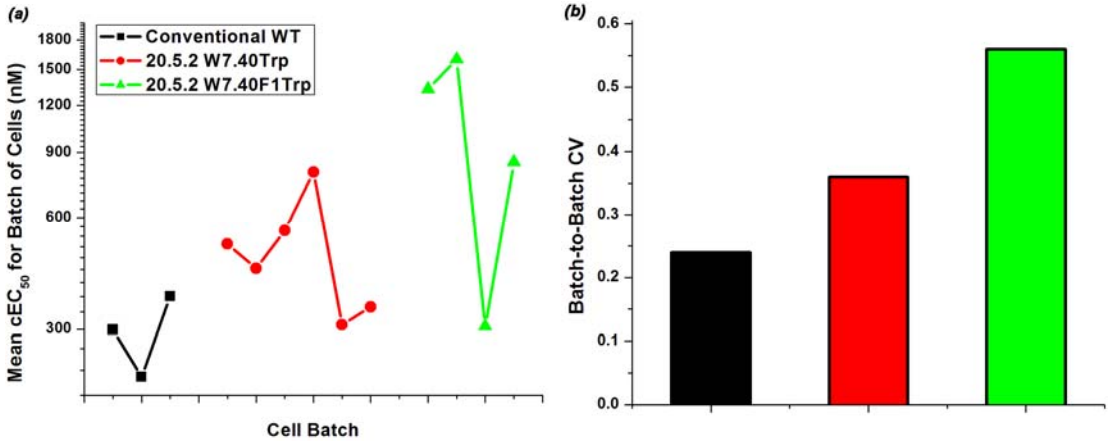


**Figure 3.13.** Comparison of batch-to-batch variability for conventional and suppression $M_2$AChR data. ***(a)*** Mean $cEC_{50}$ values for each cell batch in a given expression condition are plotted. ***(b)*** The batch-to-batch CV values for batch $cEC_{50}$s are shown. Condition colors match those in ***(a)***. Batch-to-batch CVs are 0.24, 0.36, and 0.56 for the conventional wild type, 20.5.2 W7.40Trp, and 20.5.2 W7.40$F_1$Trp conditions, respectively

**Table 3.1.** $cEC_{50}$ values for conventional and suppressed wild-type experiments based on $I_{K,ACh}$[a]

| | **$EC_{50}$** | **$n_H$*** | **N** |
|---|---|---|---|
| **Conventional WT (all cells)** | 250 ± 12 | 1.2 ± 0.1 | 57 |
| **Conventional WT ($I_{K,ACh}$ > 2 μA)** | 230 ± 8 | 1.2 ± 0.04 | 40 |
| **Suppressed WT (all cells)** | 440 ± 10 | 1.1 ± 0.03 | 30 |
| **Suppressed WT ($I_{K,ACh}$ > 2 μA)** | 300 ± 10 | 1.1 ± 0.1 | 16 |

[a]$EC_{50}$ (nM) and $n_H$ values are ± SEM.

### 3.2.6.1 Gα and Higher $cEC_{50}$ Values

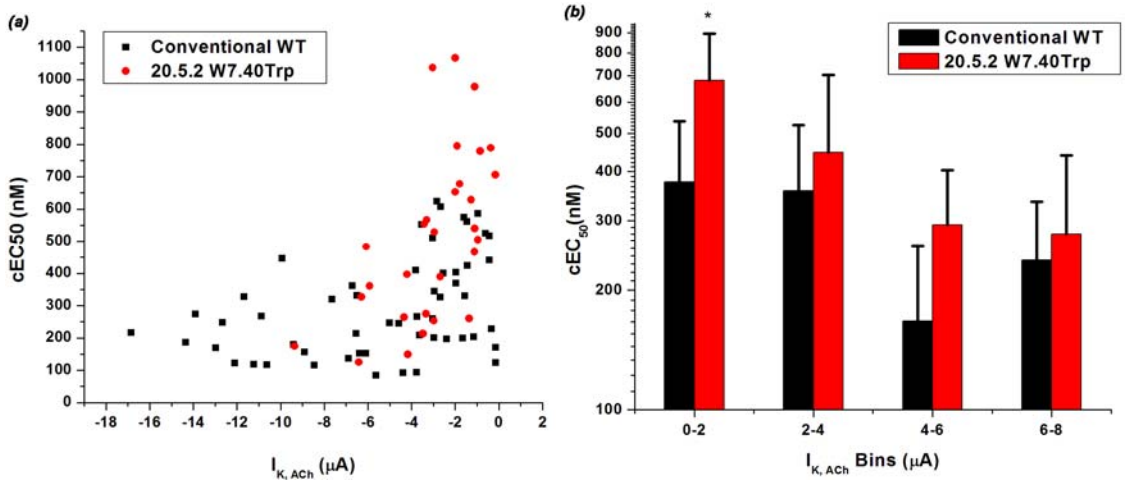


**Figure 3.14.** Suppression $M_2$AChR experiments exhibit higher $cEC_{50}$ values in cells with low $I_{K,ACh}$. ***(a)*** When $I_{K,ACh}$ is plotted with $cEC_{50}$, conventional and suppressed wild-type data diverge most for cells with $I_{K,ACh}$ < 2 μA. ***(b)*** Cell data are placed in 2 μA current bins. * *t*-test *p*-value < 0.001. In the four current bins, N = 15 and 13 for the 0 to 2 μA bin, N = 14 and 9 for the 2 to 4 μA bin, N = 4 and 4 for the 4 to 6 μA bin, and N = 7 and 4 for the 6 to 8 μA bin, for the conventional and suppressed conditions, respectively. Error bars are standard deviations

In addition to the batch-to-batch variability of the nonsense suppression data, we also observed an upward shift in the $EC_{50}$ value for the entire 20.5.2 W7.40Trp data set (440 nM) compared to the conventional wild-type experiment (240 nM; Table 3.1). To try to remedy this elevated wild-type recovery $EC_{50}$ and, hopefully, the batch-to-batch data variability, we began to search for trends between $cEC_{50}$ and other properties of our $M_2$AChR-GIRK 1/4 signaling system. When we analyzed the relationship between $I_{K,ACh}$ and $cEC_{50}$, we found that cells from our nonsense suppression experiments with low $I_{K,ACh}$ had higher $cEC_{50}$ values on average than cells with equivalent current levels in the conventional expression experiments (Figure 3.14). In fact, separating cells from both conventional and 20.5.2 W7.40Trp experiments into 2 μA bins showed that the two data sets only differed significantly in the 0 to 2 μA current bin (Figure 3.14b). If cells with $I_{K,ACh}$ less than 2 μA were removed from both data sets, the difference between the two

$EC_{50}$ values narrowed (230 nM and 300 nM for the conventional and nonsense suppression experiments, respectively; Table 3.1). We concluded that low levels of $M_2$AChR expression in the nonsense suppression experiments, which would lead to low $I_{K,ACh}$ levels, were producing abnormally shifted ACh dose-response relationships.

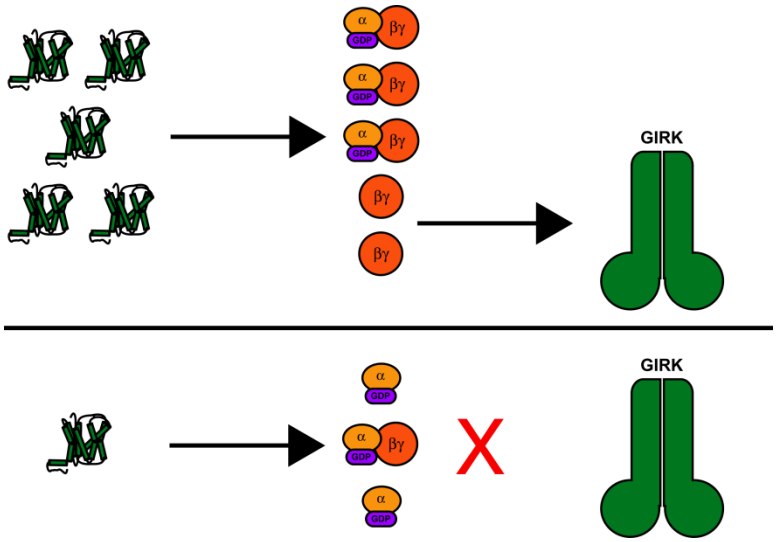


**Figure 3.15.** Possible explanation of low $I_{K,ACh}$ / high $cEC_{50}$ phenomenon. Co-injection of $G\alpha_{oA}$ mRNA produces greater amounts of $G\alpha_{oA}$ protein that can block free $G\beta\gamma$. In cells with average-to-high GPCR expression (*top*), higher amounts of $G\alpha_{oA}$ do not affect GPCR-mediated free $G\beta\gamma$ signaling to downstream GIRK channels. But, if GPCR expression is low (*bottom*) and low amounts of GPCR-mediated free $G\beta\gamma$ are produced, then the higher amounts of $G\alpha_{oA}$ will block free $G\beta\gamma$ and a higher dose of drug will be required to produce the same level of GIRK signal

One possible explanation for this connection between expression levels and dose-response relationships is the injection of $G\alpha_{oA}$ mRNA. Nonsense suppression produces lower levels of receptor expression than conventional expression methods. Lower receptor expression would produce a lower flux of free $G\beta\gamma$ subunits in response to ACh application. With the injection of $G\alpha_{oA}$ mRNA, there would also be an increased level of free $G\alpha$ inside the cell, which could bind to free $G\beta\gamma$ subunits and prematurely terminate $M_2$AChR-GIRK signaling (Figure 3.15). Therefore, a higher dose of ACh would be needed in low-expressing cells to produce the equivalent amount of signal as in normally

expressing cells. Such a phenomenon would shift the dose-response relationship to higher $cEC_{50}$ values.

**Table 3.2.** $EC_{50}$ values for conventional and suppressed wild-type experiments with varying amounts of co-injected $G\alpha_{oA}$ mRNA[a]

| | **$EC_{50}$** | **$n_H^*$** | **N** |
|---|---|---|---|
| **Conventional WT (2 ng $G\alpha_{oA}$)** | 250 ± 10 | 1.2 ± 0.1 | 57 |
| **Conventional WT (0 ng $G\alpha_{oA}$)** | 240 ± 30 | 0.8 ± 0.1 | 9 |
| **Suppressed WT (2 ng $G\alpha_{oA}$)** | 440 ± 10 | 1.1 ± 0.03 | 30 |
| **Suppressed WT (1 ng $G\alpha_{oA}$)** | 400 ± 10 | 0.9 ± 0.03 | 20 |
| **Suppressed WT (0 ng $G\alpha_{oA}$)** | 290 ± 30 | 0.8 ± 0.1 | 17 |

[a]$EC_{50}$ (nM) and $n_H$ values are ± SEM.

To test this hypothesis and reduce data variability, we performed a series of W7.40Trp experiments where we reduced the amount of $G\alpha_{oA}$ mRNA injected and monitored the change in mean $cEC_{50}$. Cells with 0 ng of injected $G\alpha_{oA}$ mRNA had $cEC_{50}$s that were not significantly different from the conventional expression experiments and significantly lower than cells with 2 ng or 1 ng of $G\alpha_{oA}$ mRNA (Figure 3.16a). When all of the cells from each condition were pooled together, the $EC_{50}$ for 20.5.0 W7.40Trp was 290 nM, similar to the conventional wild-type $EC_{50}$ of 240 nM (Table 3.2). To ensure that removing $G\alpha_{oA}$ from conventional expression experiments did not change the dose-response relationship, we determined the $EC_{50}$ for a $G\alpha$-free conventional expression experiment and found no difference from the previous $EC_{50}$.

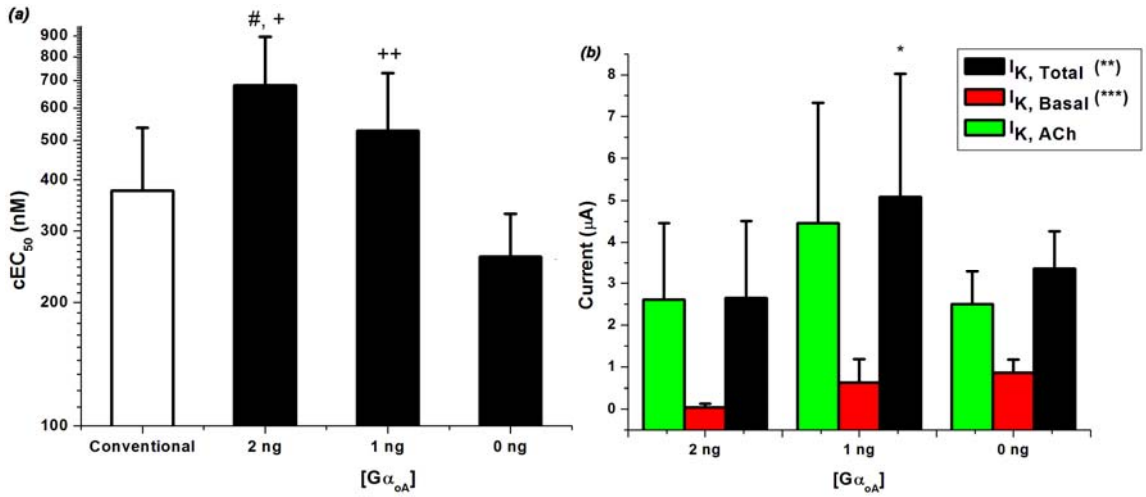


**Figure 3.16.** $G\alpha_{oA}$ / $cEC_{50}$ mRNA experiments. ***(a)*** Varying the amount of $G\alpha_{oA}$ mRNA injected in suppression experiments affects $cEC_{50}$ values. + *t*-test for comparison of 2 ng to 0 ng, *p*-value = 0.002; ++ *t*-test comparison of 1 ng to 0 ng, *p*-value = 0.02; # comparison of 2 ng to conventional, *p*-value = 0.002. ***(b)*** Lowering $G\alpha_{oA}$ mRNA amounts also affected $I_{K,Total}$ and $I_{K,basal}$ levels. *** One-way ANOVA test for $I_{K,Basal}$ differences between the three injection conditions, F-value = 56.34, df = 2, 62, and *p*-value << 0.001. ** One-way ANOVA test for $I_{K,Total}$ differences between the three injection conditions, F-value = 8.03, df = 2, 62, and *p*-value < 0.001. * T-test for $I_{K,Basal}$ difference between 2 ng and 1 ng, *p*-value = 0.001. Error bars are standard deviation

Not surprisingly, the removal of $G\alpha_{oA}$ mRNA from our suppression experiments significantly increased $I_{K,Basal}$ (Figure 3.16b). Interestingly, the 20.5.1 W7.40Trp conditions yielded the highest level of $I_{K,Total}$ ($I_{K,ACh}$ + $I_{K,Basal}$). It is unclear why the $G\alpha_{oA}$-free conditions did not produce higher $I_{K,Total}$ levels.

### *3.2.6.2 Batch-to-Batch $cEC_{50}$ Variability*

While removing $G\alpha_{oA}$ mRNA injections from our experimental conditions returned wild-type recovery $EC_{50}$ values to an appropriate number, it did not reduce the overall data variability. The 20.5.0 W7.40F1Trp data set had a cell-to-cell CV of 1.03 (Figure 3.17) and a batch-to-batch CV of 1.05 (Figure 3.18); both CVs were greater than the conventional wild-type and the 20.5.2 W7.40F1Trp data sets.

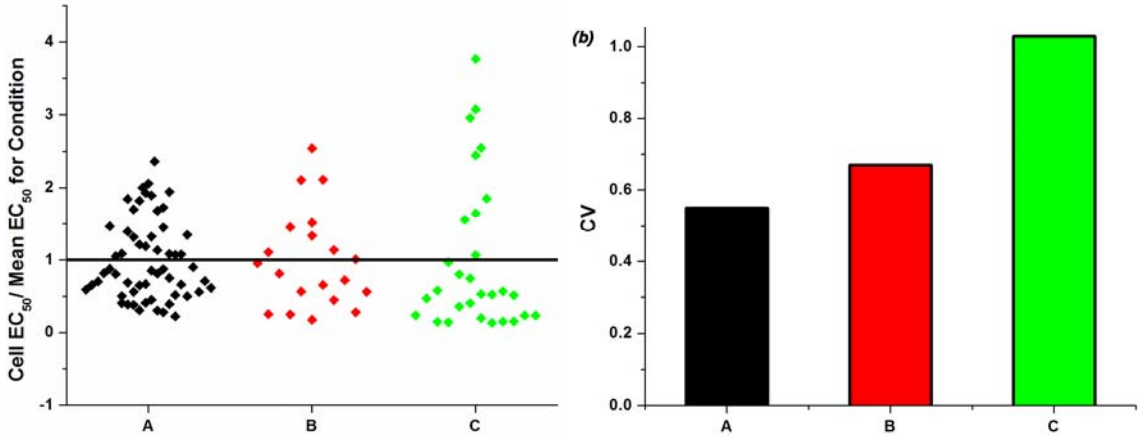


**Figure 3.17.** Cell-to-cell variability for conventional wild-type (A), 20.5.2 W7.40F$_1$Trp (B), and 20.5.0 W7.40F$_1$Trp (C). ***(a)*** cEC$_{50}$ values are normalized to the mean EC$_{50}$ for the condition. ***(b)*** The CVs for each condition's distribution are presented: A, CV = 0.55; B, CV = 0.68; C, CV = 1.03

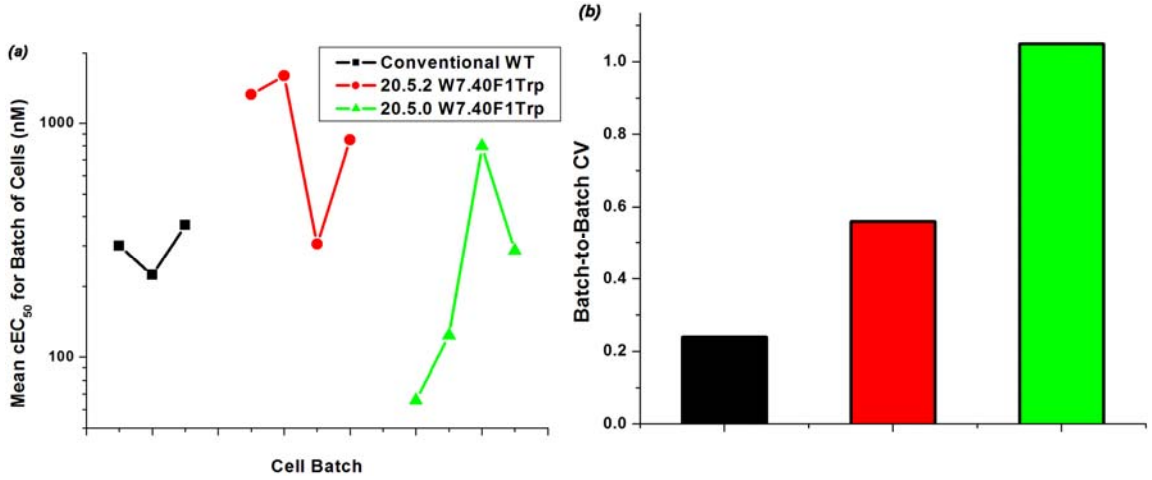


**Figure 3.18.** Batch-to-batch variability of conventional WT (black), 20.5.2 W7.40F$_1$Trp (red), and 20.5.0 W7.40F$_1$Trp (green). ***(a)*** Mean cEC$_{50}$ values for each cell batch of a given condition are plotted. ***(b)*** Batch-to-batch CV values for each condition are presented: conventional WT, CV = 0.24; 20.5.2 W7.40F$_1$Trp, CV = 0.56; 20.5.0 W7.40F$_1$Trp, CV = 1.05

Our next attempt to solve this variability involved varying the injection ratios of mutant $M_2$AChR and GIRK 1/4 mRNA. We wondered if lowering the $M_2$AChR : GIRK 1/4 mRNA ratio would decrease the CV of our data. Four nonsense suppression experimental conditions were compared: 20.5.0, 20.10.0, 10.10.0, and 2.5.0 had $M_2$AChR : GIRK 1/4 ratios of 4, 2, 1, and 0.4, respectively. A strong correlation (R = 0.98) was found between the mRNA ratio and the cell-to-cell CV (Figure 3.19). Although the 2.5.0 experimental conditions had the least variability, the expression efficiency was quite low

and irregular. We therefore decided to examine the batch-to-batch variability of sets of 10.10.0 suppression data.

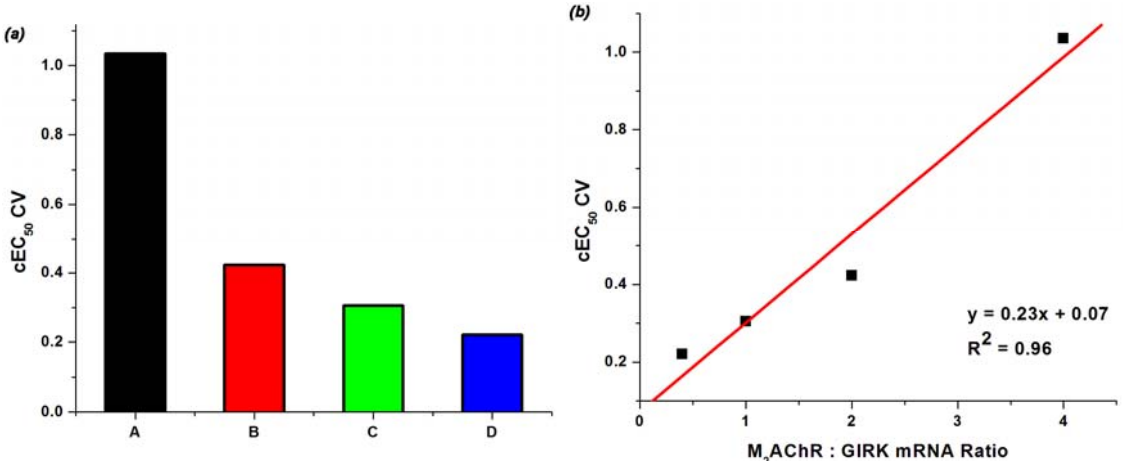


**Figure 3.19.** $M_2$AChR : GIRK mRNA injection ratio improves cell-to-cell variability. ***(a)*** Four different mRNA ratios were tested and cell-to-cell CV values were determined. (A: 20.5.0, CV = 1.03; B: 20.10.0, CV = 0.42; C: 10.10.0, CV = 0.30; D: 2.5.0, CV = 0.22). ***(b)*** A strong linear correlation between mRNA ratio and CV was found. In all four conditions, the suppression experiment measured W7.40$F_1$Trp $EC_{50}$ values

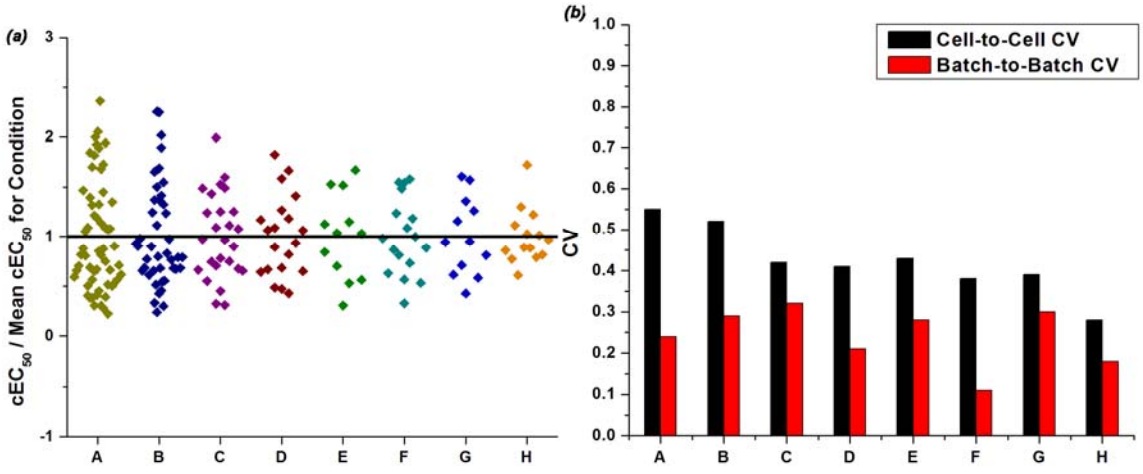


**Figure 3.20.** Variability of data from suppression experiments with 10.10.0 injection conditions. ***(a)*** $cEC_{50}$ variability shown through normalizing $cEC_{50}$ values to the mean $cEC_{50}$ for the given condition. ***(b)*** CV values for cell and mean batch $cEC_{50}$ values reported for each condition. (A: conventional WT, CV = 0.55 and 0.24; B: W7.40Trp, CV = 0.52 and 0.29; C: W7.40$F_1$Trp, CV = 0.42 and 0.32; D: W7.40$F_2$Trp, CV = 0.41 and 0.21; E: W7.40$F_3$Trp, CV = 0.43 and 0.28; F: W6.48Trp, CV = 0.38 and 0.11; G: W6.48$F_2$Trp, CV = 0.39 and 0.3; H: W6.48$F_3$Trp, CV = 0.28 and 0.18. CVs are cell-to-cell and batch-to-batch, respectively.)

Seven different sets of 10.10.0 data were obtained for mutations at two different sites in the $M_2$AChR, W6.48 and W7.40 (Figure 3.20). Cell-to-cell CVs for the 10.10.0 data sets ranged from 0.28 to 0.52 (the equivalent conventional CV was 0.54) and the batch-to-batch CVs ranged from 0.11 to 0.32 (the equivalent conventional CV was 0.24). The data from these seven data sets suggest that the 10.10.0 conditions are the optimal conditions for consistent nonsense suppression data in the $M_2$AChR-GIRK 1/4 signaling system.

### *3.2.6.3 Explanations of the $cEC_{50}$ Variability*

To understand the source of the variability of the 20.5.0 data, we examined three different possible mechanisms. Our first hypothesis involved expression of an endongenous oocyte GIRK subunit, GIRK5 or XIR[73]. GIRK5 is capable of forming heterotetramers with GIRK1. If the GIRK 1/5 channel had different signaling properties from the GIRK 1/4 channel, different $EC_{50}$ values could be obtained. It is possible that different batches of cells have different levels of GIRK5 endogenous expression. To try to assess the expression levels of these channels, we injected $M_2$AChR mRNA with GIRK1 mRNA only. $I_{K,ACh}$ would only be produced in cells that were expressing GIRK5, because GIRK1 is incapable of forming functional homotetramers. Through three batches of oocytes, we did not once observe detectable $I_{K,ACh}$ from GIRK1-only injected cells. We concluded that our oocytes had low-to-negligible levels of endogenous GIRK5 expression, and thus GIRK5 was not the source of our variability.

Another possible explanation for batch-to-batch variability we considered was oocyte maturation-dependent differences in the expression levels of proteins in the GPCR-GIRK signaling network, such as Gβγ, β-arrestin, or GRK. Changes in the expression levels of these proteins could subtly change the signaling profile of the GPCRs. Our oocytes are harvested between maturation stages V and VI. We wondered if during this transition the levels of proteins in the signaling system fluctuate and thus cause changes in dose-response relationships.

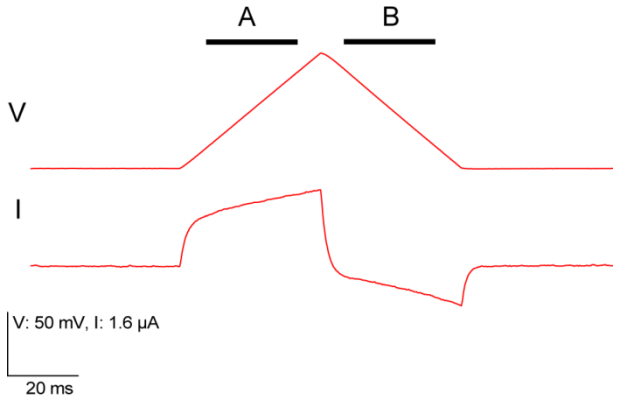


**Figure 3.21.** Sample of $C_m$ measurement. First ramp begins at a holding potential of -60 mV and ends at +20 mV, while the second ramp starts at +20 mV and finishes at -60 mV. (A: samples 159 to 236; B: samples 282 to 359; ΔV = 50 mV)

To test this possibility, we first determined if $cEC_{50}$ values changed with maturation stage. Oocytes increase in size during the transition from stage V to stage VI; this increase in cell diameter would also increase the membrane capacitance ($C_m$). In a collection of 10.10.0 W7.40Trp cells, we measured $C_m$ through paired voltage ramps as described in Figure 3.21. No significant correlation was found between $C_m$ and $cEC_{50}$ ($R = 0.09$) and we concluded that the maturation stage did not affect $cEC_{50}$ values.

The third and final hypothetical source of variability we tested was whether the same dose of ACh elicited the same current response throughout the course of a dose-

response relationship experiment. We spaced five test doses of 0.3 μM ACh equally throughout the ten dose series of a 10.10.0 W7.40Trp experiment (right side of Figure 3.22) and determined the percent change in response relative to the first test dose. As shown in Figure 3.22, on average, the responses increased throughout the experiment until the final test dose, where it decreased significantly. When the penultimate 10 μM dose was removed from the series of doses, we saw no significant drop in response, suggesting that the drop at test dose #5 is due to desensitization caused by two successive saturating doses of ACh. This decrease in response may also have been due to poor cell health at the end of the experiment.

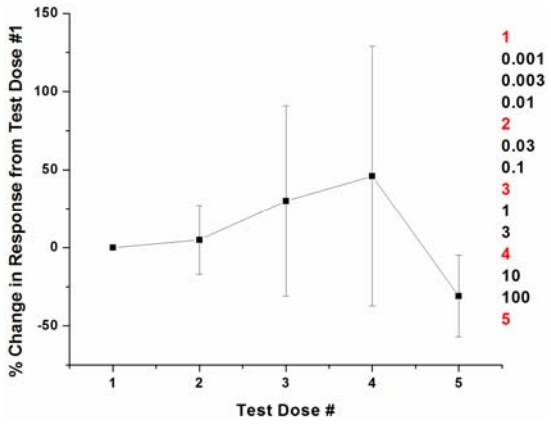


**Figure 3.22.** Varying responses to a test dose of ACh throughout the course of a dose-response experiment. A test pulse of 0.3 μM ACh was applied to cells at positions 1, 2, 3, 4, and 5 in the dose-response experiment (*right*). Percent change in current response is measured relative to test dose #1. Error bars are standard deviations. (% at 2 = 5 ± 20%, % at 3 = 30 ± 60%, % at 4 = 50 ± 80 %, and % at 5 = -30 ± 30 %.)

We wondered if the change in responses observed at test doses #2 through #4 could be responsible for the data variability we observed. Through an unknown biological mechanism, increased current responses during an experiment could skew dose-response relationships to higher $cEC_{50}$ values. To investigate this possibility, we simulated dose response data using an asymmetric current change model based on the

data we had collected (see Appendix C for full description). The model we constructed started with an ideal set of dose-response data with an $EC_{50}$ value of 140 nM; these data were then modified through current changes that were randomly sampled from current changes we recorded. $cEC_{50}$ values from five collections of simulated data sets were not significantly different in distribution from the actual 10.10.0 W7.40Trp data we collected (Figure 3.23 and Table 3.3): both the means and variances of the simulated data were similar to the actual data. This data simulation exercise suggests that an asymmetric current change model, in which the responses to drug increase as the experiment progresses, could explain the variability in dose-response relationship data.

**Table 3.3.** Actual 10.10.0 W7.40Trp data and five simulated data sets[a]

| | **Mean $cEC_{50}$** | **SD** | **CV** | ***t*-test p[b]** | **F-test p[b]** |
|---|---|---|---|---|---|
| **Actual Data** | 230 | 120 | 0.52 | - | - |
| **Rand1** | 230 | 150 | 0.64 | 0.9 | 0.2 |
| **Rand2** | 210 | 120 | 0.58 | 0.4 | 0.9 |
| **Rand3** | 230 | 130 | 0.58 | 0.9 | 0.5 |
| **Rand4** | 180 | 100 | 0.54 | 0.05 | 0.2 |
| **Rand5** | 190 | 90 | 0.47 | 0.07 | 0.05 |

[a]One-way ANOVA test for difference between the six data sets showed no significant difference between the sets: F-value = 1.48, df = 5,240, *p*-value = 0.2.
[b]F- and *t*-tests were performed between each simulated data set and the actual data set.

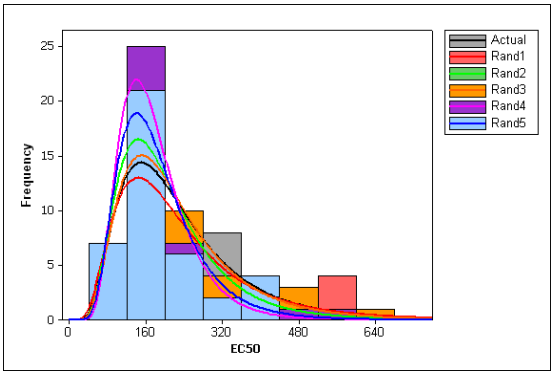


**Figure 3.23.** Histogram of actual 10.10.0 W7.40Trp data with five simulated data sets. Log-normal distribution fits shown. (Shape parameters are as follows: actual data: $\mu = 5.3$, $\sigma = 0.54$; Rand1: $\mu = 5.3$, $\sigma = 0.57$; Rand2: $\mu = 5.2$, $\sigma = 0.49$; Rand3: $\mu = 5.3$, $\sigma = 0.52$; Rand4: $\mu = 5.1$, $\sigma = 0.40$; Rand5: $\mu = 5.1$, $\sigma = 0.44$.)

### *3.2.7 Fluorinated Trp Series at W3.28, W6.48, and W7.40*

With a set of suppression experiment conditions that produced stable, reliable data, we proceeded to our second goal: we began to probe aromatic residues in the $M_2$AChR binding site in search of a cation-$\pi$ interaction. Three Trp residues were chosen as likely candidates. We chose Trp residues over Phe and Tyr residues because the calculated cation-$\pi$ binding energy for the indole ring is greater than that of the other aromatic side chains (32.6 kcal/mol compared to 27.1 kcal/mol and 26.9 kcal/mol for benzene and phenol, respectively[74]). W3.28 was chosen due to its position four amino acids—approximately one turn of a helix—above the highly conserved D3.32. This position could place the indole ring in the appropriate orientation to interact with the quaternary amine of ACh as it forms an electrostatic interaction with the negatively charged Asp. W6.48 is highly conserved throughout the rhodopsin-like family of GPCRs. Rhodopsin studies have shown that the Trp side chain makes an important contact with 11-*cis*-retinal—the covalently bound agonist of rhodopsin that undergoes

photoisomerization to activate the receptor—during rhodopsin activation[25,26]. Finally, W7.40 is the most uniquely conserved residue in the aminergic class of GPCRs besides D3.32, as determined by taking all residues conserved in the aminergic class and removing residues that are also conserved in other classes of rhodopsin-like receptors[75]. Also, in the 5-$HT_{2A}$ receptor, the W7.40A mutation completely abolishes agonist binding[76].

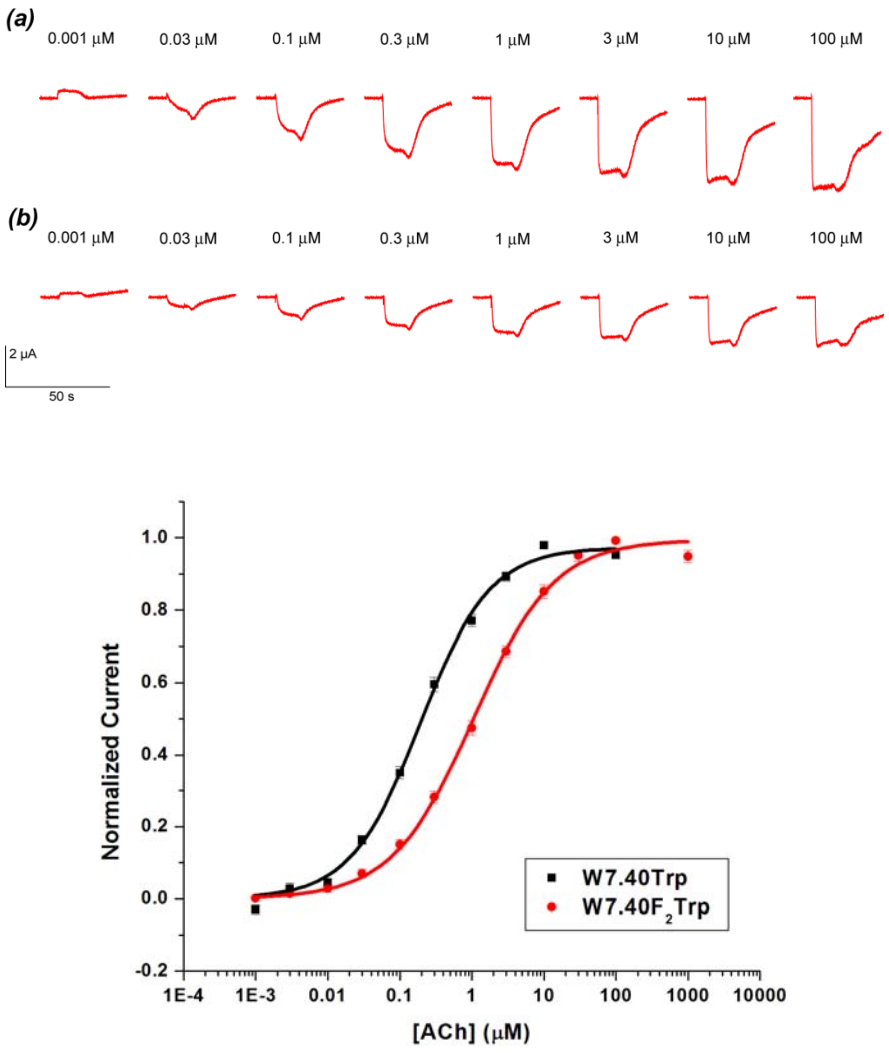


**Figure 3.24.** Dose-response experiment for 10.10.0 suppression conditions. *Top*: Sample traces of 10.10.0 W7.40Trp ***(a)*** and 10.10.0 W7.40$F_2$Trp ***(b)*** dose-response experiments. *Bottom*: Dose-response relationships fit to the Hill equation shown for the two conditions shown above

**Table 3.4.** $F_n$Trp series data at W7.40, W6.48, and W3.28[a]

| | $EC_{50}$ | $n_H$* | N |
|---|---|---|---|
| **W7.40** | | | |
| **Trp** | 190 ± 20 | 0.9 ± 0.1 | 41 |
| **F1Trp** | 240 ± 9 | 0.9 ± 0.03 | 26 |
| **F2Trp** | 1000 ± 80 | 0.8 ± 0.04 | 20 |
| **F3Trp** | 170 ± 10 | 0.9 ± 0.05 | 12 |
| **W6.48** | | | |
| **Trp** | 310 ± 6 | 0.8 ± 0.01 | 17 |
| **F2Trp** | 1100 ± 70 | 0.8 ± 0.04 | 12 |
| **F3Trp** | 420 ± 30 | 1.1 ± 0.06 | 14 |
| **W3.28** | | | |
| **dCA** | 1900 ± 80 | 0.8 ± 0.02 | 12 |

[a]$EC_{50}$ (nM) and $n_H$ values are ± SEM.

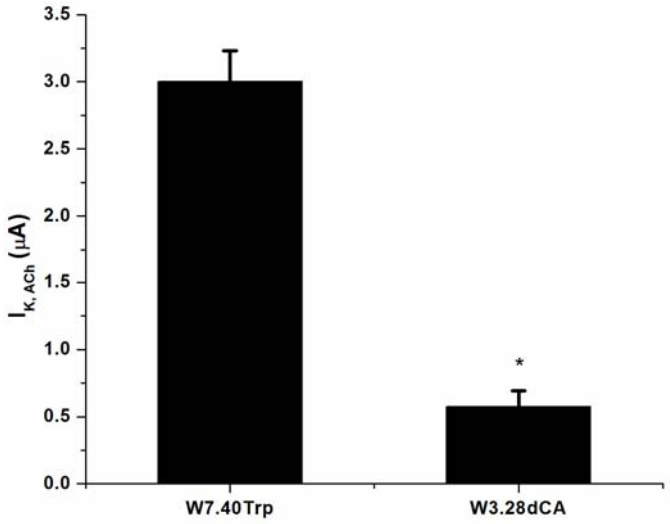


**Figure 3.25.** $I_{K,ACh}$ comparison between W7.40Trp and W3.28dCA. Both use 10.10.0 suppression conditions. The reaminoacylation current (W3.28dCA) was 5 times lower than the W7.40Trp currents: 3.0 ± 0.2 μA compared to 0.6 ± 0.1 μA. * *t*-test *p*-value << 0.001. Error bars are SEM

The fluorinated Trp analogs, 5-F-Trp ($F_1$Trp), 5,7-$F_2$-Trp ($F_2$Trp), and 5,6,7-$F_3$-Trp ($F_3$Trp), were incorporated at W7.40, while $F_2$Trp and $F_3$Trp were incorporated at W6.48. Examples of W7.40Trp and W7.40$F_2$Trp data are shown in Figure 3.24, and Table 3.4 summarizes the fluorinated Trp series data. Incorporation of $F_2$Trp produced 5- and 3.5-fold shifts in $EC_{50}$ at W7.40 and W6.48, respectively. The other fluorinated Trp residues did not shift $EC_{50}$ values at W7.40 or W6.48. When we performed the misacylation control experiment at W3.28 (injection of THG73-dCA), we observed definite, albeit low, $I_{K,ACh}$ (Figure 3.25). A dose-response relationship experiment on W3.28dCA yielded an $EC_{50}$ of 1900 nM, a 10-fold increase from wild type (Table 3.4).

## 3.3 Discussion

### *3.3.1 Optimal Conditions for the Incorporation of Unnatural Amino Acids into $M_2$AChR*

After controlling for adequate expression efficiencies and consistent dose-response relationship data, we arrived at the 10.10.0 conditions for our nonsense suppression experiments. Under these conditions, we inject 10 ng of the stop codon mutant $M_2$AChR mRNA, 10 ng each of GIRK1 and GIRK4 mRNA, along with 25 ng of the suppressor tRNA ligated with our amino acid of choice 48 hours prior to recording. 24 hrs later, we inject another 25 ng of tRNA and 10 ng of RGS4 mRNA.

The double injection of tRNA was necessary for high levels of expression, as measured by $I_{K,ACh}$ (Figure 3.11). RSG4 expression was used to provide more uniform, faster electrophysiology traces through the ability of the protein to accelerate both the

activation and deactivation of $M_2$AChR-GIRK 1/4 signaling (Figure 3.7). Injecting the RGS4 mRNA a day later than the rest of the mRNA allowed for more consistent expression of the RGS protein as observed through changes to trace kinetics. We believe that this delay in injection provides the cell's translation and membrane trafficking machinery a chance to process the $M_2$AChR and GIRK mRNA before expressing the RGS4 protein. Although in conventional expression experiments, co-injection of $G\alpha_{oA}$ lowered $I_{K,Basal}$ and increased $I_{K,ACh}$, we found that in nonsense suppression experiments this additional expression of $G\alpha_{oA}$ protein resulted in increased wild-type $cEC_{50}$s (Figure 3.16). We proposed that a large amount of $G\alpha_{oA}$ expression prematurely terminates G-protein signaling in the cell by binding free $G\beta\gamma$ released by active receptors. Finally, to avoid substantial batch-to-batch and cell-to-cell $cEC_{50}$ variability, we found that equal-to-low $M_2$AChR : GIRK 1/4 mRNA injection ratios were necessary (Figure 3.20). Increasing the amount of GIRK mRNA was necessary to keep an equal ratio with $M_2$AChR mRNA, while still injecting enough mutant $M_2$AChR mRNA to allow for efficient expression of receptor. We also found that injecting cells with wild-type recovery conditions alongside cells with mutant conditions provided a good means to assess the variability of a given batch of cells.

### *3.3.2 What Causes $cEC_{50}$ Variability in Suppressed $M_2$AChR Experiments?*

By far, the biggest struggle during this project was overcoming the data variability in the nonsense suppression experiments. Perhaps it is not surprising that GPCR data would have higher variability than LGIC data. In our LGIC experiments,

drug action on the receptor of study and detectable signal were connected directly: drug binding caused a conformational change in the receptor that allowed current to pass through the cell membrane. But, in our GPCR system, multiple steps separate drug action from current signals. These steps require multiple proteins within the cell. The expression levels of some of these proteins, like GIRK, we can control, but there are others over which we have no control, like the G-protein. Other cellular pathways can intersect with these players in our signaling system. Gβγ can interact with GRKs, which can then phosphorylate our receptor to terminate signaling. Gα proteins from the $G_{i/o}$ family can also inhibit the synthesis of cAMP by AC, which can alter cAMP levels within the cell. Combine the variability caused by this spider web of cellular pathways with the variability inherent in the nonsense suppression methodology and greater fluctuations in $cEC_{50}$s are inevitable.

Unfortunately, the reason why the 10.10.0 injection conditions remedied the problem is not quite clear. The endogenous GIRK5 and maturation state hypotheses seemed to be strong possible explanations, but we did not detect GIRK5 expression in our cells and our measurement of maturation state ($C_m$) did not correlate with $cEC_{50}$.

The remaining explanation was provided by data from our test dose experiments (Figure 3.22). By repeating the same concentration of ACh at 5 different times during a dose-response relationship, we were able to detect a significant upward trend in responses to the same dose as the experiment progressed. Most of the changes in current responses occur around and after the midway point of the dose-response series (test dose #3). Therefore, it appeared that the first half of the dose series was unaffected by these current changes. But, in the second half, responses began to increase. This asymmetric upward

trend would effectively stretch the second half of the dose-response relationship higher than its normal state. Upon normalization, the dose-response relationship would be warped towards higher $EC_{50}$ values. If the degree of these asymmetric current changes varied from cell to cell or batch to batch—and given the large standard deviations observed in our collected current change data, this appeared to be likely—large batch and cell variation in $cEC_{50}$ data would be expected.

Our data simulation trials (described in detail in Appendix C), in which we utilized an asymmetric current change model on an ideal set of dose-response data, supports this hypothesis. The simulated data resembled our actual 10.10.0 W7.40Trp data in mean and variance (Figure 3.23 and Table 3.3). Unfortunately, we did not collect data on the change in responses during dose-response experiments for the 20.5.0 W7.40F1Trp trials, in which the cell-to-cell and batch-to-batch CVs were around 1. But this model suggests that data with such high variability should exhibit response changes during an experiment that are greater and even more asymmetric than the data collected in the 10.10.0 experiments. We would predict that the percent change at test dose #2 would not differ much from the 10.10.0 data, but that later test doses, #3 and #4, would show larger percent changes.

Even though this asymmetric current change model provides a source of the data variability, it does not provide a biological explanation for the variability. What cellular mechanism could cause such changes in response to the same dose of drug in the course of an experiment? The most likely explanation is some combination of changes in the receptor internalization and surface trafficking machineries. One way to test this hypothesis would be to perform a similar repeated dose experiment on non-desensitizing

$M_2$AChRs[77,78]. If the internalization process is the source of current changes, these mutants would eliminate the phenomenon because the non-desensitizing receptors would not be internalized. If the source of these response changes is an increase in surface trafficking over the course of an experiment, these mutations should produce larger response changes because internalization would be shut down. It is also entirely possible that response changes and their connection to equal or low $M_2$AChR : GIRK 1/4 mRNA injection ratios have multiple or complex causative factors. Thus, the connection may be simply phenomenological.

### *3.3.3 No Cation-π Interaction Site at W3.28, W6.48, or W7.40*

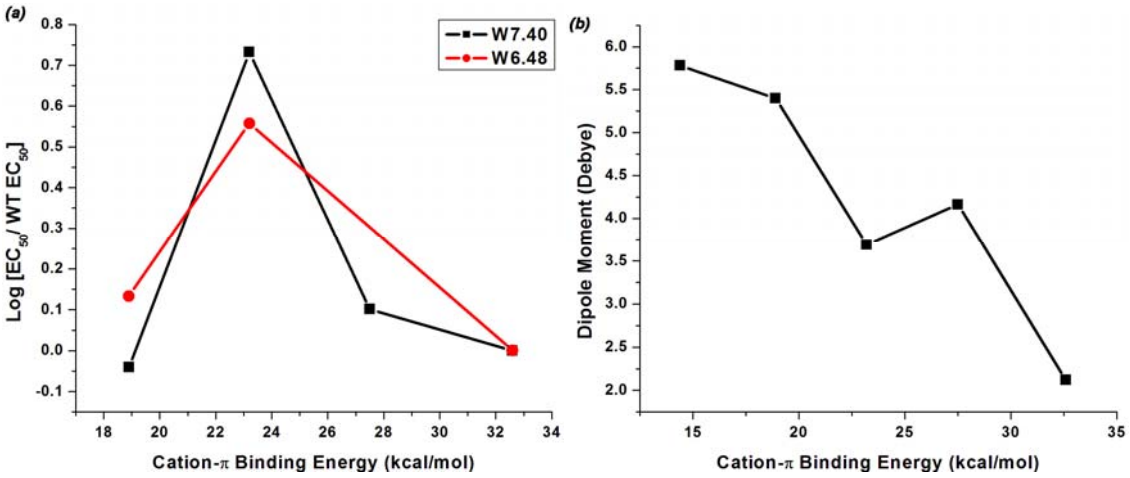


**Figure 3.26.** $F_n$Trp data analyzed in terms of cation-π binding energy and ring dipole moment. ***(a)*** Zhong Plot: calculated gas phase cation-π binding energies of fluorinated indole rings versus the log of the ratio of the $F_n$Trp $EC_{50}$ and wild-type $EC_{50}$. ***(b)*** Plot of cation-π binding energy versus dipole moment of the same indole ring

A plot of the calculated gas-phase cation-π binding energies against a measure of the change in $EC_{50}$ for $F_n$Trp mutations (a Zhong plot) at W6.48 and W7.40 does not yield the telltale linear relationship of a cation-π interaction (Figure 3.26a). We therefore

conclude that neither residue makes a conventional cation-π interaction with ACh. Also, because W3.28 failed the misacylation control experiment, we also conclude that W3.28 is not a possible site of interaction for the quaternary amine of ACh in the $M_2$AChR binding site. Previous experiments have shown that the amino acid incorporated by misacylated THG73 tRNA is Gln[79]. Therefore, a 10-fold shift in $EC_{50}$ for an effective W3.28Gln mutation is not indicative of a cation-π interaction.

What causes the $F_2$Trp shift at W6.48 and W7.40? Fluorination of the indole ring also makes other changes to the chemistry of the aromatic moiety, beyond depleting the electrostatic potential within the ring: the dipole moment of the ring is also changed through fluorination. This change in dipole moment is not uniform, but, as shown in Figure 3.26b, the relative trend is similar enough to the cation-π binding energy trend that the $F_2$Trp abnormality could not be explained by a change in indole dipole moments. Partial charge on the hydrogen of the indole nitrogen is also affected by fluorination. This change follows the cation-π trend and its magnitude is negligible.

A possible explanation for the $F_2$Trp $EC_{50}$ abnormality is that ACh makes a cation-π interaction with multiple aromatic residues. Incorporation of $F_2$Trp weakens one of these interactions. But when the weaker-binding $F_3$Trp is incorporated, the binding site readjusts and the quaternary amine of ACh makes contacts with the remaining cation-π sites, avoiding the significantly weakened binding residue. To test this hypothesis, multiple unnatural amino acids could be incorporated into the binding site[80]. If the quaternary amine of ACh makes contact with both W7.40 and W6.48, incorporation of

the fluorinated Trp series simultaneously at both residues should present the expected linear relationship between receptor response and cation-π binding energy.

### *3.3.4 Other Possible Cation-π Interaction Sites and Future $M_2$AChR Experiments*

The recent crystal structure of the $\beta_2$AR with the inverse agonist carazolol bound provides some possible sites of interest for future studies on the $M_2$AChR[31]. There are nine residues found within 5 Å of the ligand that are aromatic residues in $M_2$AChR (Figure 3.27); we have studied three of these residues in this project. Of the six remaining aromatic residues, only one, W7.35, is a Trp. Would the quaternary amine of ACh bind to a Tyr or Phe instead of a Trp, even though Trp is the stronger cation-π binder? In previous experiments on the α7 nAChR, a cation-π interaction was discovered at Tyr 93 even though the classic Trp 149 was also present[81]. So, there is precedent for such a Tyr cation-π site. In fact, a recent model of the $M_1$AChR suggested that residues Y7.39, Y6.51, and Y7.43 are in the same proximity to the quaternary amine of ACh as the aromatic box residues in the nAChR[36]. An Asn at position 7.39 in the $\beta_2$AR appears to hydrogen bond with the secondary amine of carazolol in the crystal structure[31]. Therefore, there is evidence that a Tyr in the $M_2$AChR may serve as the anchor point for the quaternary amine of ACh.

Beyond possible cation-π interactions within the $M_2$AChR binding site, there are other sites of interest (Table 3.5). Tyr residues could also be studied in terms of hydrogen bonding through the incorporation MeO-Tyr and Me-Phe. Of course, D3.32 is a site of extreme interest in aminergic GPCR research. Incorporation of a nitro amino

acid at D3.32 could assess the role of the negative charge of Asp in a much more subtle manner than Ala scanning or Asn mutants. Unfortunately, the D3.32E mutation produces a significant shift in agonist affinity for carbachol at the $M_2$AChR[82]. Therefore, nitroalanine (Noa) would be preferable over nitrohomoalanine (Nha) for studies at this position.

```
B2 107 (3.26) EFWTSIDVLC VTASIETLCV IAVDR (3.50)
M2 97         DLWLALDYVV SNASVMNLLI ISFDR

B2 184 (EL-2) CYANETCCDF FT
M2 171        VEDGECYIQF FS

B2 196 (5.35) NQAYAIASSI VSFYVPLVIM VFVYS (5.59)
M2 183        NAAVTFGTAI AAFYLPVIIM TVLYW

B2 274 (6.36) TLGIIMGTFT LCWLPFFIVN IV    (6.57)
M2 388        TILAILLAFI ITWAPYNVMV LI

B2 306 (7.33) EVYILLNWIG YVNSGFNPLI YCRS  (7.56)
M2 420        TVWTIGYWLC YINSTINPAC YALC
```

**Figure 3.27.** Alignment of $\beta_2$AR and $M_2$AChR binding site sequences. Residues within 5 Å of the ligand in the $\beta_2$AR crystal structure are shown in red. Aromatic residues not studied in this work shown in blue; the three Trp residues studied above shown in green. EL-2 members of the conserved disulfide shown in yellow on black background

N6.52 has often been proposed to hydrogen bond with the ester moiety of ACh[32,83]. This position is a Phe in the other aminergic GPCRs that bind aromatic-based agonists, but in the non-aromatic-agonist-binding $M_2$AChR this residue is an Asn. The Ala mutation at N6.52 reduces agonist potency significantly[83]. Incorporation of 2-amino-4-ketopentanoic acid (Akp) at this site would provide a negligible change in sterics, but eliminate a hydrogen-bond-donating group. Noa would also eliminate a hydrogen-bond-donating group and weaken the hydrogen-bond-accepting ability of the oxygen atom. Finally, Leu would be isosteric to Asn and Akp, but incapable of being involved in any type of hydrogen bond.

**Table 3.5.** $M_2$AChR binding site residues and mutational data

| Binding Site Residue | Literature Mutations[a] | Conclusion from Data or Possible UAA Mutations |
|---|---|---|
| **W3.28**[82] | **$M_2$AChR:** 0.3 to 5.6 fold shift in agonist affinities | W3.28dCA shows current; no cation-π |
| **D3.32**[82,84] | **$M_1$AChR:** Zero efficacy and 100-fold decrease in affinity **$M_2$AChR:** (*Glu*) 140-fold shift in carbachol affinity | Noa |
| **Y3.33**[84,85] | **$M_1$AChR:** 100-fold decrease in affinity and efficacy<br>**$M_3$AChR:** (*Phe*) 10-fold reduction in affinity and $EC_{50}$ | MeO-Phe, Me-Phe, $F_n$Phe series |
| **W6.48**[82,86] | **$M_2$AChR:** >10-fold shifts in agonist affinities<br>**$M_3$AChR:** (*Phe*) 20-fold shift in affinity | $F_n$Trp series showed no cation-π |
| **Y6.51**[85,87,88] | **$M_1$AChR:** 10-fold decrease in affinity and 100-fold decrease in $EC_{50}$<br>**$M_1$AChR:** (*Phe*) 10-fold decrease in potency<br>**$M_2$AChR:**; (*Phe*) 100-fold decrease in potency<br>**$M_3$AChR:**; (*Phe*) 10-fold decrease in potency | MeO-Phe, Me-Phe, $F_n$Phe series |
| **N6.52**[83] | **$M_1$AChR:** 10-fold decrease in potency | Akp, Noa, Leu |
| **W7.35**[89] | **$M_1$AChR:** 10-fold decrease in affinity | $F_n$Trp series |
| **Y7.39**[85,89] | **$M_1$AChR:** 100-fold decrease in affinity<br>**$M_3$AChR: (***Phe*) 10-fold decrease in potency | MeO-Phe, Me-Phe, $F_n$Phe series |
| **W7.40**[76] | **5-$HT_{2A}$:** No binding detected | $F_n$Trp series showed no cation-π |
| **Y7.43**[85] | **$M_3$AChR: (***Phe)* 10-fold decrease in affinity and 5-fold decrease in potency | MeO-Phe, Me-Phe, $F_n$Phe series |

[a]All mutations are Ala mutations and ligand studied is ACh, unless otherwise stated.

## 3.4. Materials and Methods

### *Molecular Biology*

The genes used in these experiments were in the following plasmids: $G\alpha_{oA}$ was in a pCI plasmid, GIRK1 and GIRK4 were in pBSMXT plasmids, RGS4 was in the pcDNA3.1 plasmid, and the $M_2$AChR was in the pGEM3 plasmid. Plasmids were linearized with the appropriate restriction enzymes: $G\alpha_{oA}$ was linearized with ClaI, the GIRK plasmids were linearinzed with SalI, RGS4 was linearized with StuI, and the $M_2$AChR was linearized with HindIII. mRNA was prepared by *in vitro* runoff transcription using the Ambion (Austin, TX) T7 mMessage mMachine kit for all of the constructs except for GIRK1 and GIRK4, which required the T3 kits. For unnatural amino acid mutants, the site of interest was mutated to the amber stop codon by standard means, verified by sequencing through both strands.

Typical oocyte injection volumes were 50 nL per cell; doubly injected oocytes received 50 nL injections at each injection session. Synthetic amino acids, which were conjugated to the dinucleotide dCA and ligated to truncated 74 nt tRNA as previously described[49,90], were deprotected via a 1kW xenon lamp for 5 minutes, using WG-335 and UG-11 filters to remove the NVOC group. Injection mixture concentrations were typically made such that a 1:1 combination of a mRNA mixture solution and a volume of deprotected tRNA yielded the appropriate concentrations reported above. Wild-type recovery conditions (injecting tRNA with the native amino acid) were always injected alongside mutant conditions to control for data variability. Misacylation was controlled for at every site of unnatural amino acid incorporation through the injection of 74 nt THG73 ligated to dCA (THG73-dCA)[79].

### *Electrophysiology*

Stage V–VI oocytes of *Xenopus laevis* were employed. Oocyte recordings were made in two-electrode voltage clamp mode using the OpusXpress$^{TM}$ 6000A (Axon Instruments, Union City, California). Recording buffers were ND96 (96 mM NaCl, 2 mM KCl, 1 mM $MgCl_2$, 5 mM HEPES, 1.8 mM $CaCl_2$) and high potassium ringer (96 mM NaCl, 24 mM KCl, 1 mM $MgCl_2$, 5 mM HEPES, 1.8 mM $CaCl_2$). Both recording buffers were at pH 7.5. Solution flow rates were 2 ml/min during washing and pre-washing; Drug application flow rates were 4 ml/min. Initial holding potentials were -60 mV. Data were sampled at 125 Hz and filtered at 50 Hz. The ND96 pre-wash lasted 10 s; the high potassium pre-wash lasted 50 s; drug applications were 15 s in duration; the high potassium and ND96 washings were 45 s and 90 s in duration, respectively. Acetylcholine chloride was purchased from Sigma/Aldrich/RBI. All drugs were prepared in sterile ddi water for dilution into high-potassium ringer. Dose-response relations were fitted to the Hill equation, $I_{Norm} = \frac{1}{1+\left(\frac{EC_{50}}{A}\right)^{n_H}}$, where $I_{Norm}$ is the normalized current peak at [ACh] = $A$, $EC_{50}$ is the concentration of ACh that elicits a half-maximum response, and $n_H$ is the Hill coefficient. $cEC_{50}$ values were obtained by fitting a single cell's $I_{Norm}$ data to the Hill equation, while $EC_{50}$ values were obtained by averaging the $I_{Norm}$ values for each cell at a given dose and fitting those average $I_{Norm}$ data to the Hill equation. Statistical calculations were performed using Origin 7.0 (Origin Lab, Northhampton, MA), MiniTab (MiniTab, State College, PA), or built-in functions in Excel (Microsoft).

Wild-type recovery $cEC_{50}$s from a given batch of cells were compared to previous data: the cell-to-cell CV and the batch mean $cEC_{50}$ were calculated for this comparison. This analysis was performed for each recording session to control for batch-to-batch $cEC_{50}$ variability.

The concentration of ACh test doses was approximately equal to the $EC_{50}$ (0.3 μM for W7.40Trp). In experiments where test doses were applied, they were inserted at positions in the dose series described in Figure 3.22. Most of the test dose experiments did not include a test dose #5, because it was believed to be uninformative. Our final dose-response experiments (the $F_n$Trp mutants at W7.40 and W6.48) did not include test doses.

The $C_m$ voltage ramp experiments were performed under voltage clamp conditions[91]. Data were filtered at 1 kHz and sampled at 12.5 kHz. Each ramp trace consisted of 10 ms at -60 mV, a 10 ms ramp up to +20 mV (2 V/s), a symmetric 10 ms ramp back down to -60 mV (2 V/s), and a final 10 ms at -60 mV. Five traces per cell were collected and averaged in the Clampfit 9.0 software package (Axon Instruments, Union City, California). The averaged current traces were integrated from samples 159 to 236 for $Q_A$ and 282 to 359 for $Q_B$. $C_m$ was calculated through the equation, $C_m = \frac{Q_A+Q_B}{2\Delta V}$, where $\Delta V$ is the change in potential over the integration ranges.

## 3.5 References

(1) Hopkins, A. L.; Groom, C. R. *Nat Rev Drug Discov* **2002**, *1*, 727–730.
(2) Klabunde, T.; Hessler, G. *ChemBioChem* **2002**, *3*, 928–944.

(3) Lefkowitz, R. J. *Trends in Pharmacological Sciences* **2004**, *25*, 413–422.
(4) Pierce, K. L.; Premont, R. T.; Lefkowitz, R. J. *Nat Rev Mol Cell Biol* **2002**, *3*, 639–650.
(5) Kobilka, B. K. *Biochimica et Biophysica Acta (BBA)—Biomembranes* **2007**, *1768*, 794–807.
(6) Offermanns, S. *Progress in Biophysics and Molecular Biology* **2003**, *83*, 101–130.
(7) Lefkowitz, R. J.; Shenoy, S. K. *Science* **2005**, *308*, 512–517.
(8) Hermans, E. *Pharmacology & Therapeutics* **2003**, *99*, 25–44.
(9) Bunemann, M.; Frank, M.; Lohse, M. J. *Proceedings of the National Academy of Sciences* **2003**, *100*, 16077–16082.
(10) Frank, M.; Thumer, L.; Lohse, M. J.; Bunemann, M. *J. Biol. Chem.* **2005**, *280*, 24584–24590.
(11) Gales, C.; Rebois, R. V.; Hogue, M.; Trieu, P.; Breit, A.; Hebert, T. E.; Bouvier, M. *Nat Meth* **2005**, *2*, 177–184.
(12) Lachance, M.; Ethier, N.; Wolbring, G.; Schnetkamp, P. P. M.; Hebert, T. E. *Cellular Signalling* **1999**, *11*, 523–533.
(13) Neubig, R. R.; Gantzos, R. D.; Thomsen, W. J. *Biochemistry* **1988**, *27*, 2374–2384.
(14) Tian, W. N.; Duzic, E.; Lanier, S. M.; Deth, R. C. *Mol Pharmacol* **1994**, *45*, 524–531.
(15) Ellis, C. *Nat Rev Drug Discov* **2004**, *3*, 577–626.
(16) Fotiadis, D.; Jastrzebska, B.; Philippsen, A.; Müller, D. J.; Palczewski, K.; Engel, A. *Current Opinion in Structural Biology* **2006**, *16*, 252–259.
(17) Filipek, S.; Krzysko, K. A.; Fotiadis, D.; Liang, Y.; Saperstein, D. A.; Engel, A.; Palczewski, K. *Photochemical & Photobiological Sciences* **2004**, *3*, 628–638.
(18) Janetopoulos, C.; Jin, T.; Devreotes, P. *Science* **2001**, *291*, 2408–2411.
(19) Marshall, F. H. *Current Opinion in Pharmacology* **2001**, *1*, 40–44.
(20) Violin, J. D.; Lefkowitz, R. J. *Trends in Pharmacological Sciences* **2007**, *28*, 416–422.
(21) Wei, H.; Ahn, S.; Shenoy, S. K.; Karnik, S. S.; Hunyady, L.; Luttrell, L. M.; Lefkowitz, R. J. *Proceedings of the National Academy of Sciences* **2003**, *100*, 10782–10787.
(22) Whistler, J. L.; von Zastrow, M. *Proceedings of the National Academy of Sciences* **1998**, *95*, 9914–9919.
(23) Dougherty, D. A. *Chem. Rev.* **2008**, *108*, 1642–1653.
(24) Parnot, C.; Miserey-Lenkei, S.; Bardin, S.; Corvol, P.; Clauser, E. *Trends in Endocrinology and Metabolism* **2002**, *13*, 336–343.
(25) Lu, Z.L.; Saldanha, J. W.; Hulme, E. C. *Trends in Pharmacological Sciences* **2002**, *23*, 140–146.
(26) Palczewski, K.; Kumasaka, T.; Hori, T.; Behnke, C. A.; Motoshima, H.; Fox, B. A.; Trong, I. L.; Teller, D. C.; Okada, T.; Stenkamp, R. E.; Yamamoto, M.; Miyano, M. *Science* **2000**, *289*, 739–745.
(27) Filipek, S.; Teller, D. C.; Palczewski, K.; Stenkamp, R. *Annual Review of Biophysics and Biomolecular Structure* **2003**, *32*, 375–397.
(28) Ballesteros, J. A.; Shi, L.; Javitch, J. A. *Mol Pharmacol* **2001**, *60*, 1–19.

(29) Cherezov, V.; Rosenbaum, D. M.; Hanson, M. A.; Rasmussen, S. G. F.; Thian, F. S.; Kobilka, T. S.; Choi, H.J.; Kuhn, P.; Weis, W. I.; Kobilka, B. K.; Stevens, R. C. *Science* **2007**, *318*, 1258–1265.

(30) Rasmussen, S. G. F.; Choi, H.J.; Rosenbaum, D. M.; Kobilka, T. S.; Thian, F. S.; Edwards, P. C.; Burghammer, M.; Ratnala, V. R. P.; Sanishvili, R.; Fischetti, R. F.; Schertler, G. F. X.; Weis, W. I.; Kobilka, B. K. *Nature* **2007**, *450*, 383–387.

(31) Rosenbaum, D. M.; Cherezov, V.; Hanson, M. A.; Rasmussen, S. G. F.; Thian, F. S.; Kobilka, T. S.; Choi, H.J.; Yao, X.J.; Weis, W. I.; Stevens, R. C.; Kobilka, B. K. *Science* **2007**, *318*, 1266–1273.

(32) Shi, L.; Javitch, J. A. *Annual Review of Pharmacology and Toxicology* **2002**, *42*, 437–467.

(33) Archer, E.; Maigret, B.; Escrieut, C.; Pradayrol, L.; Fourmy, D. *Trends in Pharmacological Sciences* **2003**, *24*, 36–40.

(34) Hibert, M. F.; Trumpp-Kallmeyer, S.; Bruinvels, A.; Hoflack, J. *Mol Pharmacol* **1991**, *40*, 8–15.

(35) Jöhren, K.; Höltje, H.D. *Journal of Computer-Aided Molecular Design* **2002**, *16*, 795–801.

(36) Peng, J. Y.; Vaidehi, N.; Hall, S. E.; Goddard, W. A., III. *ChemMedChem* **2006**, *1*, 878–890.

(37) Kalani, M. Y. S.; Vaidehi, N.; Hall, S. E.; Trabanino, R. J.; Freddolino, P. L.; Kalani, M. A.; Floriano, W. B.; Kam, V. W. T.; Goddard, W. A., III. *Proceedings of the National Academy of Sciences* **2004**, *101*, 3815–3820.

(38) Selent, J.; Brandt, W.; Pamperin, D.; Göber, B. *Bioorganic & Medicinal Chemistry* **2006**, *14*, 1729–1736.

(39) Vistoli, G.; Pedretti, A.; Dei, S.; Scapecchi, S.; Marconi, C.; Romanelli, M. N. *Bioorganic & Medicinal Chemistry* **2008**, *16*, 3049–3058.

(40) Jacobsen, J. *Current Topics in Medicinal Chemistry* **2002**, *2*, 343–352.

(41) Raedler, T. J.; Bymaster, F. P.; Tandon, R.; Copolov, D.; Dean, B. *Mol Psychiatry* **2006**, *12*, 232–246.

(42) Eglen, R. M.; Choppin, A.; Watson, N. *Trends in Pharmacological Sciences* **2001**, *22*, 409–414.

(43) Beene, D. L.; Brandt, G. S.; Zhong, W.; Zacharias, N. M.; Lester, H. A.; Dougherty, D. A. *Biochemistry* **2002**, *41*, 10262–10269.

(44) Beene, D. L.; Price, K. L.; Lester, H. A.; Dougherty, D. A.; Lummis, S. C. R. *J. Neurosci.* **2004**, *24*, 9097–9104.

(45) Cashin, A. L.; Petersson, E. J.; Lester, H. A.; Dougherty, D. A. *J. Am. Chem. Soc.* **2005**, *127*, 350–356.

(46) Cashin, A. L.; Torrice, M. M.; McMenimen, K. A.; Lester, H. A.; Dougherty, D. A. *Biochemistry* **2007**, *46*, 630–639.

(47) Dougherty, D. A. *Current Opinion in Chemical Biology* **2000**, *4*, 645–652.

(48) Dougherty, D. A. *J. Org. Chem.* **2008**, *73*, 3667–3673.

(49) England, P. M.; Lester, H. A.; Dougherty, D. A. *Tetrahedron Letters* **1999**, *40*, 6189–6192.

(50) England, P. M.; Zhang, Y.; Dougherty, D. A.; Lester, H. A. *Cell* **1999**, *96M1 nAChR*, 89–98.

(51) Kearney, P. C.; Nowak, M. W.; Zhong, W.; Silverman, S. K.; Lester, H. A.; Dougherty, D. A. *Mol Pharmacol* **1996**, *50*, 1401–1412.
(52) Li, L. T.; Zhong, W. G.; Zacharias, N.; Gibbs, C.; Lester, H. A.; Dougherty, D. A. *Chemistry & Biology* **2001**, *8*, 47–58.
(53) Lummis, S. C. R.; Beene, D. L.; Lee, L. W.; Lester, H. A.; Broadhurst, R. W.; Dougherty, D. A. *Nature* **2005**, *438*, 248–252.
(54) Lummis, S. C. R.; L. Beene, D.; Harrison, N. J.; Lester, H. A.; Dougherty, D. A. *Chemistry & Biology* **2005**, *12*, 993–997.
(55) McMenimen, K. A.; Petersson, E. J.; Lester, H. A.; Dougherty, D. A. *ACS Chem. Biol.* **2006**, *1*, 227–234.
(56) Mu, T. W.; Lester, H. A.; Dougherty, D. A. *J. Am. Chem. Soc.* **2003**, *125*, 6850–6851.
(57) Nowak, M. W.; Gallivan, J. P.; Silverman, S. K.; Labarca, C. G.; Dougherty, D. A.; Lester, H. A.; Conn, P. M. *Methods in Enzymology* **1998**, *293*, 504–529.
(58) Padgett, C. L.; Hanek, A. P.; Lester, H. A.; Dougherty, D. A.; Lummis, S. C. R. *J. Neurosci.* **2007**, *27*, 886–892.
(59) Petersson, E. J.; Choi, A.; Dahan, D. S.; Lester, H. A.; Dougherty, D. A. *J. Am. Chem. Soc.* **2002**, *124*, 12662–12663.
(60) Zhong, W.; Gallivan, J. P.; Zhang, Y.; Li, L.; Lester, H. A.; Dougherty, D. A. *PNAS* **1998**, *95*, 12088–12093.
(61) Ivanina, T.; Rishal, I.; Varon, D.; Mullner, C.; Frohnwieser-Steinecke, B.; Schreibmayer, W.; Dessauer, C. W.; Dascal, N. *J. Biol. Chem.* **2003**, *278*, 29174–29183.
(62) Krapivinsky, G.; Krapivinsky, L.; Wickman, K.; Clapham, D. E. *J. Biol. Chem.* **1995**, *270*, 29059–29062.
(63) Mark, M. D.; Herlitze, S. *European Journal of Biochemistry* **2000**, *267*, 5830–5836.
(64) Kofuji, P.; Davidson, N.; Lester, H. A. *Proceedings of the National Academy of Sciences* **1995**, *92*, 6542–6546.
(65) Sadja, R.; Alagem, N.; Reuveny, E. *Neuron* **2003**, *39*, 9–12.
(66) Zhang, Q. L.; Pacheco, M. A.; Doupnik, C. A. *Journal of Physiology—London* **2002**, *545*, 355–373.
(67) Dascal, N.; Schreibmayer, W.; Lim, N. F.; Wang, W.; Chavkin, C.; DiMagno, L.; Labarca, C.; Kieffer, B. L.; Gaveriaxu-Ruff, C.; Trollinger, D.; Lester, H. A.; Davidson, N. *Proceedings of the National Academy of Sciences* **1993**, *90*, 10235–10239.
(68) Sakmann, B.; Noma, A.; Trautwein, W. *Nature* **1983**, *303*, 250–253.
(69) Zhong, W. G.; Gallivan, J. P.; Zhang, Y. O.; Li, L. T.; Lester, H. A.; Dougherty, D. A. *Proceedings of the National Academy of Sciences of the United States of America* **1998**, *95*, 12088–12093.
(70) Doupnik, C. A.; Lim, N. F.; Kofuji, P.; Davidson, N.; Lester, H. A. *J. Gen. Physiol.* **1995**, *106*, 1–23.
(71) Rishal, I.; Porozov, Y.; Yakubovich, D.; Varon, D.; Dascal, N. *J. Biol. Chem.* **2005**, *280*, 16685–16694.
(72) Doupnik, C. A.; Davidson, N.; Lester, H. A.; Kofuji, P. *Proceedings of the National Academy of Sciences* **1997**, *94*, 10461–10466.

(73) Hedin, K. E.; Lim, N. F.; Clapham, D. E. *Neuron* **1996**, *16*, 423–429.
(74) Ma, J. C.; Dougherty, D. A. *Chem. Rev.* **1997**, *97*, 1303–1324.
(75) Huang, E. S. *Protein Sci* **2003**, *12*, 1360–1367.
(76) Roth, B. L.; Shoham, M.; Choudhary, M. S.; Khan, N. *Mol Pharmacol* **1997**, *52*, 259–266.
(77) Pals-Rylaarsdam, R.; Hosey, M. M. *J. Biol. Chem.* **1997**, *272*, 14152–14158.
(78) Pals-Rylaarsdam, R.; Xu, Y.; Witt-Enderby, P.; Benovic, J. L.; Hosey, M. M. *J. Biol. Chem.* **1995**, *270*, 29004–29011.
(79) Rodriguez, E. A.; Lester, H. A.; Dougherty, D. A. *RNA* **2007**, *13*, 1703–1714.
(80) Rodriguez, E. A.; Lester, H. A.; Dougherty, D. A. *Proc. Natl. Acad. Sci.* **2006**, *103*, 8650–8655.
(81) Xiu, X. California Institute of Technology, 2007.
(82) Heitz, F.; Holzwarth, J. A.; Gies, J. P.; Pruss, R. M.; Trumpp-Kallmeyer, S.; Hibert, M. F.; Guenet, C. *European Journal of Pharmacology* **1999**, *380*, 183–195.
(83) Huang, X.P.; Nagy, P. I.; Williams, F. E.; Peseckis, S. M.; Messer, W. S., Jr. *Br J Pharmacol* **1999**, *126*, 735–745.
(84) Lu, Z.L.; Hulme, E. C. *J. Biol. Chem.* **1999**, *274*, 7309–7315.
(85) Wess, J.; Gdula, D.; Brann, M. R. *Embo Journal* **1991**, *10*, 3729–3734.
(86) Wess, J.; Nanavati, S.; Vogel, Z.; Maggio, R. *Embo Journal* **1993**, *12*, 331–338.
(87) Vogel, W. K.; Sheehan, D. M.; Schimerlik, M. I. *Mol Pharmacol* **1997**, *52*, 1087–1094.
(88) Ward, S. D. C.; Curtis, C. A. M.; Hulme, E. C. *Mol Pharmacol* **1999**, *56*, 1031–1041.
(89) Matsui, H.; Lazareno, S.; Birdsall, N. J. *Mol Pharmacol* **1995**, *47*, 88–98.
(90) Nowak, M. W.; Gallivan, J. P.; Silverman, S. K.; Labarca, C. G.; Dougherty, D. A.; Lester, H. A. *Ion Channels, Pt. B* **1998**, *293*, 504–529.
(91) Schmitt, B. M.; Koepsell, H. *Biophys. J.* **2002**, *82*, 1345–1357.

# **Chapter 4:** The Use of Hydroxy Acids to Probe Structural Changes in the αM1 Helix of the Nicotinic Acetylcholine Receptor during Gating

## 4.1 Introduction

### *4.1.1 Nicotinic Acetylcholine Receptor Gating*

We discussed the incorporation of unnatural amino acids into the binding site of the nicotinic acetylcholine receptor (nAChR)—a member of the Cys-loop family of pentameric LGICs—in Chapter 2. In this chapter, we will describe an investigation of the gating mechanism of the receptor through the incorporation of hydroxy acids into a transmembrane helix of the receptor.

All members of the Cys-loop family share a similar structure that consists of a pentameric arrangement of homologous subunits around a central ion pore. Each subunit consists of a large N-terminal extracellular domain connected to a series of four transmembrane helices referred to as M1 through M4 (Figure 4.1a). Binding of a ligand to the extracellular domain causes a conformational change in the transmembrane helices that transforms the receptor from a non-conducting state into a conducting state. This molecular process is referred to as gating[1].

A model of receptor gating has been proposed through a series of cryo-EM structures of muscle-type nAChRs isolated from the *Torpedo marmorata* electric organ

(Figure 4.1b); these structures have been determined in the absence and presence of ACh[1–5]. In this model, M2, the pore lining helix, is described as a rigid helix that forms few contacts with the other three helices. L251 is part of a hydrophobic cluster of amino acids in the M2 helix that forms the gate of the channel[1,3]. This residue is referred to as 9' and we will use the X' M2 numbering throughout this chapter. By overlaying electron densities from the cryo-EM structures and the ACh binding protein (AChBP) crystal structure[6], the model suggests that during gating the β1-β2 loop of the extracellular domain rotates about 15º from its position in the closed state[5]. This structural change appears to be translated to the transmembrane helices through contacts between the β1-β2 loop and the loop that connects M2 and M3. These contacts cause M2 to rotate back into the other three helices and thus open the gate (Figure 4.1b)[3].

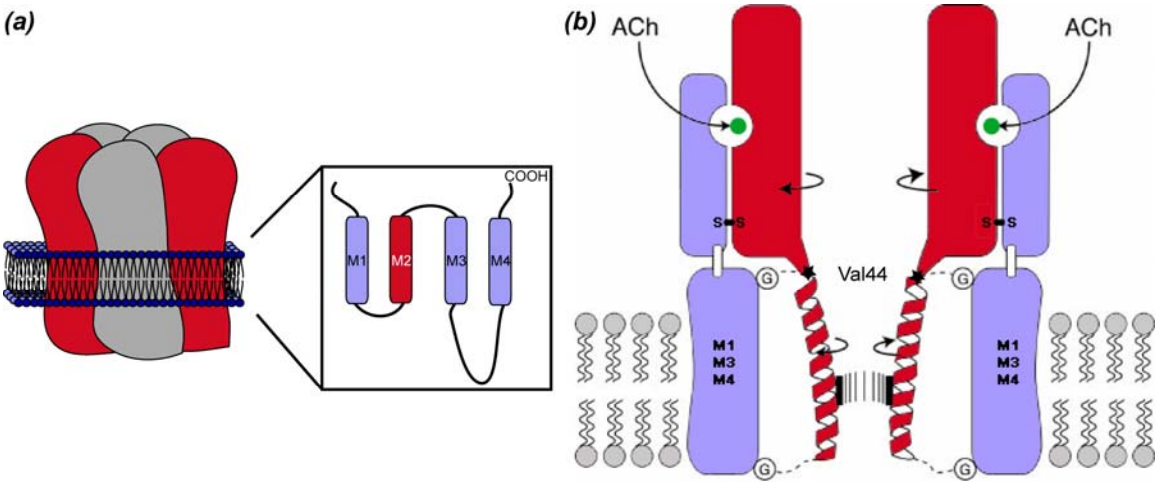


**Figure 4.1.** nAChR structure and gating model. ***(a)*** nAChR basic structure with basic transmembrane helix topology. ***(b)*** Model of gating mechanism suggested by the cryo-EM studies. A 15° rotation of the β1-β2 loop occurs upon ligand binding. Contacts between the β1-β2 loop (Val44, *star*) and the M2-M3 loop trigger the rotation of M2 away from the ion pore. ***(b)*** Adapted from Miyazawa, et al.[3].

Another model of nAChR gating has been developed through the use of substituted-cysteine accessibility method (SCAM) studies of the transmembrane helices[7–12]. SCAM determines the water accessibility of a given protein residue through labeling

with methanethiosulfonate (MTS) derived small molecules (Figure 4.2a). A residue is said to be labeled if, after MTS application, the response of the receptor to ACh is altered[8]. By applying MTS probes both extracellularly and intracellularly, the degree of reactivity of residues along M1 and M2 has been measured to find the location of the nAChR gate[10,11]. According to these data, the gate of the nAChR is located at the intracellular end of M2, between residues Gly240 and Thr2' (Figure 4.2b). Changes in MTS reactivity also suggest that the M2 helix transitions from a disrupted α-helical structure to an uninterrupted α-helix. This secondary structural rearrangement in the 8' to 10' region of M2 is proposed as an alternative gating mechanism[10,11]. Analysis of the M1 helix with SCAM reveals that in the closed state the extracellular end of M1 lines the pore, but in the open state it is blocked by M2[7].

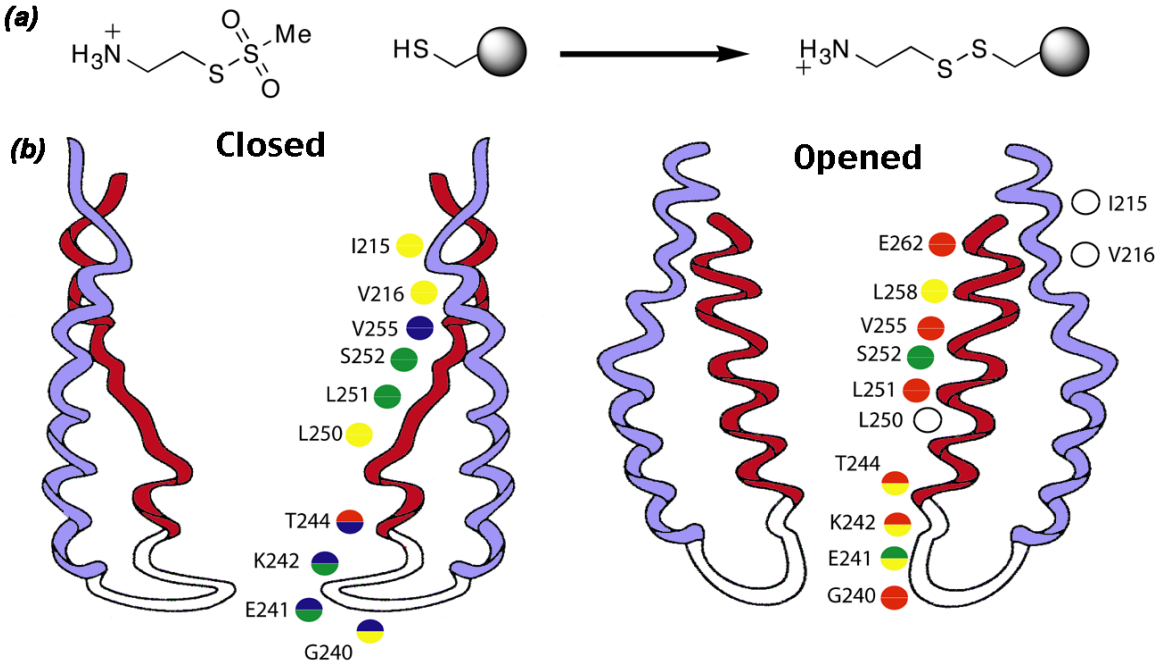


**Figure 4.2.** nAChR SCAM studies. ***(a)*** Scheme of SCAM methodology. ***(b)*** SCAM data for M1 and M2 helices. Residue reactivity is indicated by the half-circle color: high reactivity shown in red, low reactivity shown in blue. Top half of the circle represents reactivity to extracellularly applied MTS probe, while the bottom half corresponds to intracellular reactivity. Empty circle represents a non-reactive residue. L251 is L9'. M1 and M2 helices colored as in Figure 4.1. Adapted from Wilson, G.G., and Karlin, A.[10,11]

### *4.1.2 Use of Hydroxy Acid Scanning to Study Receptor Gating*

Previous studies from this lab have also probed the transmembrane region in an attempt to elucidate the gating mechanism. These past studies have focused on hydrogen bonding within the transmembrane helices. Hydrogen bonding plays a crucial role in the secondary structure of proteins. Much of this hydrogen bonding occurs between the amide backbone moieties of the protein. In a standard α-helix, a given residue, *i*, in the helix donates a hydrogen bond through an amide NH to the carbonyl of residue *i* – 4; the same residue accepts a hydrogen bond through its carbonyl oxygen from the amide NH of residue *i* + 4[13]. These backbone hydrogen bonds form or break during the structural rearrangements involved in establishing or unraveling an α-helix.

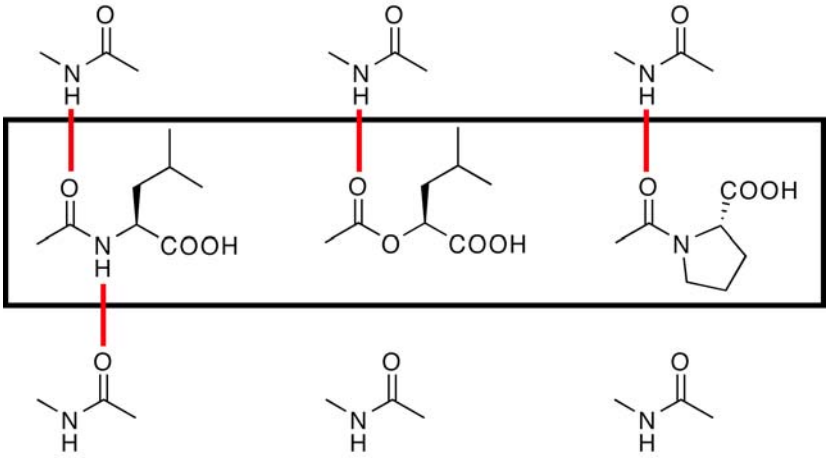


**Figure 4.3.** Comparison of backbone hydrogen bonding. Shown from left to right are Leu, leucic acid (Lah), and Pro. Lah and Pro cannot donate a hydrogen bond.

Backbone hydrogen bonds can be disrupted through conventional and non-native mutations. The natural amino acid Pro disrupts backbone hydrogen bonding because the tertiary amide group of Pro cannot donate a hydrogen bond (Figure 4.3)[14]. Hydroxy acid analogs of natural amino acids can also disrupt backbone hydrogen bonding.

Incorporation of a hydroxy acid into a protein results in the formation of an ester backbone, instead of an amide backbone (Figure 4.3)[15–18]. An ester backbone disrupts hydrogen bonding through two different mechanisms. Unlike amides, esters lack a hydrogen-bond-donating moiety (Figure 4.3). The dipole moment of an ester carbonyl is also significantly reduced compared to an amide carbonyl (the difference in dipole moment between formic acid and formamide is greater than 2 Debye[19]); the ester carbonyl, therefore, is also a weaker hydrogen bond acceptor. Several groups have determined the net destabilization caused by the incorporation of an ester backbone into an α-helix to be between 1.7[15,18] and 2.9 kcal/mol[20].

Our previous studies utilized the destabilizing nature of these ester linkages to map regions of the nAChR transmembrane helices that undergo structural changes during gating[17,21]. Hydroxy acids inserted into positions that do not change hydrogen bonding status during gating will not cause a change in $EC_{50}$, because both closed and open states will be equally destabilized. But hydroxy acids inserted into positions that undergo a secondary structural change will alter dose-response relationships because of the change in hydrogen bonding status. This shift would correspond to the formation or destruction of a hydrogen bond in the gating transition[17,21].

This methodology was used to study structural changes in the M2 helix of the α subunit (αM2) during gating[17]. Valic acid (Vah) and leucic acid (Lah)—the hydroxy acid analogs of Val and Leu, respectively (Figure 4.4a)—were incorporated into positions along the αM2 helix. It was observed that the largest shifts in $EC_{50}$ occurred in the extracellular half of the helix (11'+; Figure 4.4b). The four major shifts to lower $EC_{50}$s (22', 19', 16', and 13') occurred with an $i + 3$ periodicity.

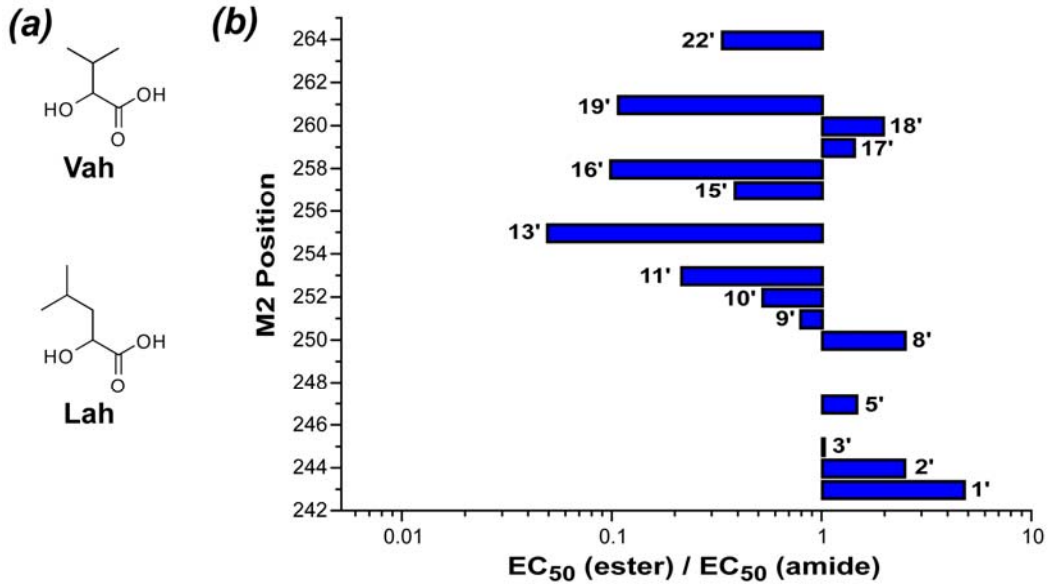


**Figure 4.4.** αM2 hydroxy acid data. ***(a)*** Structures of valic acid (Vah) and leucic acid (Lah). ***(b)*** Data from hydroxy acid scanning of the αM2 helix. Ratio of the hydroxy acid mutant $EC_{50}$ to that of the corresponding amino acid shown for each residue. Data reported previously[17]

The helical periodicity of these data supports the SCAM model of nAChR gating[11]. These two data sets suggest that portions of the M2 helix undergo secondary structure changes during gating and that the helix does not act as a rigid helix. The SCAM model predicts a significant structural rearrangement in the residues from 8' to 10'; the positions most affected by hydroxy acid mutagenesis were found N-terminal to the 11' residue. Linear-free energy relationship (LFER) analysis of the δM2 helix mutants also suggest that the N-terminal half of the M2 helix undergoes structural changes independent of the C-terminal half[22–24].

### *4.1.3 Project Goals*

To further understand the structural changes that occur in the transmembrane helices of the nAChR during the gating transition, hydroxy acids were incorporated into the αM1

helix. A previous study using hydroxy acid incorporation determined that the conserved P221 in the αM1 helix plays a crucial role in nAChR gating[17]. Conventional mutants at P221 in the α subunit produced non-functional receptors. Incorporation of Lah, Vah, and the hydroxy acid analog of Ala (Aah) at αP221, however, produced functional receptors. These observations suggest that the disruption of the αM1 helix hydrogen bonding network caused by αP221 is required for nAChR gating. αP221 may act as a hinge in the αM1 helix, separating the two halves of the helix and allowing them to act independently during gating.

## 4.2 Results

**Table 4.1** Hydroxy acid mutation data[a]

| M1 Position | $EC_{50}$ | $n_H$ | N |
|---|---|---|---|
| **L212 (24")** | 49 ± 4 | 1.2 ± 0.1 | 3 |
| **F214 (22")** | 44 ± 1 | 1.5 ± 0.04 | 4 |
| **V216 (20")** | 43 ± 2 | 1.3 ± 0.1 | 3 |
| **L223 (13")** | 130 ± 10 | 1.5 ± 0.1 | 5 |
| **L224 (12")** | 62 ± 3 | 1.3 ± 0.1 | 3 |
| **F225 (11")** | 1.5 ± 0.04 | 2.7 ± 0.2 | 5 |
| **S226 (10")** | 2.8 ± 0.1 | 1.8 ± 0.1 | 4 |
| **F227 (9")** | 130 ± 10 | 1.4 ± 0.1 | 6 |
| **L228 (8")** | 150 ± 20 | 1.4 ± 0.2 | 3 |
| **V232 (4")[b]** | 47 | 1.6 | |

[a] $EC_{50}$ (μM) and $n_H$ ± SEM
[b] Data for V232 was collected by Ben Jones.

Following the procedure of the previous hydroxy acid experiments, the hydroxy acid Vah (Figure 4.4a) was incorporated into several positions along the αM1 helix. Dose-response relationships were obtained for each Vah mutant (Table 4.1), and the resulting $EC_{50}$ values were compared to the wild-type value. A cluster of αM1 positions

exhibited shifted $EC_{50}$s for the hydroxy acid mutations (Figure 4.5). (We created an αM1 numbering scheme referenced from F225. This residue is at the same register as L11' of αM2; we therefore set F225 as 11". The order of numbering parallels that of αM1: numbers increase intracellular to extracellular. This scheme is shown in Figure 4.5.) Shifts in $EC_{50}$ values were observed at positions 8", 9", 10", 11", and 13".

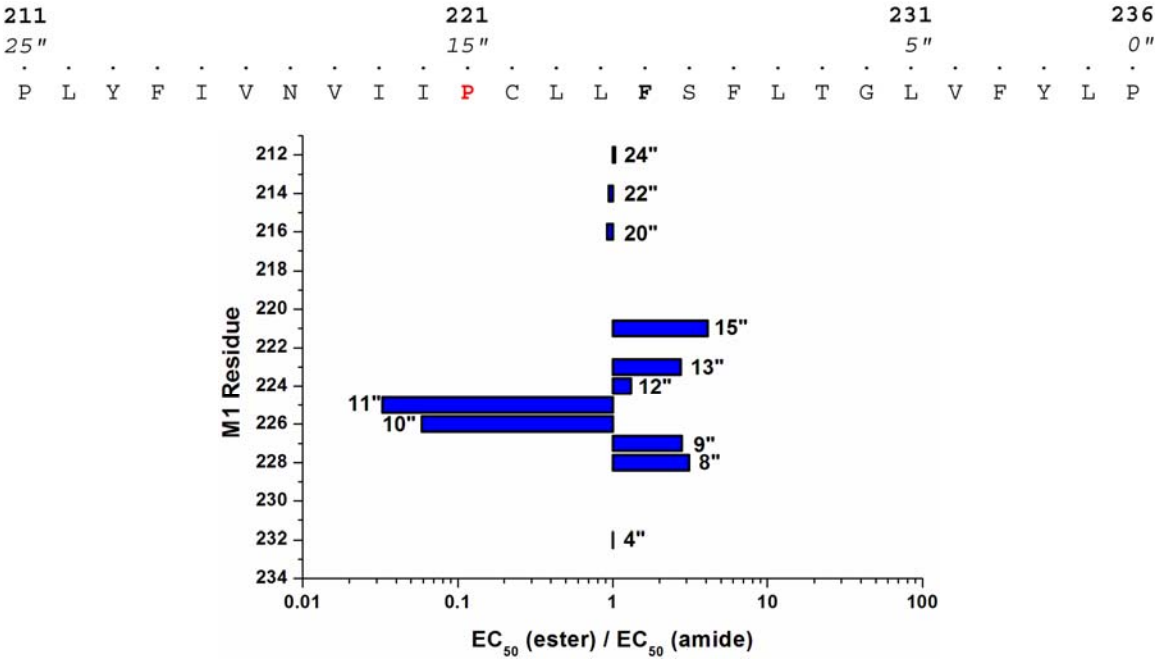


**Figure 4.5.** αM1 hydroxy acid data. *Top*: αM1 numbering scheme. P221(15") shown in red. Reference F225(11") shown in bold. *Bottom*: M1 hydroxy acid scanning data from Table 4.1. The amide $EC_{50}$ used was the wild-type nAChR $EC_{50}$ (47 μM). P15" data previously reported[17]

## 4.3 Discussion

The pattern of hydroxy acid $EC_{50}$ shifts in αM1 has two possible explanations. The division between the affected and unaffected residues in αM1 is P15" (P221). These data support the hypothesis that αP221 acts as a hinge in the αM1 helix and allows the extracellular and intracellular halves of αM1 to act independently. Significant shifts in

$EC_{50}$ values observed in the αM2 study were extracellular to 13', while the αM1 data showed significant shifts on the intracellular side of 15". The similarity in helix position for these divisions suggests that gating involves structural changes along the extracellular half of αM2 that are then translated over to the intracellular half of αM1 at αP15".

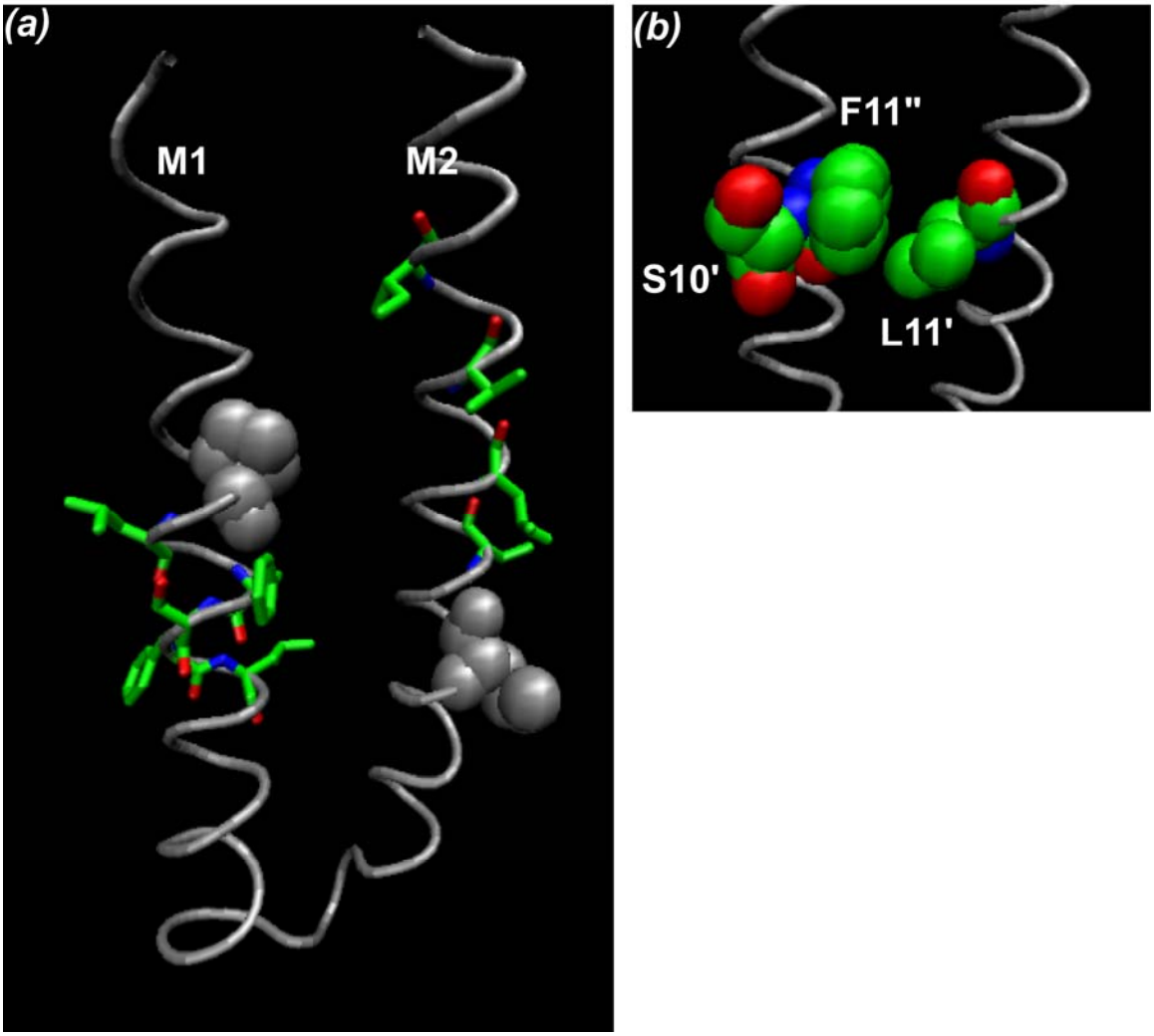


**Figure 4.6.** Cryo-EM structures of αM1 and αM2 helices studied with hydroxy acids. ***(a)*** Residues identified from hydroxy acid scanning experiments as sites of structural changes in the gating process shown as sticks. L9' and P15" shown as space-filling. ***(b)*** Interaction between F11" and L11'. S10" also shown. Both images from 2BG9 pdb[25]

Another possible explanation for the pattern in observed $EC_{50}$ shifts may not originate from the backbone mutations we made, but instead from changes in the side

chains. The two most significant $EC_{50}$ shifts (> 10-fold reduction) were observed at F11" and S10". In two recent studies, F11" has been shown to interact with L11' of αM2[26,27] (Figure 4.6b). Although the two helices do not make substantial contact, these two residues are proximal in the most recent cryo-EM structure[25]. Double-mutant analysis of single-channel data for the F11"L and L11'F mutants shows an interaction energy of -1.2 kcal/mol[27]. When F11" was mutated to amino acids with smaller side chains, the mean open times and $P_{open}$ both increased; a decrease in the channel closing rate was deemed responsible[26]. Decreasing bulk at this αM1 position appears to weaken a crucial interaction with αM2 that may stabilize the closed state of the receptor. Because our F11"Vah mutation decreased bulk at this position, it is possible that the lower $EC_{50}$ value we observed was caused by disrupting this important αM1-αM2 interaction. The side chain of S10" is in contact with F11" in the most recent cryo-EM structure and may help position the Phe side chain for this F11"-L11' interaction. The 10-fold reduction in $EC_{50}$ for the S10"Vah mutant may have been caused by adversely affecting this positioning of F11".

## 4.4 Materials and Methods

### *Molecular Biology*

All experiments performed utilized the following procedure for the preparation of mRNA and aminoacyl tRNA, as has been described previously[28]. The α, β, γ, δ nAChR subunit genes were in pAMV plasmids. To transcribe mRNA for each protein, the plasmids were linearized with NotI. mRNA transcriptions were run using Ambion T7

mMessage mMachine kits for all constructs. Unprotected hydroxy acid-dCA molecules were ligated onto THG73 74 nt tRNA using T4 RNA ligase.

### *Electrophysiology*

Stage V–VI *Xenopus* oocytes were isolated and injected with mRNA and aminoacyl-tRNA as described above. Injection volumes were 50 nL for each oocyte. Oocytes were recorded in ND96 $Ca^{2+}$-free buffer (96 mM NaCl, 2 mM KCl, 1 mM $MgCl_2$, 5 mM HEPES) at pH 7.5.

Oocyte recordings were made 48 h post-injection in two-electrode voltage clamp mode using the OpusXpress$^{TM}$ 6000A (Axon Instruments, Union City, CA). Oocytes were superfused with $Ca^{2+}$-free ND96 solution at flow rates of 1 mL/min before drug application, 4 mL/min during application, and 3 mL/min during wash. Holding potentials were -60 mV. Data were sampled at 125 Hz and filtered at 50 Hz. Drug applications were 15 s in duration. Acetylcholine chloride was purchased from Sigma/Aldrich/RBI and prepared in sterile ddi water prior to dilution into calcium-free ND96. Dose-response relationships were fitted to the Hill equation to determine $EC_{50}$ and Hill coefficient values.

## 4.5 References

(1) Unwin, N. *Journal of Molecular Biology* **1993**, *229*, 1101–1124.
(2) Brejc, K.; van Dijk, W. J.; Klaassen, R. V.; Schuurmans, M.; van der Oost, J.; Smit, A. B.; Sixma, T. K. *Nature* **2001**, *411*, 269–276.
(3) Miyazawa, A.; Fujiyoshi, Y.; Unwin, N. *Nature* **2003**, *423*, 949–955.

(4) Unwin, N. *Nature* **1995**, *373*, 37–43.
(5) Unwin, N.; Miyazawa, A.; Li, J.; Fujiyoshi, Y. *Journal of Molecular Biology* **2002**, *319*, 1165–1176.
(6) Smit, A. B.; Syed, N. I.; Schaap, D.; van Minnen, J.; Klumperman, J.; Kits, K. S.; Lodder, H.; van der Schors, R. C.; van Elk, R.; Sorgedrager, B.; Brejc, K.; Sixma, T. K.; Geraerts, W. P. M. *Nature* **2001**, *411*, 261–268.
(7) Akabas, M. H.; Karlin, A. *Biochemistry* **1995**, *34*, 12496–12500.
(8) Akabas, M. H.; Kaufmann, C.; Archdeacon, P.; Karlin, A. *Neuron* **1994**, *13*, 919–927.
(9) Karlin, A.; Akabas, M. H. *Neuron* **1995**, *15*, 1231–1244.
(10) Wilson, G. G.; Karlin, A. *Neuron* **1998**, *20*, 1269–1281.
(11) Wilson, G. G.; Karlin, A. *Proceedings of the National Academy of Sciences of the United States of America* **2001**, *98*, 1241–1248.
(12) Yu, Y.; Shi, L.; Karlin, A. *Proceedings of the National Academy of Sciences of the United States of America* **2003**, *100*, 3907–3912.
(13) Branden, C.; Tooze, J. *Introduction to Protein Structure*, 2nd ed. Garland Publishing, Inc.: New York, NY, 1999.
(14) Cordes, F. S.; Bright, J. N.; Sansom, M. S. P. *Journal of Molecular Biology* **2002**, *323*, 951–960.
(15) Chapman, E.; Thorson, J. S.; Schultz, P. G. *J. Am. Chem. Soc.* **1997**, *119*, 7151–7152.
(16) Ellman, J. A.; Mendel, D.; Schultz, P. G. *Science* **1992**, *255*, 197–200.
(17) England, P. M.; Zhang, Y.; Dougherty, D. A.; Lester, H. A. *Cell* **1999**, *96M1 nAChR*, 89–98.
(18) Koh, J. T.; Cornish, V. W.; Schultz, P. G. *Biochemistry* **1997**, *36*, 11314–11322.
(19) Nelson, R. D.; Lide, D. R.; Maryott, A. A. *Selected Values of Electric Dipole Moments for Molecules in the Gas Phase*, 71st ed. CRC Press: Boca Raton, FL, 1990.
(20) Beligere, G. S.; Dawson, P. E. *J. Am. Chem. Soc.* **2000**, *122*, 12079–12082.
(21) Dang, H.; England, P. M.; Farivar, S. S.; Dougherty, D. A.; Lester, H. A. *Mol. Pharmacol.* **2000**, *57*, 1114–1122.
(22) Auerbach, A. *Sci. STKE* **2003**, *2003*, re11.
(23) Cymes, G. D.; Grosman, C.; Auerbach, A. *Biochemistry* **2002**, *41*, 5548–5555.
(24) Grosman, C.; Zhou, M.; Auerbach, A. *Nature* **2000**, *403*, 773–776.
(25) Unwin, N. *Journal of Molecular Biology* **2005**, *346*, 967–989.
(26) Spitzmaul, G.; Corradi, J.; Bouzat, C. *Molecular Membrane Biology* **2004**, *21*, 39–50.
(27) Corradi, J.; Spitzmaul, G.; De Rosa, M. J.; Costabel, M.; Bouzat, C. *Biophys. J.* **2007**, *92*, 76–86.
(28) Nowak, M. W.; Gallivan, J. P.; Silverman, S. K.; Labarca, C. G.; Dougherty, D. A.; Lester, H. A.; Conn, P. M. *Methods in Enzymology* **1998**, *293*, 504–529.

# **Appendix A:** The Synthesis of Nitro Amino Acids: Nitroalanine and Nitrohomoalanine

## A.1 Introduction

For our study of the conserved Asp, D89, in the nicotinic acetylcholine receptor (nAChR), we wished to study the role of the residue's negative charge in receptor function[1]. Also, we had hoped to study the conserved binding site residue, D3.32, in the aminergic class of G-protein-coupled receptors (GPCRs). This Asp has been suggested to form an electrostatic interaction with positively charged monoamine ligands[2–5]. We therefore decided to synthesize unnatural amino acids that could subtly probe the contribution of the negative charge of Asp or Glu to receptor structure and function.

The nitro group provides a neutral analog to the carboxylate group that is isosteric and isoelectronic (Figure 2.5). As described in Chapter 2, D89N mutations not only neutralize side-chain charge, but also introduce an electrostatic clash through the amide moiety. Another researcher in our group has previously synthesized the keto analog to Asp, 2-amino-4-ketopentanoic acid (Akp)[6], and we have shown in Chapter 2 that this amino acid relieves the electrostatic clash caused by Asn. But Akp destroys the symmetry of Asp, which may disrupt the hydrogen bonding network of the native residue. A nitro analog of Asp would neutralize the negative charge while maintaining the side chain's symmetry and avoiding steric clashes. A significant difference between

the nitro group and the carboxylate is the substantially weaker hydrogen-bond-accepting ability of the nitro group (energetic differences are between 1.5 and 2.0 kcal/mol)[7].

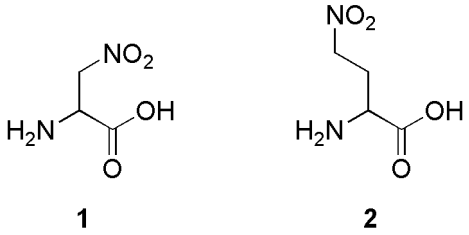


**1** **2**

**Figure A.1.** Structures of nitroalanine (**1**) and nitrohomoalanine (**2**)

This appendix describes the synthesis of nitroalanine (Noa) and nitrohomoalanine (Nha; Figure A.1). While Nha could be synthesized and adapted to our nonsense suppression methodology, Noa was incompatible with a crucial transformation.

## A.2 Results and Discussion

### *A.2.1 Noa Synthesis*

To synthesize Noa, we used a literature procedure (Figure A.2, ***i*** through ***iii***) that began with a fully protected glycine (**3**)[8,9]. Boc-2-bromoglycine *tert*-butyl ester (**4**) was synthesized from **3** through photobromination. After reaction of **4** with methyl nitronate and acid deprotection, we were able to produce Noa (**1**). The standard NVOC protection of the free amine was performed without issue.

But when we attempted to synthesize the NVOC-nitroalanine cyanomethyl ester (**8b)**, we mainly produced NVOC-dehydroalanine cyanomethyl ester (**8a**). This side product was the result of deprotonation at the $\alpha$ carbon and elimination of the nitro group to yield the $\alpha, \beta$ unsaturated amino acid. Some of the desired cyanomethyl ester was

produced, but we were unable to separate it from **8a** through flash chromatography; we believed that the compound degraded while on the column. Attempts at running the cyanomethyl reaction with weaker bases, such as $Na_2CO_3$[10], also produced dehydroalanine.

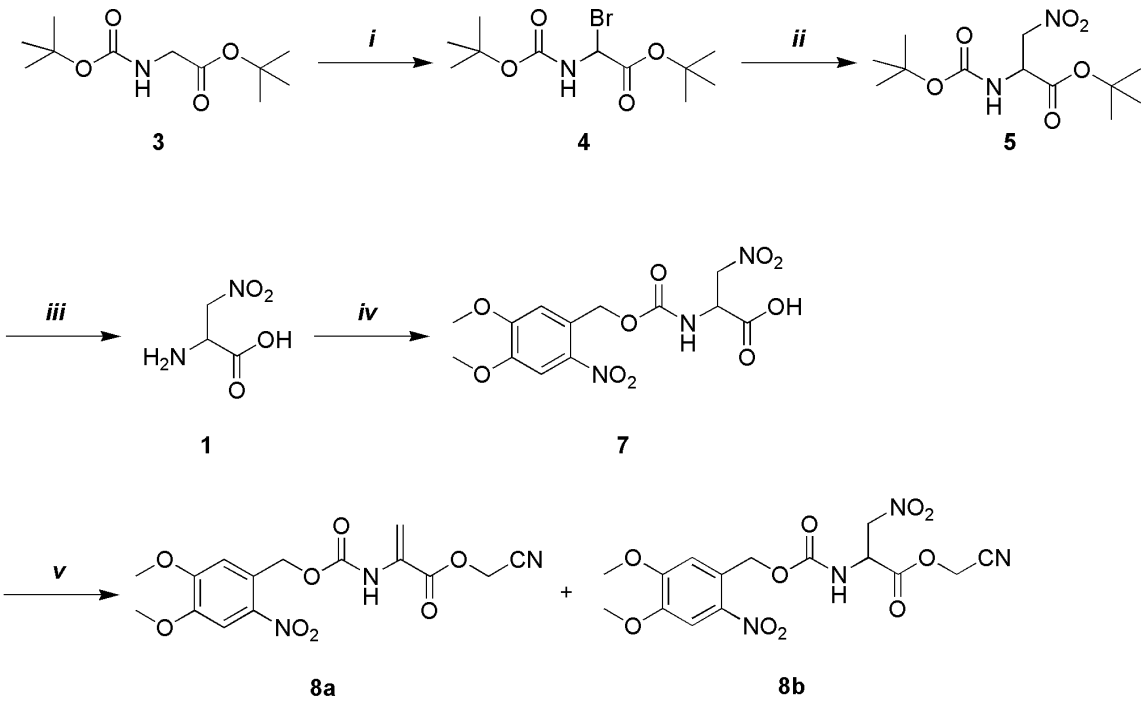


**Figure A.2.** Synthetic route for the attempted synthesis of NVOC-nitroalanine cyanomethyl ester. ***i***: *N*-bromosuccinimide, *hv*. ***ii***: *n*-BuLi, $CH_3NO_2$, THF, HMPA. ***Iii***: 1:1 TFA / $CH_2Cl_2$. ***iv***: NVOC-Cl, 2 eq. $Na_2CO_3$, 1:1 $H_2O$/dioxanes. ***v***: 2 eq. $Et_3N$, $ClCH_2CN$; or 2 eq. $Na_2CO_3$, 2 eq. $ClCH_2CN$, DMSO

The elimination of the nitro group in Noa may be unavoidable when transforming the free amino acid into a form that is compatible with dCA coupling. β-nitro amino acids have been synthesized as a facile route to dehydro amino acids in synthetic peptides[8,9]. Because dehydro amino acids are not stable enough for solid-phase peptide synthesis, β-nitro amino acids are incorporated into the peptide and subsequent treatment of the full peptide with base eliminates the nitro group, yielding the dehydro amino acid.

Basic conditions during the cyanomethyl ester formation step and the dCA coupling procedure may prevent us from incorporating Noa through standard means.

One alternative route could involve oxidation of the primary amine of 2,3-diaminopropionic acid (Dap) to a nitro group. Early in our attempts to synthesize Noa, we investigated the zirconium alkoxide catalyzed oxidation of primary amines[11–13]. This transformation could be performed on the cyanomethyl ester of Dap to produce the cyanomethyl ester of Noa. Of course, if the nitro group is eliminated by dCA coupling conditions, this route will also not be viable. Any attempt to revisit the Noa synthesis should begin with submitting **5** to dCA coupling conditions to determine how stable the $NO_2$ group is during coupling.

### *A.2.2 Nha Synthesis*

Unlike Noa, Nha was found to be adaptable to both cyanomethyl ester formation and dCA coupling procedures. The synthesis of Nha (Figure A.3) began with the reaction of a nucleophilic protected glycine (**10**) with nitroethylene (**9**) following a literature procedure[14,15]. Nitroethylene was prepared from 2-nitroethanol following a literature preparation[16]. Deprotection of the protected Nha (**11**) by acid yielded the free amino acid (**2**). Standard NVOC protection and cyanomethyl ester formation procedures were used to produce **14**. dCA-Nha was formed using our standard method.

As an aside, Nha could also be synthesized from dehydroalanine. Reaction of methyl nitronate with protected dehydroalanine has been shown to yield Nha[17]. Because

the distillation of nitroethylene is cumbersome (see A.3 for details), this route may serve as an easier means to synthesize Nha.

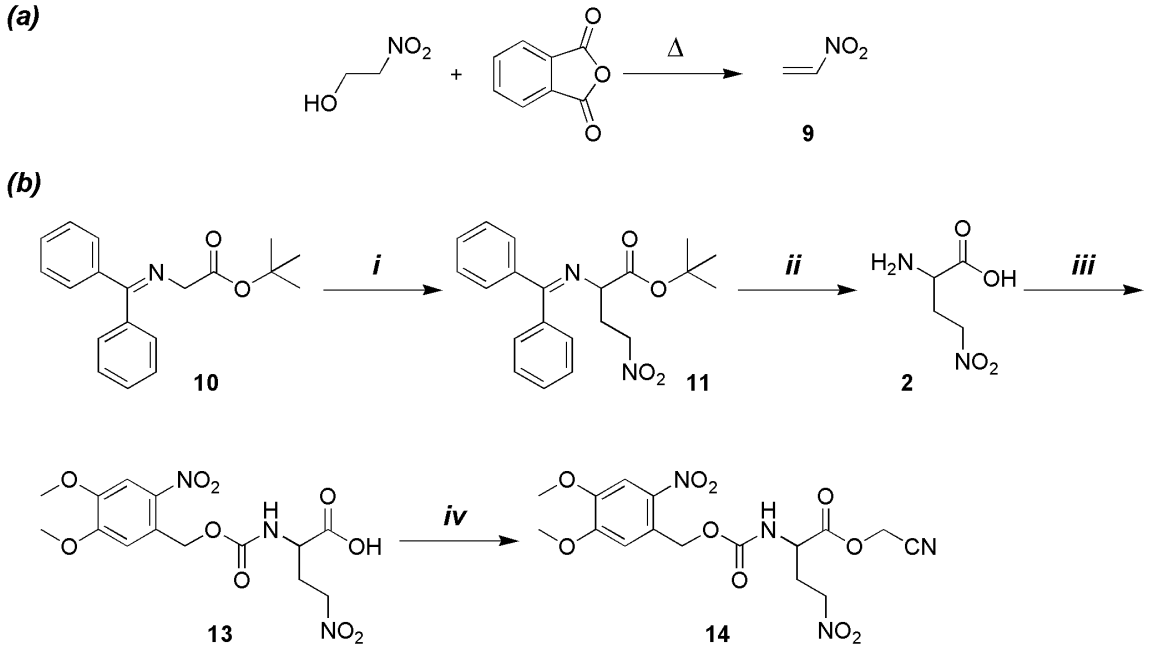


**Figure A.3.** Synthesis of NVOC-nitrohomoalanine cyanomethyl ester. ***(a)*** Preparation of nitroethylene. ***(b)*** Synthetic route for the synthesis of nitrohomoalanine. ***i***: 1) 1 eq. LDA, THF; 2) nitroethylene, THF. ***ii*****:** 1 N HCl. ***iii***: NVOC-Cl, 2 eq. $Na_2CO_3$, 1:1 $H_2O$/dioxanes. ***iv***: 2 eq. $Et_3N$, $ClCH_2CN$

## A.3 Materials and Methods

### *Synthesis of N-Boc-2-Bromoglycine t-Butyl ester (4)*

A solution of *N*-Boc-glycine *tert*-Butyl ester (**3**; 463 mg, 2 mmol) and *N*-bromosuccinimide (356 mg, 2 mmol) in 23 mL of dry $CCl_4$ was stirred for 1 h in front of a 1 kW xenon lamp without the WG-335 and UG-11 filters (without the filters, there was greater than 75% transmission for wavelengths greater than 250 nm). The solution was then filtered and evaporated to yellow crystals that were stored under Ar at 4ºC. $^1$H-NMR ($CDCl_3$) δ 1.52 (s, 9H), 5.92 (d, 1H), 6.24 (d, 1H).

*Synthesis of N-Boc-Nitroalanine tert-Butyl ester (**5**)*

Nitromethane (216 μL, 4mmol) was stirred with 20 mL THF and 4 mL HMPA at -78ºC under Ar. *n*-BuLi (1.6 mL of a 2.5 M solution in hexanes, 4 mmol) was added dropwise to the nitromethane solution to produce the methyl nitronate. A solution of **4** (618 mg, 2 mmol) in 2 mL THF was added dropwise to the reaction mixture and allowed to stir for 4 h at -78ºC. The reaction was then quenched with 3 mL of acetic acid and the reaction flask was allowed to warm to room temperature. After dilution of the reaction mixture with 25 mL of ethyl acetate, three washes with brine, and drying over $Na_2SO_4$, the solution was evaporated to a solid. Crude product was purified on a flash silica column using a 5:1 hexanes / ethyl acetate solvent system to yield 330 mg of pure product (57% yield). $^1$H-NMR ($CDCl_3$) δ 1.46 (s, 9H), 1.50 (s, 9H), 4.6 (m, 1H), 4.78 (m, 1H), 4.92 (m, 1H), 5.47 (d, 1H).

*Synthesis of Nitroalanine (**1**)*

*N*-Boc-nitroalanine *tert*-butyl ester (330 mg, 1.14 mmol) was dissolved in a 1:1 solution of TFA and dichloromethane (15 mL each). After 1 h, the solution was evaporated to dryness to yield 245 mg of **1**. Product was taken onto the next step without characterization.

*Synthesis of NVOC-Nitroalanine (**7**)*

Nitroalanine (245 mg, 0.99 mmol) and $Na_2CO_3$ (212 mg, 2 mmol) were dissolved in water (20 mL). To this solution, NVOC-Cl (300 mg, 1.09 mmol) in dioxane (20 mL) was added and stirred for 4 h at room temperature. The reaction was evaporated to half of the reaction volume and then diluted with 40 mL of water. The solution was extracted with ether (40 mL) until the organic layer was no longer colored. The aqueous layer was acidified with HCl to a pH of ~ 2 (solution became cloudy) and extracted with dichloromethane until organic layer was clear. The organic layers were dried and evaporated to yield 194 mg of **7** (52%). $^1$H-NMR ($CDCl_3$) δ 3.97 (s, 1H), 4.01 (s, 1H), 4.88 (m, 1H), 4.94 (m, 1H), 5.07 (m, 1H), 5.59 (s, 2H), 5.90 (d, 1H), 6.98 (s, 1H), 7.74 (s, 1H). ES-MS calculated for $C_{13}H_{15}N_3O_{10}$: 373.08, found *m/z* $(M+Na)^+$: 395.8. Crude product was taken on directly to the next step.

*Attempted Synthesis of NVOC-Nitroalanine Cyanomethyl Ester (**8b**)*

$Et_3N$ (35.1 μL, 0.25 mmol) was added to a solution of **7** (90 mg, 0.25 mmol) in neat chloroacetonitrile. The mixture was stirred for 4 h and evaporated to dryness. Flash silica chromatography was used to try to separate the desired product (**8b**) from the side product (**8a**) with a 1:1 hexanes / ethyl acetate solvent system. Purification attempts never yielded pure **8b**, possibly due to degradation to **8a**. $^1$H-NMR ($CDCl_3$) for **8a** δ 3.98 (s, 3H), 4.01 (s, 3H), 4.89 (s, 2H), 5.60 (s, 2H), 5.95 (m, 1H), 6.44 (s, 1H), 7.01 (s, 1H), 7.74 (s, 1H). ES-MS calculated for **8a** $C_{15}H_{15}N_3O_8$: 365.3, found *m/z* $(M+Na)^+$: 388,

$(M+K)^+$: 404. ES-MS calculated for **8b** $C_{15}H_{16}N_4O_{10}$: 412/3, found *m/z* $(M+Na)^+$: 434.8, $(M+K)^+$: 450.8.

An alternative procedure using a weaker base involved combining **7** (80 mg, 0.2 mmol), $Na_2CO_3$ (50 mg, 0.5 mmol), and chloroacetonitrile (36 μL, 0.5 mmol) in 5 mL of dry DMSO. The solution was stirred under Ar overnight. The reaction was diluted with 5 mL ethyl acetate and then washed twice with water and twice with brine. Similar ES-MS data found for **8a** and **8b**.

### *Preparation of Nitroethylene (**9**)*

2-Nitroethanol (5 mL, 70 mmol) and phthalic anhydride (15.6 g, 105 mmol) were mixed in a distillation setup. As the mixture was heated, the pressure of the distillation setup was kept at 80 mmHg with a VWR automatic vacuum controller (1600B-01). The mixture became a homogeneous yellow liquid at 120ºC; the color changed to orange at 140ºC; the last color change to dark red occurred at 150ºC. Phthalic anhydride would sublimate into the distillation set-up before large amounts of product could be distilled. Often product would be found in the cold finger between the distillation set-up and the vacuum controller. **9** was collected and stored as a 0.8M solution in THF. $^1$H-NMR ($CDCl_3$) δ 5.90 (d, J = 6.3 Hz, 1H), 6.61 (dd, J = 15 and 2 Hz, 1H), 7.11 (m, J = 15 and 8 Hz, 1H).

*Synthesis of 2-Diphenylmethyleneimino-4-nitro-butanoate tert-Butyl ester (**11**)*

Lithium diisopropylamide (6.8 mL of a 0.5 M solution in THF, 3.4 mmol) was added to a solution of *N*-diphenylmethyleneglycine *tert*-butyl ester (1 g, 3.4 mmol) in THF (6.8 mL) at -78°C. After 1 h, nitroethylene (4.25 mL 0.8 M in THF, 3.4 mmol) was added to the mixture and stirred for an additional 1 h. The reaction mixture was then brought to room temperature and a 1:1 mixture of ethyl acetate and water (20 mL) was added. The organic layer was separated, washed with brine, dried ($Mg_2SO_4$), and evaporated. The crude product was purified on a flash silica column using a 1:1 ethyl acetate and hexane solvent system to yield 690 mg of pure product (53%): $^1$H-NMR ($CDCl_3$) δ 1.44 (s, 9H), 2.58 (m, 2H), 4.08 (t, 1H), 4.53 (m, 2H), 7.20 (m, 2H), 7.36 (m, 3H), 7.47 (m, 3H), 7.67 (m, 2H). ES-MS calculated mass for $C_{21}H_{24}N_2O_4$: 368.17, found *m/z* ($M+H^+$): 369.0, ($M+Na^+$): 390.8, ($M+K^+$): 407.0.

*Synthesis of Nitrohomoalanine (**2**)*

2-Diphenylmethyleneimino-4-nitrobutanoate t-Butyl ester was deprotected by addition of 1 N HCl and stirring of the mixture for 15 h at room temperature. The reaction mixture was lyophilized and taken onto the next reaction.

*Synthesis of NVOC-Nitrohomoalanine (**13**)*

Nitrohomoalanine (230 mg, 0.6 mmol) and $Na_2CO_3$ (132 mg, 1.2 mmol) were dissolved in water (10 mL). To this solution was added NVOC-Cl (171 mg, 0.6 mmol) in

dioxane (10 mL), and the mixture was stirred for 4 h at room temperature. The reaction mixture was evaporated to half of the reaction volume and then diluted with 20 mL of water. The solution was extracted with ether (20 mL) until the organic layer was no longer colored. The aqueous layer was acidified with HCl to a pH of ~ 2 (solution became cloudy) and extracted with dichloromethane until the organic layer was clear. The organic layers were dried and evaporated to yield 209 mg of NVOC-nitrohomoalanine (90%); ES-MS calculated for $C_{14}H_{17}N_3O_{10}$: 387.09, found *m/z* ($M-H^-$): 387.0. Crude product was taken on directly to the next step.

### *Synthesis of NVOC-Nitrohomoalanine Cyanomethyl Ester (**14**)*

NVOC-nitrohomoalanine (50 mg, 0.13 mmol) was dissolved in 5 mL of $ClCH_2CN$. $Et_3N$ (18.3 μL, 0.13 mmol) was added and the solution was stirred under Ar for 4 h. The reaction mixture was evaporated and purified on a flash silica column with a 1:1 mixture of ethyl acetate and hexanes to yield 40 mg of product (72%). $^1H$ NMR (CDCl3) δ 2.95 (m, 2H), 3.18 (m, 2H), 3.96 (s, 3H), 4.02 (s, 3H), 4.33 (m, 1H), 4.96 (d, 2H), 5.56 (d, 2H), 5.72 (d, 1H), 6.91 (s, 1H), 7.72 (s, 1H). ES-MS calculated for $C_{16}H_{18}N_4O_{10}$: 426.10, found *m/z* ($M+Na^+$): 449.0, ($M+K^+$): 465.0.

### *Synthesis of Nha-dCA*

NVOC-nitrohomoalanine cyanomethyl ester (10 mg, 2.3 μmol) was dissolved in 0.5 mL of dry DMF. The dinucleotide dCA was added (10 mg, 8.4 μmol) and the

mixture was stirred under Ar overnight. The reaction mixture was purified by reverse phase HPLC. ES-MS calculated for $C_{33}H_{38}N_{11}O_{22}P_2$: 1005.9, Found *m/z* ($M-H^-$): 1004.2.

## A.4 References


(1) Cashin, A. L.; Torrice, M. M.; McMenimen, K. A.; Lester, H. A.; Dougherty, D. A. *Biochemistry* **2007**, *46*, 630–639.

(2) Heitz, F.; Holzwarth, J. A.; Gies, J. P.; Pruss, R. M.; Trumpp-Kallmeyer, S.; Hibert, M. F.; Guenet, C. *European Journal of Pharmacology* **1999**, *380*, 183–195.

(3) Huang, E. S. *Protein Sci*. **2003**, *12*, 1360–1367.

(4) Lu, Z.-L.; Hulme, E. C. *J. Biol. Chem.* **1999**, *274*, 7309–7315.

(5) Shi, L.; Javitch, J. A. *Annual Review of Pharmacology and Toxicology* **2002**, *42*, 437–467.

(6) Mu, T. California Institute of Technology, 2006.

(7) Kelly, T. R., Kim, M.H. *Journal of the American Chemical Society* **1994**, *116*, 7072–7080.

(8) Burgess, V. A.; Easton, C. J. *Australian Journal of Chemistry* **1988**, *41*, 1063–1070.

(9) Coghlan, P. A.; Easton, C. J. *Tetrahedron Letters* **1999**, *40*, 4745–4748.

(10) Byers, J. H.; Baran, R. C.; Craig, M. E.; Jackman, J. T. *Organic Preparations and Procedures International* **1991**, *23*, 373–374.

(11) Krohn, K. *Synthesis-Stuttgart* **1997**, 1115–1127.

(12) Krohn, K.; Küpke, J. *European Journal of Organic Chemistry* **1998**, *1998*, 679–682.

(13) Thiel, W. R.; Krohn, K. *Chemistry—A European Journal* **2002**, *8*, 1049–1058.

(14) Rowley, M.; Leeson, P. D.; Williams, B. J.; Moore, K. W.; Baker, R. *Tetrahedron* **1992**, *48*, 3557–3570.

(15) Vanderwerf, A.; Kellogg, R. M. *Tetrahedron Letters* **1991**, *32*, 3727–3730.

(16) Ranganathan, D., Rao, B., Ranganathan, S., Mehrotra, A.K., Iyengar, R. *Journal of Organic Chemistry* **1980**, *45*, 1185–1189.

(17) Crossley, M. J.; Fung, Y. M.; Potter, J. J.; Stamford, A. W. *Journal of the Chemical Society—Perkin Transactions 1* **1998**, 1113–1121.

# **Appendix B:** Assessing the Statistical Significance of Shifts in Cell $EC_{50}$ Data with Varying Coefficients of Variation

## B.1 Introduction

Because of the high levels of variability in cell $EC_{50}$ ($cEC_{50}$) data observed in $M_2$AChR experiments, we wondered what magnitude of shifts in mean $cEC_{50}$ between wild-type and mutant experiments could be interpreted as significant. This appendix describes our attempt to address this concern. We reformatted the student's *t*-test in terms of cell-to-cell variability and mean $cEC_{50}$ shift magnitude. With this equation, we then assessed our ability to differentiate $cEC_{50}$ data sets with high levels of variability.

## B.2 Methodology

### *B.2.1 Definitions and Assumptions*

We first assumed that the sets of $cEC_{50}$ data being analyzed do not have significant batch-to-batch variability in mean or standard deviation. Because the purpose of this exercise was to assess how increasing cell-to-cell variability affects our ability to differentiate shifts in mean $cEC_{50}$, we wished to avoid considering data that fluctuates in multiple ways. Also, we assumed that both wild-type and mutant data sets have the same level of variability. Through our past work with LGICs and our observations of GPCR

data, we have observed that the variations of $cEC_{50}$ data for wild-type and mutant conditions are often similar (as examples see Figure 3.12 and Figure 3.20).

The student's *t*-test assumes that the data sets being compared are both normally distributed. We have found that $cEC_{50}$ data are not normally distributed, but fit a log-normal distribution. A data set, $X_i$, is said to be log-normally distributed if the transformation of the data set, $\ln X_i$, is normally distributed. For example, the Shapiro-Wilk test for normality rejects the conventional wild-type $M_2$AChR data set as being normal ($W = 0.91$ and $p = 0.001$), but fails to reject the ln transformed data ($W = 0.96$ and $p = 0.1$). (Some data sets, such as the 10.10.0 W7.40F3Trp data set, fit both normal and log-normal distributions.) Type I error (false positive) rates—the probability of concluding two data sets are different statistically when, in reality, they are not—deviate above the standard $\alpha = 0.05$ level for log-normally distributed data sets that have unequal variances in the ln transformed data set. But if ln transformed data sets have equal variances, type I error rates return to acceptable levels[1]. We assume that because our hypothetical data sets have equal variation, they will also have equal variation when transformed into $\ln X_i$ data. A rigorous proof of this assumption has not been performed.

We have chosen to define the cell-to-cell variability of a given data set of $cEC_{50}$ values as the ratio of the population standard deviation to the population mean, or the coefficient of variation (CV). The CV allowed us to compare the variability of different data sets with substantially different means and, thus, different magnitudes of absolute standard deviation. In our derivation, we expressed differences in mean $cEC_{50}$ between mutant and wild-type data sets as a z-fold shift, where the mutant mean $cEC_{50}$ is z times

the wild-type mean $cEC_{50}$. What follows is the derivation of the independent two-sample *t*-test in terms of CV, z, and the number of wild-type and mutant cells.

### *B.2.2 Derivation*

Let $\mu_{mut} = \frac{\sum_i^n x_i}{n}$ be the mean $cEC_{50}$ for a mutant cell population, where $x_i$ is the $cEC_{50}$ from mutant cell, $i$, and $n$ is the number of mutant cells.

Let $\mu_{wt} = \frac{\sum_i^n y_i}{m}$ be the mean $cEC_{50}$ for a wild-type cell population, where $y_i$ is the $cEC_{50}$ from wild-type cell, $i$, and $m$ is the number of wild-type cells.

Let $s_{mut}$ be the standard deviation of $cEC_{50}$s for a mutant cell population.

Let $s_{wt}$ be the standard deviation of $cEC_{50}$s for a wild-type cell population.

$CV = \frac{s_{mut}}{\mu_{mut}} = \frac{s_{wt}}{\mu_{wt}}$ is the coefficient of variance for both mutant and wild-type cell populations.

$s_{mut}^2 = (s_{mut})^2$; $s_{wt}^2 = (s_{wt})^2$ are the variances for the mutant and wild-type cell populations, respectively.

$df = n + m - 2$ is the degrees of freedom.

For independent two-sample *t*-tests,

$t = \frac{\mu_{mut} - \mu_{wt}}{s_{\mu_{mut} - \mu_{wt}}}$, where $s_{\mu_{mut} - \mu_{wt}} = \sqrt{\left(\frac{(n-1)s_{mut}^2 + (m-1)s_{wt}^2}{n+m-2}\right)\left(\frac{1}{n} + \frac{1}{m}\right)}$.

By substituting $s_{mut}^2 = (s_{mut})^2 = (\mu_{mut}CV)^2$ and $s_{wt}^2 = (s_{wt})^2 = (\mu_{wt}CV)^2$,

$$t = \frac{\mu_{mut}-\mu_{wt}}{\sqrt{\left(\frac{(n-1)(\mu_{mut}CV)^2+(m-1)(\mu_{wt}CV)^2}{n+m-2}\right)\left(\frac{1}{n}+\frac{1}{m}\right)}} = \frac{\mu_{mut}-\mu_{wt}}{CV\sqrt{\left(\frac{(n-1)\mu_{mut}{}^2+(m-1)\mu_{wt}{}^2}{n+m-2}\right)\left(\frac{1}{n}+\frac{1}{m}\right)}}.$$

For a $z$-fold shift, let $\mu_{mut} = z\mu_{wt}$ ,

$$t = \frac{z\mu_{wt}-\mu_{wt}}{CV\sqrt{\left(\frac{(n-1)(z\mu_{wt})^2+(m-1)\mu_{wt}{}^2}{n+m-2}\right)\left(\frac{1}{n}+\frac{1}{m}\right)}} = \frac{(z-1)\mu_{wt}}{CV\mu_{wt}\sqrt{\left(\frac{(n-1)z^2+(m-1)}{n+m-2}\right)\left(\frac{1}{n}+\frac{1}{m}\right)}} =$$

$$\frac{(z-1)}{CV\sqrt{\left(\frac{(n-1)z^2+(m-1)}{n+m-2}\right)\left(\frac{1}{n}+\frac{1}{m}\right)}} .$$

## B.3 Results and Discussion

To understand the effect of CV on the statistical significance of z-fold shifts in mean $cEC_{50}$ data, we utilized the above-derived equation for *t* and performed two numeric analyses. The derived equation was coded into an Excel (Microsoft) worksheet and the *t*-distribution *p* values were calculated using the TDIST function of the software. Confidence levels described below are calculated by the equation, $CL = 100(1-p)$.

In the first analysis, we considered the *t*-test confidence level of z-fold shifts in mean $cEC_{50}$ for an experiment with 10 wild-type and 5 mutant cells. These quantities are typical for a LGIC experiment. We examined CV values of 0.25, 0.5, and 1.0 because these levels of variation were observed in our LGIC and GPCR data sets (see Figure 3.12 and Figure 3.17). Figure B.1 shows the relationship between z-fold shift and confidence level in differentiating the two $cEC_{50}$ means by the *t*-test. Confidence levels exceeded the standard 95% threshold for CV = 0.25 at z = 1.33, CV = 0.5 at z = 1.76, and CV = 1.0 at

z = 3.5. Traditionally, we do not try to physically interpret z < 3 shifts. Therefore, even in the most variable data sets we have observed, interpreting physically relevant $EC_{50}$ shifts would not be problematic for data sets containing 10 wild-type and 5 mutant cells.

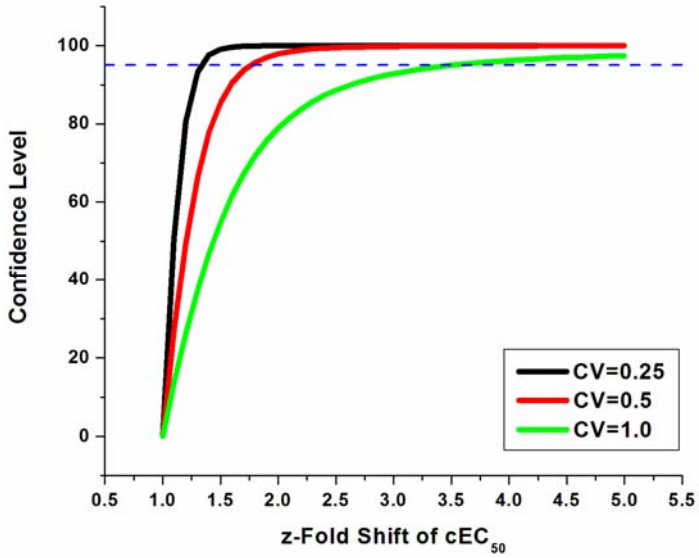


**Figure B.1.** The confidence levels of *t*-tests comparing $cEC_{50}$ means with z-fold shifts. Three CV values were considered: 0.25, 0.5, and 1.0. The dotted blue line denotes the standard 95% confidence level

The goal of our second analysis was to understand how increasing the number of cells in the data sets affected *t*-test confidence levels. We considered 3-fold mean $cEC_{50}$ shifts, the minimal shift we would want to interpret physically. Relationships between CV and confidence levels were determined for experiments with 10 wild-type and 5 mutant cells, 12 wild-type and 12 mutant cells, and 20 wild-type and 10 mutant cells (Figure B.2). The highest possible CV at which the confidence level of differentiating a 3-fold shift exceeded the 95% level increased with the number of cells in each data set. CVs below 0.91, 1.06, and 1.33 were sufficient to pass the 95% confidence level for the 10 wild-type / 5 mutant, 12 wild-type / 12 mutant, and 20 wild-type / 10 mutant cell cases, respectively. We therefore concluded that the ability to differentiate small $EC_{50}$

shifts between data sets with higher than normal cell-to-cell variability could be improved by collecting additional data.

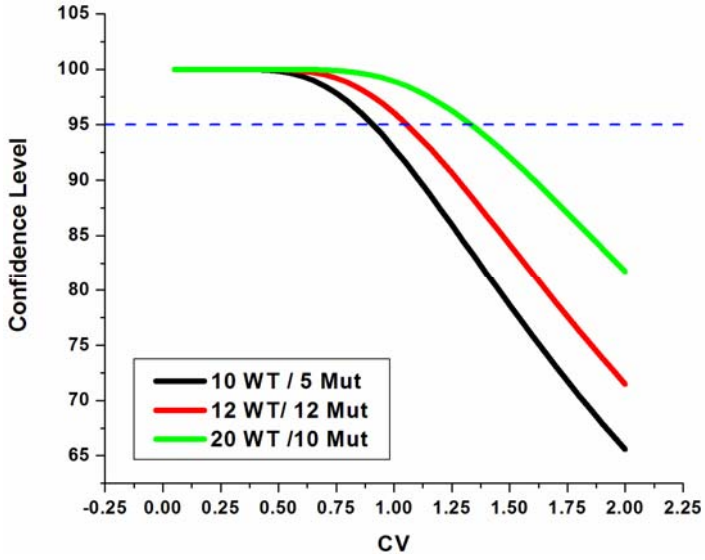


**Figure B.2.** The effect of sample sizes on discerning 3-fold shifts in mean $cEC_{50}$ using the *t*-test. The dotted blue line denotes the standard 95% confidence level.

As discussed in Section 3.2.6, we assume that significant shifts in $cEC_{50}$s produce significant shifts in $EC_{50}$. Therefore, these exercises suggest that cell-to-cell variability at levels we observed in $M_2$AChR data will not hinder our ability to interpret $EC_{50}$ shifts that we have been accustomed to in LGIC experiments. Collecting more cells per condition will allow us to strengthen the statistical significance of small $EC_{50}$ shifts. We therefore concluded that batch-to-batch variability was the real concern in GPCR data, not cell-to-cell variability.

## B.4 References

(1) Zhou, X.-H.; Gao, S.; Hui, S. L. *Biometrics* **1997**, *53*, 1129–1135.

# **Appendix C:** Simulation of $M_2$AChR Dose-Response Relationship Data Using an Asymmetric Current Change Model

## C.1 Introduction

To try to understand the source of the variability in suppressed $M_2$AChR $cEC_{50}$ data, we performed an experiment in which we repeated the same concentration of ACh (0.3 μM) at various intervals throughout a dose-response experiment (see Figure 3.22). Current responses to the same dose of agonist increased on average throughout the course of the experiments. More importantly, this change was not constant: current changes appeared to be low at the early doses in the series, but increased at the half-way point of the series.

What effect does asymmetric current change have on a dose-response relationship? Figure C.1 provides an illustration of the effect. Before we fit our data to the Hill equation, we normalize $I_{K,ACh}$ measurements (Figure C.1a) to the maximum value in the dose series. This maximum response is often found in the last two doses of the series. Our interpretation of the current change data suggests that this maximum response is higher than what it would be absent any current change mechanism. Therefore, the other $I_{K,ACh}$ values would appear to be smaller relative to this maximum dose than they would without the current changes. In other words, the normalized responses for the current change data would be smaller at each dose, effectively shifting the $cEC_{50}$ to higher values (Figure C1b).

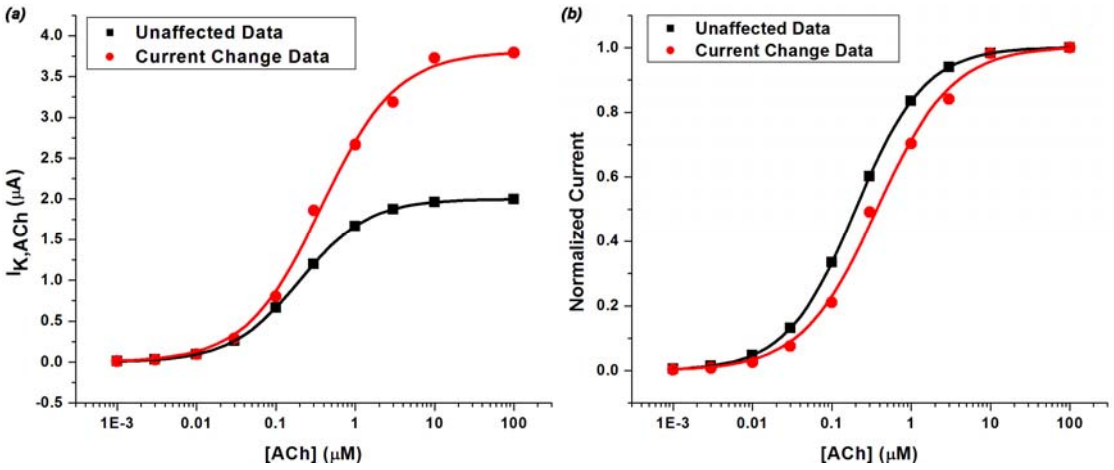


**Figure C.1.** Example of how asymmetric current changes can affect dose-response relationships. ***(a)*** $I_{K,ACh}$ data for an unaffected cell and a cell that experiences asymmetric current changes. The affected data were derived from the unaffected data by applying a set of current change values ($\alpha$) used in the data simulation exercises. ***(b)*** Both data sets from ***(a)*** are normalized and fit to the Hill equation. The unaffected data has a $cEC_{50}$ value of 200 nM, while the current change $cEC_{50}$ value is 370 nM.

Once we realized the effect these current changes could produce in our $cEC_{50}$ data, we wanted to determine if we could use the current change data we had collected to simulate dose-response data. Would this simulated $cEC_{50}$ data exhibit variability similar to the actual data we had collected? This appendix describes the method we used to simulate 10.10.0 W7.40Trp data and how this generated data set matched real data.

## C.2 Methodology

We decided to try to simulate 10.10.0 W7.40Trp data because it employed the experimental conditions that we had used to generate the current change data and was the largest suppression data set (N = 42). Our goal was to generate five different sets of N = 42 cell dose-response relationships and then compare each set to the actual data for differences in mean (*t*-test) and variance (F-test). The actual 10.10.0 W7.40Trp data had

a mean of 230 nM and a standard deviation of 120 nM (CV = 0.52; the ln transformed data set had a mean of 5.3 and a standard deviation of 0.5).

### *C.2.1 Mathematical Model for Simulating $M_2$AChR Data*

Let $Y_n = \{Y_1, Y_2, \dots, Y_{10}\}$ be an ideal set of dose-response data, where $Y_n$ refers to the $I_{K,ACh}$ measurement at dose $n$ of the dose-response series.

Let $X_n = \{X_1, X_2, \dots, X_{10}\}$ be the normalized $Y_n$ data set such that $Y_n = \beta X_n$, where $\beta$ is the maximum current of $Y_n$ or max($Y_n$).

Let $Z_n = \{Z_1, Z_2, \dots, Z_{10}\}$ be the set of current data that has been modified through asymmetric current changes such that $Z_n = Y_n(1 + \alpha_n)$, where $\alpha_n = \{\alpha_1, \alpha_2, \dots, \alpha_{10}\}$ is the set of percent changes in current relative to dose $n = 1$ of the dose-response series ($\alpha_1 = 0$).

Let $W_n = \{W_1, W_2, \dots, W_{10}\}$ be the normalized $Z_n$ data such that $W_n = \frac{Z_n}{\max(Z_n)}$.

As $Y_n = \beta X_n$ and $Z_n = Y_n(1 + \alpha_n)$, $Z_n = \beta X_n(1 + \alpha_n)$.

Therefore, $W_n = \frac{Z_n}{\max(Z_n)} = \frac{\beta X_n(1+\alpha_n)}{\max(\beta X_n(1+\alpha_n))}$.

Because $\beta$ is a positive coefficient, $\max(\beta X_n(1 + \alpha_n)) = \beta \max(X_n(1 + \alpha_n))$.

In the end, $W_n = \frac{X_n(1+\alpha_n)}{\max(X_n(1+\alpha_n))}$.

### *C.2.2 Implementation of the Mathematical Model*

The above derivation provided us with an equation for normalized simulated data ($W_n$) expressed in terms of ideal normalized data ($X_n$) and a set of current changes at each dose in a dose-response series ($\alpha_n$). Ideal normalized data were generated by evaluating the Hill equation at the ten doses used in our dose-response experiments (0.001, 0.003, 0.01, 0.03, 0.1, 0.3, 1, 3, 10, and 100 μM) using a seed $EC_{50}$ and $n_H$.

To generate sets of α values, we utilized the current change data set we had obtained from the 10.10.0 W7.40Trp experiments. In those experiments, we measured the change in current of a test dose of ACh at three positions within the dose-response series, thus obtaining sets of α values. (For the purpose of these simulations, we numbered the test doses as follows: the test dose between 0.01 μM and 0.03 μM was numbered as n = 3.5, the test dose at 0.3 μM as n = 6, and the test dose between 3 μM and 10 μM as n = 8.5. This numbering system allowed us to refer to the ten doses within the dose-response series as n = 1 through n = 10.) Our proposed current change model consisted of linear progressions connecting the three measured α values (Figure C.2). At dose n =1, α = 0 and α values increased linearly through dose n = 2 and n = 3 towards the α value measured for n = 3.5. Similar progressions were created to connect n = 3.5 with n = 6 and n = 6 with n = 8.5. At doses n = 9 and n = 10, we set α at the value measured for n = 8.5.

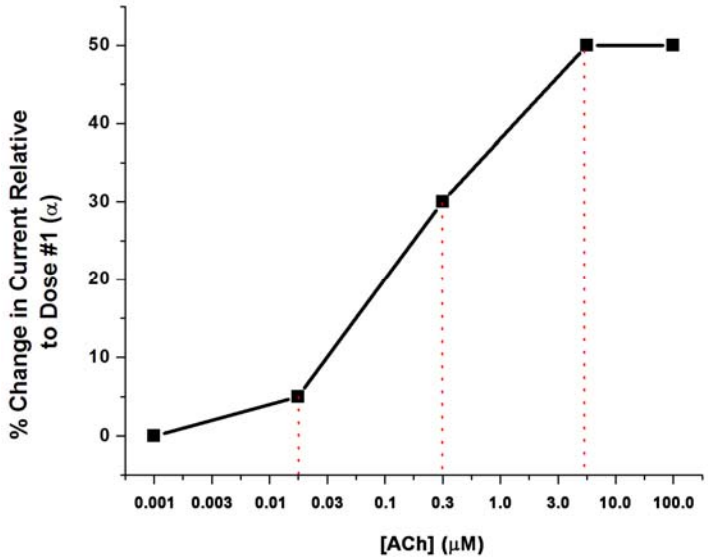


**Figure C.2.** Model for progression of α values throughout a dose-response relationship series. Dotted red lines denote the data points for α values measured during the current change experiments described in Section 3.2.6.3 and above. We refer to these data points as doses n = 3.5, n = 6, and n = 8.5, where the 0.001 μM dose is n = 1 and the 100 μM dose is n = 10.

With this model of current change, we then randomly generated α values for n = 3.5, n = 6, and n = 8.5. To generate these values (#1, #2, and #3) we randomly sampled from three data sets using the MiniTab software package: #1 was generated from the set of n = 3.5 current change percentages, #2 was generated from the set of differences between n = 6 and n = 3.5 percentages, and #3 was generated from the set of differences between n = 8.5 and n = 6 percentages. α values for n = 6 and n = 8.5 were then produced by adding the randomly generated #2 to #1 and adding randomly generated #3 to the previous sum (#1 + #2), respectively. This method for randomly generating values at n = 6 and n = 8.5 was used to provide the context of current change observed in the cells to our generated numbers.

Once n = 3.5, n = 6, and n = 8.5 α values were obtained, the rest of the α values were determined by linear progressions between them as described above (Figure C.2). An Excel (Microsoft) spreadsheet was used to program the equations that described the

lines connecting n = 1 with n = 3.5, n = 3.5 with n = 6, and n = 6 with n = 8.5. Figure C.3 shows the mean of generated α values at each dose for the five sets of 42 dose-response relationships compared with the actual measurements at n = 3.5, n = 6, and n = 8.5.

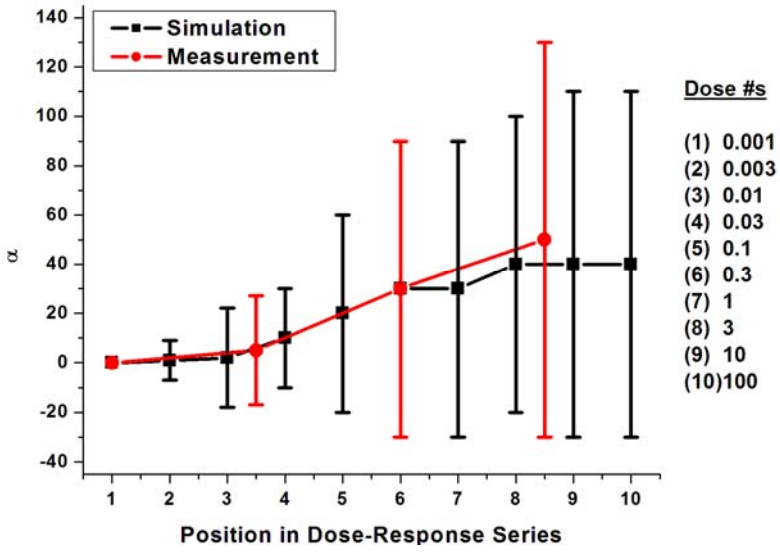


**Figure C.3.** Comparison of measured and randomly generated α values. The measured α values (red) were only determined at doses n = 3.5, n = 6, and n = 8.5. Randomly generated α values (black) were used in the five sets of 42 simulated dose-response relationships; these values were generated from the measured data as described in the text. *Right*: The ACh concentrations for each numbered dose

### *C.2.3. Seed $EC_{50}$ Value and Dose-Response Relationship Data Generation*

After five sets of 42 α value progressions were created, we took one set, Rand1, and used it to determine the appropriate seed $EC_{50}$ value. We sought a seed value that generated dose-response data with a mean $cEC_{50}$ value similar to that of the actual data. We tested seed values of 200, 190, 170, 160, 150, 140, and 135 nM and plotted the mean of the resulting $cEC_{50}$s versus the seed value (Figure C.4a). Because $cEC_{50}$ data is log-normally distributed, we made a similar plot for the mean $cEC_{50}$ of the ln transformed simulated data (Figure C.4b). Using the linear equations from both plots, we solved for

the seed value that would produce the mean $cEC_{50}$ of the actual data (230 nM or 5.3, for the ln transformed data). Both equations yielded 140 nM.

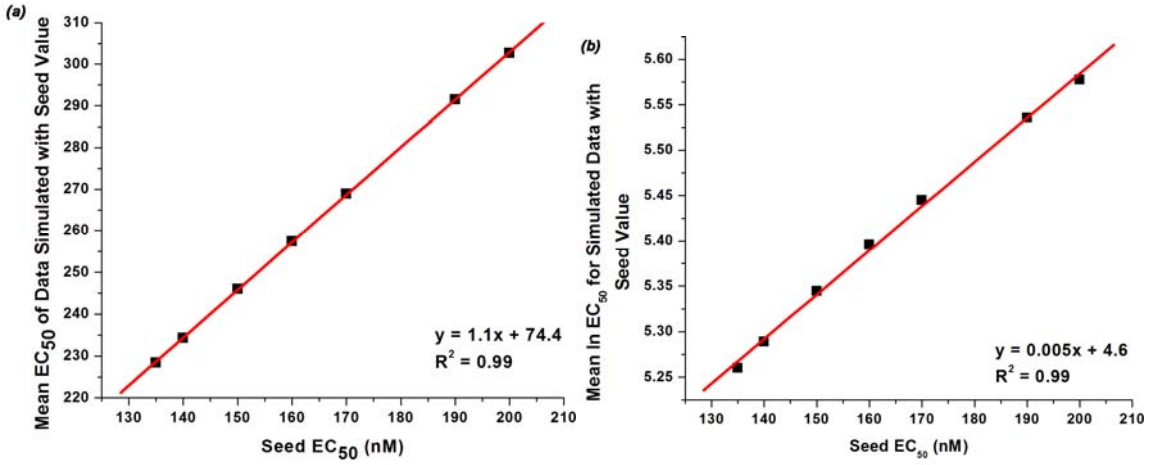


**Figure C.4.** Determination of simulated data $EC_{50}$ seed value. ***(a)*** Mean of generated $cEC_{50}$s plotted versus the seed value for that data set. ***(b)*** Mean of the ln transformed data set plotted versus the seed value. Both plots show the equation of the line that fits the data. These equations were used to determine the appropriate seed value as discussed in the text.

The five sets of 42 simulated dose-response relationships, referred to as Rand1 through Rand5, were then created using the randomly generated α values and the 140 nM $EC_{50}$ seed value (the $n_H$ seed value was set at 1, because only one ligand binds to each GPCR). To create these data sets, we programmed the $W_n$ equation derived above into an Excel spreadsheet and fit the normalized data to the Hill equation ($I_{Norm} = \frac{1}{(1+\left(\frac{EC_{50}}{A}\right)^{n_H})}$, where $A$ is the concentration of drug) with the Origin software package (Origin Lab, Northhampton, MA). Each $cEC_{50}$ data set's mean and variance were compared to those of the 10.10.0 W7.40Trp data set through *t*- and F-tests, resepectively.

### *C.2.4. "Correcting" Actual Data with the Asymmetric Current Change Model*

After generating random $M_2$AChR-like data, we attempted to use this model of asymmetric current changes to "correct" our measured dose-response relationships. By "correct" we mean remove any effect current change had on the dose-response relationship and leave what should be a more accurate $cEC_{50}$ value.

To perform this "correction", we used the measured n = 3.5, n = 6, and n = 8.5 $\alpha$ values for each cell to generate current change progressions as illustrated in Figures C.2 and C.3. With $\alpha$ values for doses n = 1 through n = 10, the actual measured response for each dose was divided by the quantity $1 + \alpha_n$ to produce "corrected" current responses. After normalizing these "corrected" responses, the data were fit to the Hill equation to obtain "corrected" $cEC_{50}$ values. These values were compared to the "uncorrected" data through *t*- and F-tests.

## C.3. Results and Discussion

### *C.3.1. Comparing Simulated Data with Actual Data*

As described in Section 3.2.6.3, Figure 3.23, and Table 3.3, the five simulated data sets had similar means and variances to the 10.10.0 W7.40Trp data set. The *p*-values for the Rand4 *t*-test and the Rand5 F-test were only slightly above 0.05. Visual inspection of the distribution of these two data sets confirms these slight deviations from the actual data (Figure C.5a).

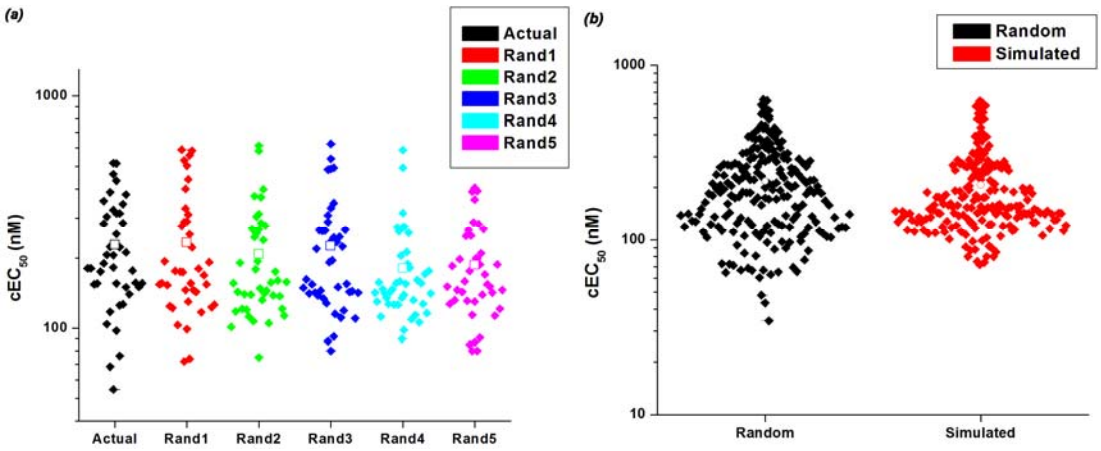


**Figure C.5.** Simulated and randomly generated 10.10.0 W7.40Trp data. ***(a)*** Distribution of actual 10.10.0 W7.40Trp data and simulated data sets Rand1 through Rand5. Open squares denote the $cEC_{50}$ mean. ***(b)*** Distributions of 204 $cEC_{50}$ values randomly generated from a log-normal distribution with the shape parameters $\mu = 5.3$ and $\sigma = 0.537$ and the 204 simulated $cEC_{50}$ values shown in ***(a)***. Comparisons of groups in both ***(a)*** and ***(b)*** described in the text

To further confirm that the simulated data fit a distribution similar to that of the actual data, we randomly generated 204 $cEC_{50}$ values from a log-normal distribution with shape parameters $\mu = 5.3$ and $\sigma = 0.537$ and compared them to the 204 simulated $cEC_{50}$ values (Figure C.5b). The mean and variance of the two sets of numbers were not significantly different (*t*-test $p = 0.4$ and F-test $p = 0.8$).

We therefore conclude that our model for generating $M_2$AChR data is capable of reproducing the means and variability of data that we observe in the laboratory. More specifically, this exercise suggests that asymmetric current changes during the course of a dose-response relationship experiment introduce both variability and a general upward shift in $cEC_{50}$. The fact that the seed value that best replicates the mean $cEC_{50}$ of our actual data was 140 nM, almost 40% lower than the measured mean $cEC_{50}$, suggests the actual ACh $EC_{50}$ for $M_2$AChR may be lower than 230 nM. If a more direct readout of receptor activation were used, we predict that the dose-response relationship would be shifted to lower $cEC_{50}$ values.

### *C.3.2. Data Not "Corrected" Through $\alpha$ Values*

Given the success of the data simulation exercises, we predicted that the "corrected" 10.10.0 W7.40Trp data would have a lower mean $cEC_{50}$ value and a lower standard deviation. Both predictions were incorrect. As shown in Figure C.6, the original and "corrected" data are indistinguishable; the means are 230 nM and 290 nM, while the standard deviations are 140 nM and 260 nM for the original and "corrected" data sets, respectively. In fact, the two variances are significantly different as determined by the F-test ($p = 0.01$).

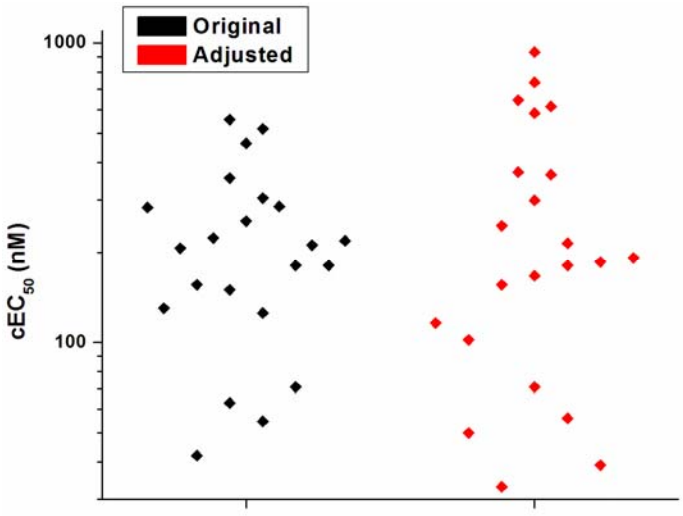


**Figure C.6.** Original and "corrected" 10.10.0 W7.40Trp data. 22 cells of data were "corrected" through the use of current change data collected during the dose-response relationship experiment. Comparisons of the two data sets are discussed in text.

Why did this "correction" fail to lower data variability or change the population mean? One possibility is that the less variable 10.10.0 injection conditions may have mitigated much of the current change-induced variability and that the remaining variability emanates from other sources within the cell. Although if this were true, the

data simulation exercise should not have been as successful at replicating data variability. We believe that the asymmetric current changes are not the sole source of variability in the $M_2$AChR-GIRK 1/4 signaling system. If another data set with higher $cEC_{50}$ variability were "corrected", it is possible that more of its variability would come from current changes and would thus show a greater degree of "correction". Despite the failure of the "correction" methodology with this data set, this procedure should not be abandoned; future data sets may show improvement through this methodology and produce less variable data from this complex signaling system.